Surface Analysis of SLA and SLActive Dental Implants

A thesis submitted to

The University of Manchester

for the degree of

Master of Philosophy

in the Faculty of Medical and Human Sciences

2013

Konstantinos Vazouras

School of Dentistry

Contents

Word count: 33386

List of Figures

List of Tables

List of Abbreviations

Abbreviation	Description
a-C	amorphous Carbon
AES	Auger Electron Spectroscopy
AFM	Atomic Force Microscopy
ALP	Alkaline Phosphatase
APC	Anodic Plasma-Chemical
ar	as received
BE	Binding Energy
bFGF	Basic Fibroblast Growth Factor
CCD	Charge Coupled Device
cp Ti	commercially pure Titanium
DPSS	Diode-Pumped Solid State Laser
E_B	Binding Energy
E_k	Kinetic Energy
EDS	Energy-dispersive X-ray Spectroscopy
EDX	Energy-dispersive X-ray Spectroscopy
EDTA	Ethylenediamine tetraacetic acid
ESCA	Electron Spectroscopy for Chemical Analysis
ETP	Ethane-1,1,2-triphosphonic Acid
FTIR	Fourier Transform Infrared Spectroscopy
GD-OES	Glow Discharge Optical Emission Spectroscopy
HA	Hydroxyapatite
HT	Heat Treated
HBSS	Hanks’ Balanced Salt Solution
HR-SEM	High-Resolution Scanning Electron Microscopy
HV-EDX	High-Voltage Energy-dispersive X-ray Spectroscopy
IR	Infra-Red
KE	Kinetic Energy
LLLT	Low-Level Laser Therapy
LRA	Liquid Reaction Apparatus
LV-SEM	Low Vacuum Scanning Electron Microscopy
MDP	Methylenediphosphonic Acid
MTT	Dimethylthiazol-diphenyl Tetrazolium Bromide
ns	non sandblasted
PDA	Photodiode Array
PDGF	Platelet-Derived Growth Factor
PIIID	Plasma Immersion Ion Implantation and Deposition
PMN	Polymorphonuclear leukocyte
PMT	Photomultiplier Tube
PTP	Propane-1,1,3,3-tetraphosphonic Acid
RBM	Resorbable Blast Medium
SBF	Simulated Body Fluid
SC	Single Crystal
SEM	Scanning Electron Microscopy
SHS	Super High Speed
SLA	Sand blasted Long grit Acid- etched
SLActive	Sand blasted Long grit Acid- etched active

TGF-β	Transforming Growth Factor beta
Ti P	bare polished Titanium discs
ToF-SIMS	Time-of-Flight Secondary Ion Mass Spectrometry
TZP	Tetragonal Zirconia Polycrystals
UHV	Ultra High Vacuum
UV	Ultraviolet
XPS	X-ray Photoelectron Spectroscopy
XRD	X-Ray Diffraction

The University of Manchester

Konstantinos Vazouras

Master of Philosophy

Surface Analysis of SLA and SLActive dental implants

2013

Abstract

Dental implants are routinely used in restorative dentistry to support restorations made to replace missing hard and soft tissues. The more their applications increase, the greater the clinical interest becomes in the implants integrating quickly with the bone in order to be functional. Here we study SLA [7] and SLActive dental implants (Straumann, Switzerland / **SLA**- **S**andblasted with **L**ong grit corundum followed by **A**cid etching with Sulfuric and Hydrochloric acid), which are both made of cold worked titanium grade 2. Combined with SLA and SLActive surfaces they demonstrate good biocompatibility, excellent mechanical strength as well as osseointegration properties. Their only difference lies at the last stage of the production process, when the SLA implants are dry-stored after sand-blasting and acid etching, ready to be used by the surgeon, whereas SLActive implants, after acid etching are rinsed under protective N_2 gas conditions and stored in isotonic NaCl (saline) solution [8]. Buser *et al.* (2004) [9] showed that SLActive surface promotes earlier bone apposition and provides greater implant stability during the first critical weeks of osseointegration.

Here we conduct a surface analysis of SLA and SLActive implants and we study the interactions of these implants with synthetic biological fluids to monitor the changes in the surface of Ti before and after exposure to them. We also discuss the effect of UV treatment on the implant surface as a means of improving the osseointegration time by further reducing carbon contamination of the surface. SLA and SLActive disks (5mm x 1mm) were obtained from Straumann Schweiz (Basel, Switzerland). SLActive had contact angle $<5^o$ compared to SLA contact angle approximately 111^o. Raman analysis results showed that SLA displayed a generally amorphous structure, whilst SLActive displayed both a similar structure to SLA (amorphous) and a more crystalline structure (probably mixture of rutile/anatase). The crystalline peaks observed for SLActive are the same as those of a nano-rutile material. XPS analysis showed reduced atmospheric contamination (Hydrocarbons) of the SLActive surface, while Hanks solution seems to have very little effect on the amount of oxide at the surface. XPS also showed that UV treatment seems to increase the amount of oxygen and carbon at the surface of the SLActive after incubation in Hanks solution for 72 hours.

Declaration

No portion of the work referred to in this thesis has been submitted in support of an application for another degree or qualification of this or any other university or institute of learning.

Signed

Konstantinos Vazouras ______________________

Copyright Statement

The following four notes on copyright and the ownership of intellectual property rights apply to this work:

i. The author of this thesis (including any appendices and/or schedules to this thesis) owns any copyright in it (the “Copyright”) and s/he has given The University of Manchester the right to use such Copyright for any administrative, promotional, educational and/or teaching purposes.

ii. Copies of this thesis, either in full or in extracts, may be made only in accordance with the regulations of the John Rylands University Library of Manchester. Details of these regulations may be obtained from the Librarian. This page must form part of any such copies made.

iii. The ownership of any patents, designs, trademarks and any and all other intellectual property rights except for the Copyright (the “Intellectual Property Rights”) and any reproductions of copyright works, for example graphs and tables (“Reproductions”), which may be described in this thesis, may not be owned by the author and may be owned by third parties. Such Intellectual Property Rights and Reproductions cannot and must not be made available for use without the prior written permission of the owner(s) of the relevant Intellectual Property Rights and/or Reproductions.

iv. Further information on the conditions under which disclosure, publication and exploitation of this thesis, the Copyright and any Intellectual Property Rights and/or Reproductions described in it may take place is available from the Head of School of Dentistry (or the Vice-President) and the Dean of the Faculty of Life Sciences, for Faculty of Life Sciences’ candidates.

Acknowledgements

Firstly, I would like to express my gratitude to my thesis supervisors Dr. Nick Silikas and Dr. Andrew Thomas for their outstanding guidance, inspiration, patience and willingness to motivate me in this research project.

Special thanks to Dr. Emily Smith for her support with the XPS experiment at the University of Nottingham. In addition, I also would like to thank Matthew Murphy for his help and support with the Raman spectroscopy, Contact Angle Goniometry and 3D Optical profilometry experiments at the University of Manchester.

Last but not least, I would like to thank my parents and sister, whose love, patience and moral support has been of unique importance during this graduate project.

1. INTRODUCTION

1.1 Significance of Problem – Purpose of the study

Dental implants were initially used just as an alternative to removable prostheses or as a means to provide additional stability to removable restorations. Nowadays, the clinical indications of dental implants have increased substantially, whereas patients demand a lot more than improvement of mastication. They have high aesthetic expectations, they prefer as shorter treatment time as possible and they rightfully want reliable solutions to their dental problems with as few complications and failure rates as low as possible.

On the other hand, the popularity of implants and their increased demand, has made dentists look for implant systems with more straightforward surgical procedures, shorter osseointegration time, clinical flexibility and, lastly, a variety of prosthetic components to meet varying needs. As a result, sufficient funds are invested in research by companies and academic institutions in the search for the next, more improved, more reliable and successful successor that will replace the current state of the art devices, by trying to improve on, if not eliminate, its limitations and widen its clinical usage indications.

All this has led to significant achievements the last few decades that are meant to primarily benefit the patient. Most importantly, the initial two-stage implant protocol proposed by Brånemark has been altered [10], with quite a few cases being currently treated with immediate loading protocols. There are several factors contributing to the success of the osseointegration of implants [11-16]; the physico-chemical properties of implant surface are nowadays admittedly regarded as the most significant of them all. Over the years, different surface treatments have been suggested and clinically implemented with varying results [17]. Several of these treatments aim at altering the surface chemical composition (Hydroxyapatite or HA deposition, incorporation of Ca ions, phosphates etc.), morphology, micro- and nano-roughness and topography (acid etching, sand blasting). The ultimate purpose of all these treatments was to improve clinical performance of dental implants. Unfortunately, though, all this otherwise healthy competition has led to undoubtedly too many implants on the market worldwide, the majority of which have not been extensively studied, despite their often widespread use.

Although new improved implant systems emerge every so often, and sometimes even after some years of successful clinical use by dentists, it is surprisingly not always clear what is the reason exactly for the improved performance of the novel system. Bearing all these in mind, we decided to study two Straumann implant systems, the SLA and the relatively more recent SLActive, which has been proven to offer shorter osseointegration time, maintaining always similarly impressive success rates in the long term to its predecessor [9, 18].

1.2 Aims and Objectives of the study

The aim of the study was to examine the surfaces of SLA and SLActive dental implants in order to see if there are any differences between them. More specifically, we wanted to find out if the clinical advantage of SLActive implants can be attributed to any changes in the surfaces, in terms of roughness, hydrophilicity, crystallinity and chemical composition. In addition to the aforementioned surface analysis, we wanted to study the interactions of these implants with synthetic biological fluids, as well as to determine the effect of UV treatment in the implant surface.

The specific objectives of the study were to:

- Obtain roughness profiles information with 3D Surface Optical Profilometry.
- Obtain wettability information with Contact Angle Measurements.
- Identify differences in the surfaces of SLA and SLActive as received samples, as well as monitor the changes in the surface of Ti before and after exposure to biological fluids and UV treatment with X-ray photoelectron spectroscopy (XPS).
- Determine the phase of the surface oxide in real dental implant materials with Raman spectroscopy.

1.3 Experimental Hypotheses

Null Hypothesis (Ho) (1): There is no difference in the surface roughness between SLA and SLActive implants.

Alternative Hypothesis (Ha) (1): There is difference in the surface roughness between SLA and SLActive implants.

Null Hypothesis (Ho) (2): There is no difference in the wettability between SLA and SLActive implants.

Alternative Hypothesis (Ha) (2): There is difference in the wettability between SLA and SLActive implants.

Null Hypothesis (Ho) (3): There is no difference in the surface chemical composition between SLA and SLActive implants.

Alternative Hypothesis (Ha) (3): There is difference in the surface chemical composition between SLA and SLActive implants.

Null Hypothesis (Ho) (4): There is no difference in the phase of the surface oxide between SLA and SLActive implants.

Alternative Hypothesis (Ha) (4): There is difference in the phase of the surface oxide between SLA and SLActive implants.

Null Hypothesis (Ho) (5): There is no difference in the interactions with synthetic biological fluids between SLA and SLActive implants.

Alternative Hypothesis (Ha) (5): There is difference in the interactions with synthetic biological fluids between SLA and SLActive implants.

Null Hypothesis (Ho) (6): There is no difference in the effect of UV treatment in the implant surface between SLA and SLActive implants.

Alternative Hypothesis (Ha) (6): There is difference in the effect of UV treatment in the implant surface between SLA and SLActive implants.

2. REVIEW OF THE LITERATURE

2.1 Dental Implants

One of the major goals of modern dentistry is to restore patient dentition to normal function and health, as well as maintaining aesthetics. Preventive dentistry and social awareness of the importance of oral health have contributed significantly in the improvement of the overall oral health of the population globally in the last decades, but still, although tooth decay indices have dramatically dropped, a major part of a dentist's job still includes dealing with partial or full edentulism problems. The increase in people's life expectancy, the increasing prevalence of periodontal disease in the ageing population, conventional fixed prostheses failure, poor performance of conventional removable prostheses as well as psychological consequences of tooth loss have all played a part in the need to find a more predictable, long-lasting and aesthetically pleasing alternative to replacing missing teeth.

Conventional fixed bridges are anything but conservative, increasing the need for further treatment in the future, while they can only be used in cases with limited amount of missing teeth. On the other hand, conventional removable prostheses are not easily persevered by patients, who are usually complaining of not being able to function properly with them and, while in the past they were used a lot, nowadays they are used mainly when there are anatomical or financial restrictions that prevent the clinician from providing the patient with a fixed prostheses. Dental implants, on the other hand, provide a very good alternative for treating missing teeth, serving as both abutments for fixed crowns or bridges as well as abutments to secure, if not "lock", removable prostheses to their position, making the latter ones smaller in size and a lot easier to function with. This explains why implants have become nowadays a standard treatment option for the majority of edentulous patients.

An endosteal implant is an alloplastic material surgically inserted into a residual bony ridge, primarily as a prosthodontics foundation [19]. The prefix *endo* comes from Greek and means "within", and *osteal* means "bone". The term endosseous implant is also used in the literature, and the term *osseous* also indicates bone.

The most common dental implants used in clinical practice nowadays are root form implants which are later connected to a prosthodontics abutment, which will support the prosthodontic restoration on top of it [20] (Fig. 2.1, Fig. 2.2).

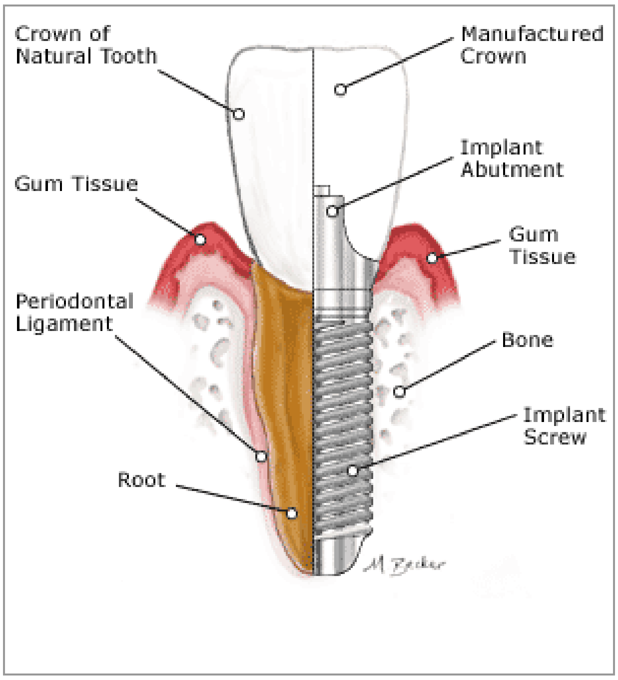

Figure 2.1 Parts of an implant [2]

Figure 2.2 Dental implant as seen in a patient’s mouth and an x-ray [21]

In addition to implants for prosthodontics purposes, implants have been introduced in the orthodontic practice and have provided a valuable solution to anchorage control problems [22]. Their clinical behaviour as rigid fixation points has significantly contributed in the effective management of asymmetry, mutilated dentition, craniofacial deformity and severe malocclusion [23-25]. Nowadays, mini-implants have become part of the everyday practice of clinical orthodontics [26, 27] (Fig 2.3).

Figure 2.3 Mini implant as Temporary Anchorage Device (TAD) for orthodontic reasons [28]

Dental implants vary in length, diameter, thread design and surface properties and specific clinical parameters are usually used to justify the use of the different types. The increasing demand for their use and the so far satisfactory research findings have led to a market of hundreds of different types of implants available, unfortunately most of them not well-documented.

The global dental implantology market is expected to grow by 6 % within the next few years, reaching an estimate of $ 4.2 billion in 2015 [29]. With 18 % of market share within the dental device market in 2009, implantology is the most dynamic market in the dental industry. Europe is the world’s largest market for implants with a 42 % share in 2009, followed by North America with 31 %. There are a lot of companies in the field, out of which the Swiss Nobel Biocare and Straumann together account for more than 50 % of the global market [29].

2.2 Osseointegration

The term *osseointegration* was first introduced by Brånemark, who in 1952 inserted titanium implant chambers in rabbits' bone, while experimenting on microscopic circulation of bone marrow healing, which he could not remove at the end of the experiment. Osseointegration was then defined by him [30] as a direct contact of living bone with an implant material without intermediate fibrous tissue layer, at a microscopic level. Nowadays, the term is commonly used in implant dentistry and it addresses, not only the microscopic bone-implant interface, but also the clinical condition of rigid fixation. Rigid fixation refers to the clinically unobservable movement of the implant when a force of 1 to 500g is applied [20]. In other words, the implant appears to be stable and ankylosed in the bone. Notably, if osseointegration is not achieved, the dental implant therapy is unsuccessful. Osseointegration can be compared with direct fracture healing, in which the fragment ends become united by bone, without intermediate fibrous tissue or fibrocartilage formation. There is though a basic difference: osseointegration unites bone not to bone, but to an implant surface: a foreign alloplastic material. For that reason, the material is very important for the achievement of the aforementioned union.

Human bone is a marvel of natural design, continuously rejuvenating through a finely balanced equilibrium of bone resorption and new bone formation. During the stage of surgical placement of a dental implant, the drill that is used to create space for the implant to be inserted intrudes and destroys the naturally sculptured bone; bone vessels are torn and a major defect is created quickly filling with blood. The implant is inserted where the tooth was previously lost. At first, the only force holding the implant in place is mechanical friction. This is called 'primary implant stability'. Osseointegration or 'secondary implant stability' requires a highly complex sequence of additional biodynamic processes. According to Nguyen *et al.* (2009) [31] the wound healing around the implant is a coordinated and sequentially organized repair mechanism of the organism, which is facilitated by finely tuned communication between the main actors of wound healing, the cells. This unique interaction is accomplished with the help of signalling molecules like cytokines, extracellular matrix proteins and small molecules. Terheyden *et al.* (2011) [5] divided it into *four stages* – the Haemostasis, the Inflammatory phase, the Proliferative stage and the Remodelling stage – in which different cell types participate in a relatively chronological order, but with a certain overlap.

a. The Haemostasis stage: It begins with the surgical trauma of drilling through the bone and placement of the implant, and lasts from minutes to hours. Matrix proteins, growth and differentiation factors become soluble and active, while the injured vessels bleed, laying the foundations to create a first extracellular matrix to the defect. Implant surface interacts immediately with water molecules and ions, changing the surface energy pattern. Blood proteins begin to be rapidly adsorbed and through that process, cells are able to attach to the titanium surface. Metal implant surface bound fibrin can bind thrombocytes, whereas at the vascular injury sites, thrombocytes aggregate and create a white thrombus closing the vascular leak. A series of molecular interactions follows, which results in activation and degranulation of the platelets. The release of cytokines from degranulating thrombocytes marks the initiation of the next stage, the Inflammatory stage.

b. The Inflammatory stage: It starts about 10 minutes after and lasts for the first day after surgery. The granulation of platelets causes release of growth factors (Transforming Growth Factor beta or TGF-β, Platelet-Derived Growth Factor or PDGF, Basic Fibroblast Growth Factor or bFGF) as well as bradykinin and histamine, which cause the initial vasoconstriction (haemostasis stage) to turn to vasodilatation, clinically observable as swelling and warming of the skin lying on top of the surgical wound. Innate host defence systems are activated [32] (glycoproteins, polymorphonuclear leucocytes or PMN, macrophages). Notably, the more bacteria in the wound area, the more intense and prolonged the immune response will be, which can cause degradation of the extracellular matrix and can be toxic for the healthy tissues surrounding the wound. To avoid that, a clean surgical environment and antibacterial measures, such as antibiotics or local disinfection, are absolutely crucial. After having removed tissue debris, macrophages secrete angiogenic and fibrogenic growth factors. The high fibronectin concentration allows attachment of fibroblasts. This initiates the next phase.

c. The Proliferative stage: It lasts from a few days to a few weeks and the transition to it is characterised by the formation of new extracellular matrix and by angiogenesis. This newly formed tissue is called granulation tissue. Angiogenesis is necessary for osteogenesis. First the blood vessel develops and then the bone follows (angiogenetic osteogenesis). An osteoprogenitor cell attaches to the implant surface via integrins. Following firm attachment, the cell that becomes secretory active is called an osteoblast. The latter starts to express osteocalcin and alkaline phosphatase. As early as one week after implant placement, new bone formation starts (Fig. 2.4a) [5]. The new bone is woven bone, which has its collagen fibres randomly oriented. New bone formation is initiated with the secretion of a collagen matrix by osteoblasts. This matrix is subsequently mineralised by hydroxyapatite. The mineralisation at this primary bone formation stage is rapid but not well-structured and not in close association with collagen (Fig. 2.4b) [5].

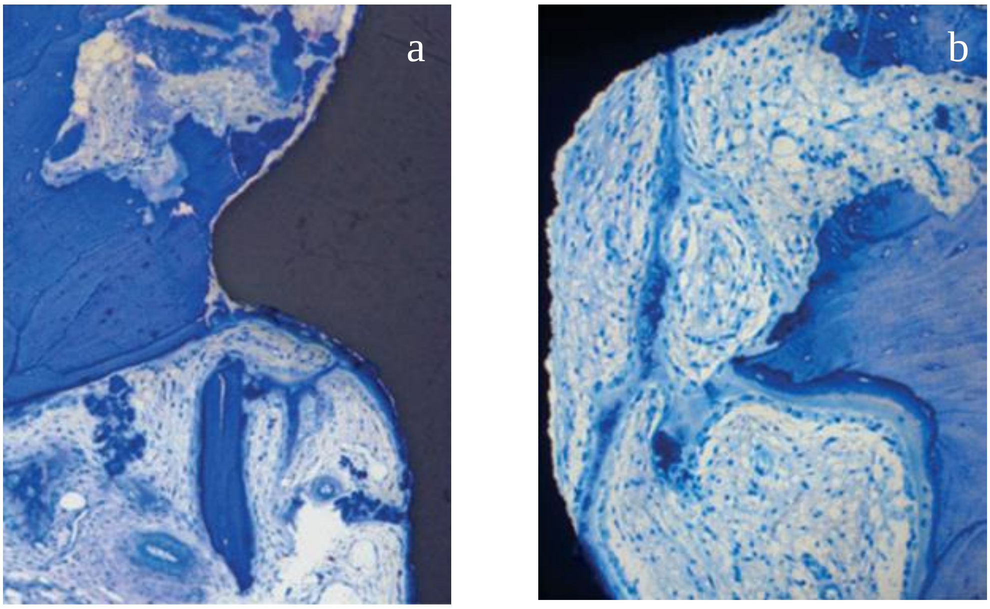

Figure 2.4 a) One-week human histology (toluidine blue) early proliferative phase, sandblasted large grit and acid etched (SLA) surface, initial bone formation bone growing on the SLA surface towards the grooves bone debris without signs of osteoclastic degradation [5]. b)Two weeks human histology (toluidine blue), proliferative phase, sandblasted large grit and acid etched (SLA) surface, new bone starts to bridge between parent bone and implant, bone debris particles incorporated into immature new bone trabeculae, no osteoclastic degradation of bone debris [5].

d. <u>The Remodelling stage</u>: The fourth and last stage, which starts weeks after surgery and lasts for a long time, starts with the removal of the woven bone by osteoclasts (Fig. 2.5a) [5]. Orderly and co-ordinated bone remodelling restores the stability of the site. Load adaptation is of pivotal importance in this context. Initially woven bone will have grown in the valleys of the implant surface and parallel to it. After remodelling, most of the bone will be structured perpendicularly to the peaks of the implant threads and at a right angle to the implant surface. The architecture and organisation of this bone becomes trabecular. The structure is thought to be directly responsive to forces imposed through the implant to the interfacial tissues. This is made possible by the synergy of osteoblasts and osteoclasts (Fig. 2.5b) [5]. The osteoclasts, activated by the osteoblast messenger RANKL, resorb the woven bone, whereas the osteoclasts then lay down a highly organised lamellar bone. The work of both cells is mainly co-ordinated by the osteocyte and its own messenger, such as the Wnt antagonist sclerostin. As a result, the new bone is rigid enough to withstand pressure and traction forces, while maintaining its elasticity.

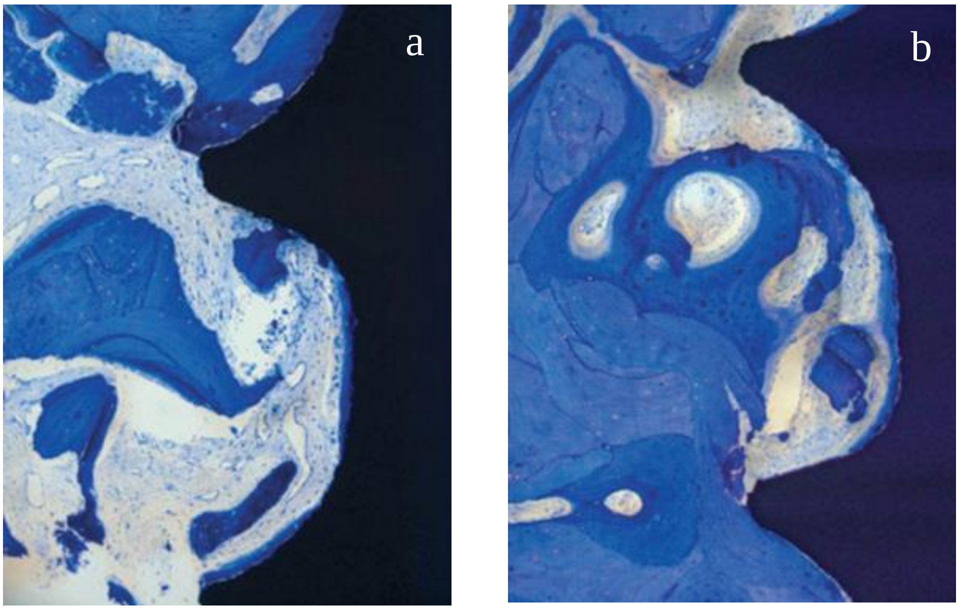

Figure 2.5 a) Four weeks human histology (toluidine blue), transition to remodelling phase, sandblasted large grit and acid etched (SLA) surface, parent bone has been degraded [5]. b) Six weeks human histology (toluidine blue), remodelling phase, sandblasted large grit and acid etched (SLA) surface, remodelling with formation of new primary and secondary osteons [5].

2.3 Factors affecting Osseointegration

The establishment of osseointegration is dependent on several parameters:

- **Implant material and surface characteristics:** Osseointegration requires a bioinert or bioactive material, as well as surface characteristics that induce bone deposition (osteophilic). Bioinert materials don't cause any adverse tissue reactions. Titanium, commercially pure or in certain alloys, is regarded as being bioinert and, thus, is being widely used in both dental as well as orthopaedic surgery [33]. On the other hand, bioactive materials cause favourable tissue reactions either by establishing chemical bonds with tissue components (hydroxyapatite) or by promoting cellular activities involved in bone matrix formation. Such materials usually have poor mechanical properties, which is why in the case of dental implants they are used as coatings (hydroxyapatite). Apart from titanium, which has satisfactory biological and mechanical properties, several implant materials have been used, mostly without success. Nowadays, the only alternative to the widely used titanium implants are Zirconia implants, which may have certain advantages compared to titanium ones, but they are missing on long-term human trials to establish their clinical success [34].

The implant surface is one of the six factors described by Albrektsson *et al.* (1981) [11] to be important for osseointegration. Implant surfaces were initially machined, but the use of implants in compromised sites and the need to load them relatively soon has resulted in implant surface topographical and chemical modifications in order to achieve better bone anchorage and to establish osseointegration sooner. Rough surfaces have been proven to provide better incorporation of the material into the bone tissue compared to smooth ones (Albrektsson & Wennerberg, 2004) [35], while other studies have claimed that implants with a roughened surface may promote the rate and degree of osseointegration (Buser *et al.* 1991 [14]; Cochran *et al.* 1996 [15], 1998 [16]). Thus, most commercially available implants have minimally or moderately rough surfaces, with an average height deviation of 0.5-2 μm. Acid etching, sand-blasting and etching as well as chemical modifications (Hydroxyapatite coating, plasma spraying, anodic oxidation) are the most common implant surface treatments nowadays and research data investigating their effect on osseointegration suggest they are favourable. The major benefits from them appear to be earlier bone formation, enhanced biomechanical interlocking and higher bone-implant contact consequently increasing the load-transmitting surface [36].

- **Primary Stability:** Is believed to play a significant role in successful osseointegration. Brånemark *et al.* (1977) [37] and Albrektsson *et al.* (1981) [11] considered it to be a prerequisite, while others like Meredith (1998) [38] and Friberg *et al.* (1999a) [39] suggested that primary stability may a useful predictor for osseointegration. The primary stability of implants is subject to their appropriate design and precise press fitting at surgery. It is essential to have increased initial stability, since it reduces the risk of increased micromotion and fibrous tissue formation at the bone implant interface during both healing as well as loading. In this way, high bone-implant contact is achieved and, thus, successful osseointegration.

During the surgical insertion of the implant, the latter is passively stabilised in the jawbone through friction with primary bone contacts. The denser the bone is, the more available primary contacts there are, thus, higher primary stability is achieved. Micromovement caused by load forces greater than friction hold can be catastrophic, since the bone surface is smoothened and the bone-implant interlock is decreased. The first days after the surgery are crucial, whereas the first few weeks are detrimental for a successful osseointegration; the primary stability decreases to critical levels, before new bone starts to form and secondary stability can be established.

- **Loading conditions:** Following the Brånemark protocol, all implants require a prolonged period of time before they can be loaded, in order for the osseointegration to develop first. Early loading was then considered a serious cause for implant failure, since the micromovement caused would cause fibrous tissue to form around the implant. Nowadays, this is not exactly the case and under certain circumstances, immediate or early loading is indeed an existing alternative to the standard one or two stage delayed loading protocols. An increased primary stability, though, is a necessity for immediate loading (Glauser & Meredith, 2001) [40]. Surgical and prosthodontic considerations are taken into account and different loading protocols have been suggested, depending on the area or extent of the edentulism, the state of the surgical site and, of course, patients' expectations.

- **Surgical procedure:** A delicate surgical procedure is necessary to ensure osseointegration (Brånemark *et al.* 1977 [37], Albrektsson *et al.* 1981 [11]). The surgery must be performed following the "minimal tissue violence" principles, whereas constant cooling during drilling and a clean surgical environment contribute to an uneventful and quicker healing of the surgical trauma.

- **Bone density:** Research and clinical data have shown osseointegration success is affected by bone quality. In 1985, Lekholm and Zarb [41] came up up with a list of different bone qualities that were found in the anterior area of the jaws (Fig. 2.6). *Type I* consisted of homogeneous compact bone. *Type II* had a thick layer of compact bone surrounding a core of dense trabecular bone. *Type III* was composed of a thin layer of cortical bone surrounding dense trabecular bone of favourable strength, and last, *Type IV* was characterised by a core of low-density trabecular bone surrounded by a thin layer of cortical bone. A higher failure rate was observed for Type IV bone quality, and an increased overall success rate for Types II and III.

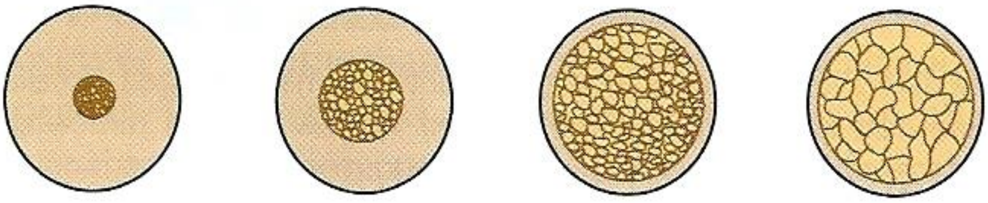

Figure 2.6 Four bone qualities for the anterior region of the jaws [41]

Bone density, in general, varies in different regions of the jawbones making the lower anterior region of the mandible the area with the most favourable bone quality, followed by the lower posterior and upper anterior areas, and leaving the upper posterior area of the maxilla last regarding favourable bone quality for implant placement**.** Turkyilmaz and McGlumphy (2008) [42] showed also that local bone density has a prevailing influence on primary implant stability, which is an important determinant for implant success. Implants inserted in location with higher bone density have more stability.

2.3.1 Trends in dental implants' surface characteristics

The continuously increasing implant demand and their growing application in cases where early loading is required or in compromised sites has contributed to continuous attempts being made in order to increase bone anchorage and earlier osseointegration establishment. These attempts are focusing on improving the bone-implant interface either physically by altering the surface topography and/or chemically or biochemically by incorporating inorganic or organic phases on or into the TiO_2 layer [43].

By changing the surface topography, at a micrometre level a rougher surface is created, which increases the initial bone anchorage and strengthens the biomechanical interlocking between the implant and the bone, at least up to a certain level of roughness [44]. In addition, on a nanometre scale, a roughness rise leads to increase of surface energy and hence to enhancement of matrix protein adsorption, bone cell migration and proliferation and finally osseointegration.

On the other hand, chemical modification of implant surfaces, such as incorporation of calcium phosphate on the TiO_2 layer, might encourage bone regeneration and increase biomechanical interlocking between surface materials and bone matrix proteins [44]. Moreover, biochemical modification, such as incorporation of proteins, peptides or enzymes, can promote specific cell and tissue responses. Although most techniques promote either physical or chemical modification, there are processes that can combine both. For example, electrochemical anodization of the titanium surface, which causes not only thickening of the TiO_2 layer, but also ion impregnation on the same layer, as well as porous structures [45].

The main techniques used for surface modification [46] can be divided in three groups:

a. Addition of material: Titanium plasma projection (TPS, TiO_2); coating with Hydroxyapatite or calcium phosphate.

b. Removal of material: grit-blasting and/or acid etching (usually performed using hydrofluoric, nitric or sulphuric acid and combinations). Acid-etching often follows grit-blasting in order to homogenise the implant's microprofile, as well as to remove as much residual blasting particles as possible. Laser treatment -as applied in implants- is also a material removing (subtraction) method.

c. Surface modification without either removing or adding material. This includes electron beam thermal treatment and ion implantation.

The importance of the surface properties of dental implants in achieving osseointegration is evident from the growing number of studies published annually. The wider the clinical use of dental implants gets, the more intense the interest in their surface characteristics becomes. The surface analysis of implants is made possible through several analysis techniques, among which are X-ray Photoelectron Spectroscopy (XPS), Raman Spectroscopy and Atomic Force Microscopy (AFM), Optical 3D Profilometry and Contact Angle Goniometry.

2.3.2 Titanium Dioxide layer (TiO_2)

Titanium (Ti) and its alloys have excellent mechanical, anticorrosive, and biocompatibility characteristics, and they are thus used predominantly as dental implants. A thin, dense, protective oxide layer (mainly TiO_2) forms spontaneously on the Ti surface when exposed to the atmosphere. This passivation oxide layer is very adherent and electrochemically inert, thus giving titanium and its alloys excellent anti-corrosive and biocompatibility properties [47]. When a Ti implant is introduced into the human body, the surrounding tissue is in direct contact with the Ti-oxide layer on the Ti surface. For this reason, the biocompatibility of the Ti implant depends on the properties of this surface oxide layer such as its microstructure, chemical composition, and morphology [48].

Titanium dioxide has three polymorphs, rutile, anatase and brookite, with rutile being the most common [49]. At low temperatures and pressures, anatase is the most stable form of TiO_2, whereas at high temperatures and pressures, anatase will undergo a phase change to rutile. They both have similar density and hardness and both have tetragonal symmetry [50]. However, anatase and rutile have different crystal structures as demonstrated in Figure 2.7, in which the red atoms are oxygen and the grey atoms are titanium. In the bulk unit cell of rutile the lattice constants are $a=b=4.587$ Å, $c=2.953$ Å. In the anatase unit cell they are $a=b=3.782$ Å, $c=9.502$ Å [51]. In both structures, a titanium atom is bonded to six oxygen atoms in a distorted octahedral fashion. In rutile, neighbouring octahedra share one corner and are stacked in an alternating pattern such that adjacent octahedra have their long axes at 90° to each other. In anatase, the octahedra share corners to form (001) planes and are connected with their edges [51]. Figure 2.8 displays the stacking of the octahedra in the rutile and anatase structures. Threefold coordinated oxygen atoms are found in both rutile and anatase structures. Brookite, on the other hand, is rare compared to the other two TiO_2 polymorphs and it exhibits photocatalytic activity [52]. It is built up of distorted octahedra with a titanium ion in the centre and oxygen ions at each of the six vertices. Each octahedron shares three edges with adjoining octahedra, forming an orthorhombic structure [53]. In the brookite unit cell the lattice constants are a=5.456 Å, b=9.182 Å and c=5.143 Å [54]. Brookite will revert to rutile structure at temperatures above 750 °C [55]. Finally, the atomic arrangement in amorphous TiO_2 may be described as an assembly of short staggered chains of octahedral TiO_6 units. Similar spatial arrangement of octahedral units is found in brookite with the differences that the interatomic correlations in amorphous TiO_2 extend to much larger distance than that for brookite and there is a significant number of structural defects in the amorphous TiO_2 [56]. Notably, the most appropriate structure of TiO_2 for biomineralization is anatase [57].

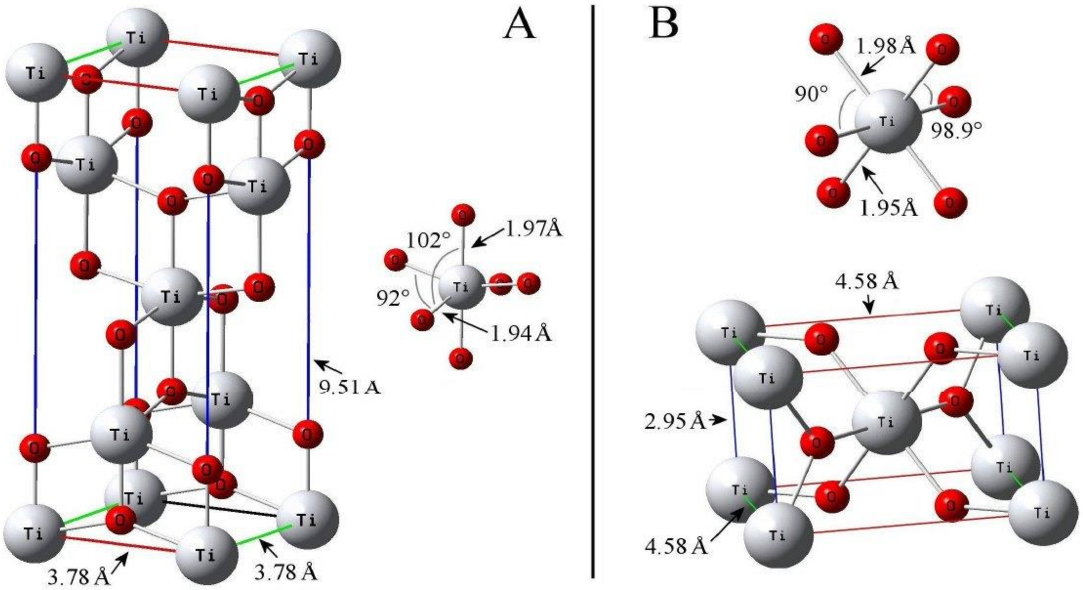

Figure 2.7 Structures of A: anatase and B: rutile, polymorphs of TiO_2 [58]

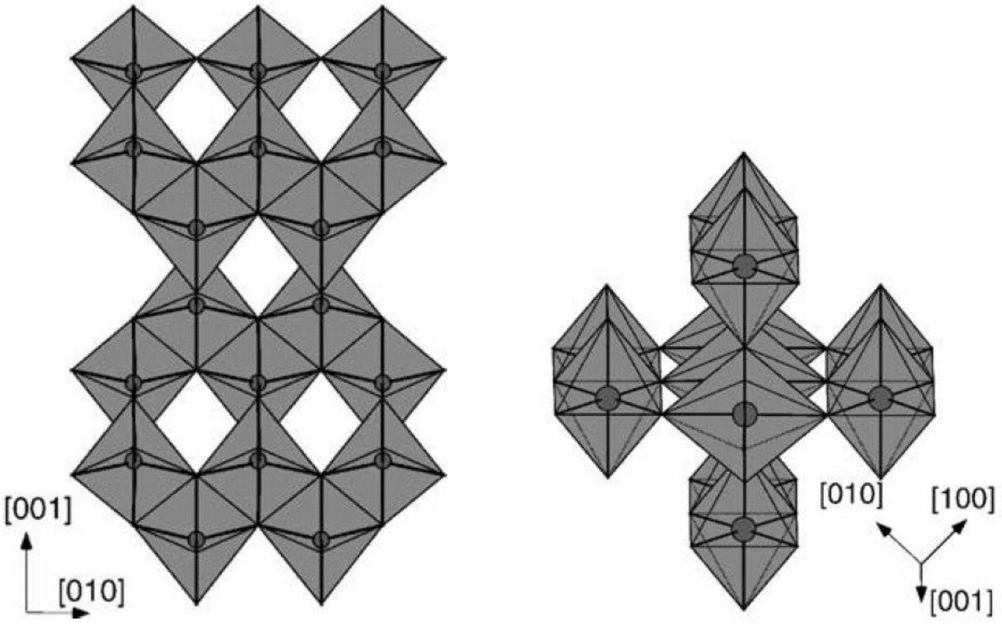

Anatase

Rutile

Figure 2.8 Stacking of TiO_2 octahedra in anatase and rutile structures [51].

2.4 SLA and SLActive dental implants

The implants that were chosen in this study were SLA and SLActive dental implants (Straumann, Switzerland). Both implant types are made of cold worked titanium grade 4 and combined with SLA and SLActive surfaces they demonstrate good biocompatibility, excellent mechanical strength as well as osseointegration properties.

The SLA surface was first introduced in 1998 and it is one of the most documented rough surfaces in dental implantology. It is produced using a large-grit (250-500 μm) sandblasting technique with corundum particles that generates a macro-roughness on the titanium surface. This is then followed by a strong acid-etching bath with a mixture of HCl/H_2SO_4 at elevated temperature for several minutes. This creates 2-4μm micropits superimposed on the rough-sanded surface so that the etching process itself superposes a micro-roughness. The resulting topography offers an ideal structure for cell attachment. Noteworthy, the abbreviation SLA was introduced by Buser *et al.* in a histomorphometric study in 1991 [7] and stands for Sand-blasted, Large grit, Acid etched.

SLA and SLActive dental implants are manufactured in the same way; their only difference lies at the last stage of the production process. The SLA implants are dry-stored after sand-blasting and acid etching, ready to be used by the surgeon, whereas SLActive implants, after acid etching are rinsed under protective N_2 gas conditions and stored in isotonic NaCl (saline) solution (Fig. 2.9). The process results in a more active hydrophilic surface (SLActive surface), with higher surface energy and less hydrocarbon contamination from the atmosphere [59]. This surface remains active until the implant is actually surgically inserted into the bone by the surgeon, where the primary interaction with the aqueous biosystem is therefore accelerated.

Buser *et al.* (2004) [9] showed that the SLActive surface promotes earlier bone apposition and provides greater implant stability during the first critical weeks of osseointegration. After eight weeks, both implant types showed similar results. Bone formation between the two implants was also compared in a study in foxhounds by Bornstein *et al.* (2008) [18]. According to it, SLActive demonstrated statistically significantly higher newly formed bone-to-implant contact length than SLA, whilst a significant increase in bone formation was obvious in both SLA and SLActive implants.

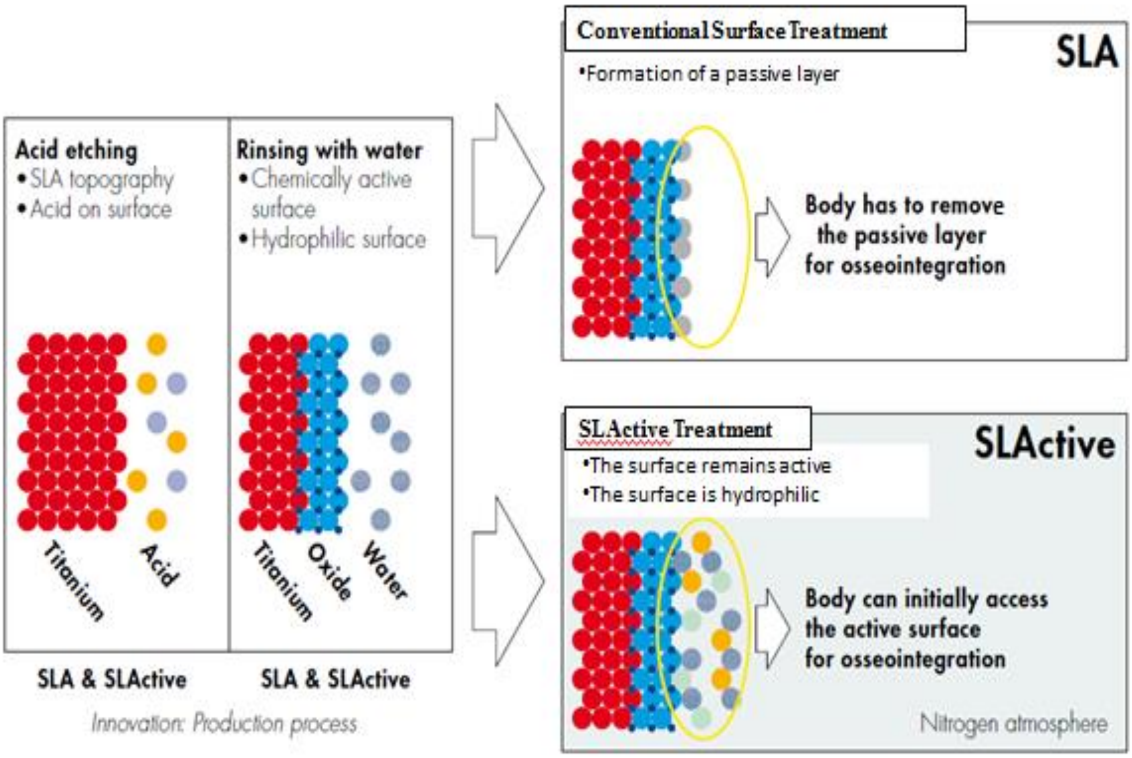

Figure 2.9 Production process of SLA and SLA surfaces. The yellow and green circles represent different species in the sterile solution in which the SLActive surface is stored [8].

2.5 X-Ray Photoelectron Spectroscopy (XPS)

2.5.1 History

X-Ray photoelectron spectroscopy (XPS) [60-63] is one of the most common methods for chemical analysis of surfaces. It has its origins in the investigations of the photoelectric effect (discovered in 1887 by Heinrich Rudolf Hertz and explained by Albert Einstein in 1905) and it was in 1954 when K. Siegbahn and his group in Uppsala, Sweden managed to obtain the first X-ray photo-electron spectrum from cleaved sodium chloride. A few years later in 1967, Siegbahn published a comprehensive study on XPS bringing instant recognition of the utility of XPS. Siegbahn named his new method ESCA (Electron Spectroscopy for Chemical Analysis) and used it mostly for the chemical analysis of gas molecules. With the development of ultra-high vacuum (UHV) technology in the late sixties XPS or ESCA became suitable for the analysis of solid surfaces and commercial instruments became available.

2.5.2 Introduction to XPS

X-Ray Photoelectron Spectroscopy (XPS) is a quantitative spectroscopic technique that determines the elemental composition, empirical formula, chemical state and electronic state of the elements that exist within a material.

XPS is a surface chemical analysis technique that can be used to analyse the surface chemistry of a material in its "as received" state, or after some treatment, for example: fracturing, cutting or scraping in air or UHV to expose the bulk chemistry, sputtering to clean off some of the surface contamination, exposure to heat to study the changes due to heating, exposure to reactive gases or solutions, exposure to ion beam implant, exposure to ultraviolet light.

The XPS facility is composed of the following components: Introduction chamber to transfer a sample from the air, preparation chamber to clean or to treatment a sample and analysis chamber. In the analysis chamber we find the X-ray source with an Al-Kα / Mg-Kα twin anode, an electron collection lens and the hemispherical energy analyser, which measures the kinetic energy of the electrons. The electrons are then counted at the electron detector.

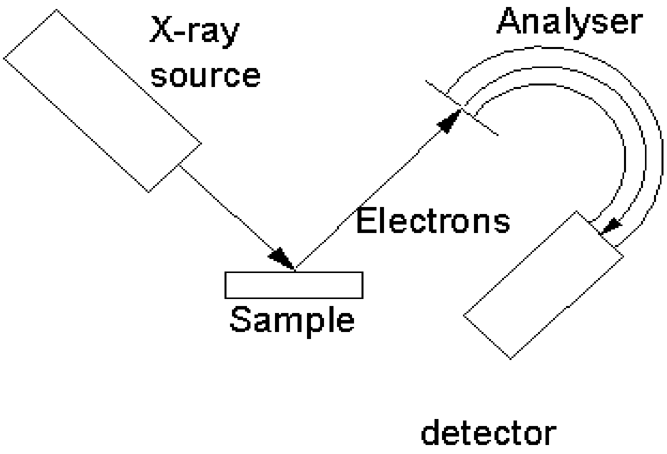

Figure 2.10 Schematic diagram of XPS (adapted from Ref. [61])

2.5.3 Core Level Emission

XPS spectra are obtained by irradiating a material with a beam of soft X-rays while simultaneously measuring the Kinetic Energy and number of photoelectrons that are emitted (Fig 2.11). Usually electrons from the inner shell of an atom (core electrons) are evaluated in an XPS experiment, because the spectra of valence electrons are too complicated to retrieve chemical information.

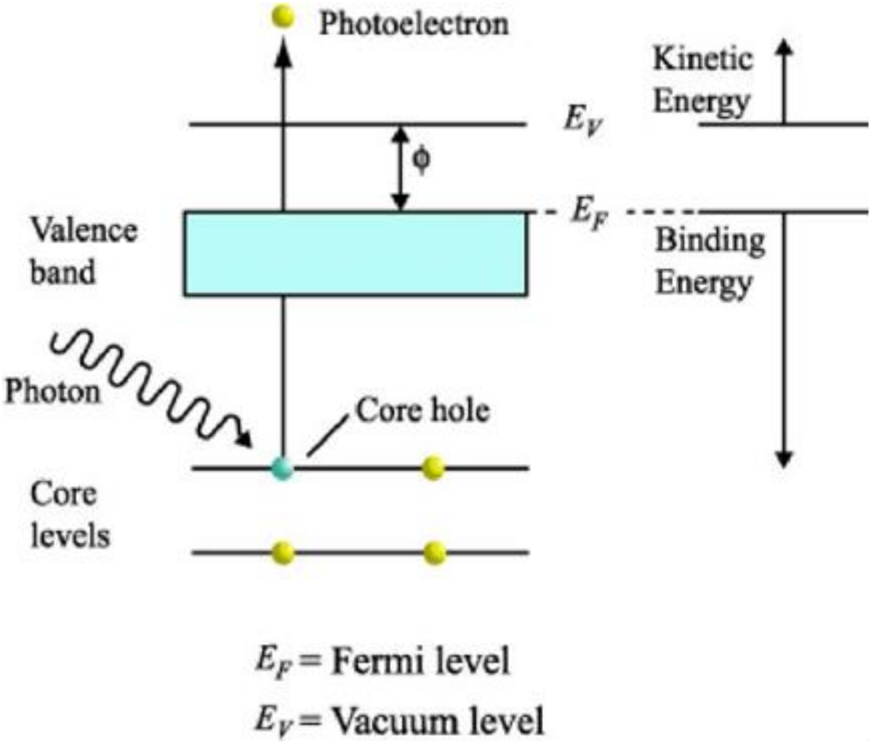

Figure 2.11 Schematic diagram of Core Level Emission [64]

The x-rays cause photo-electron emission according to the Einstein equation:

$$E_K = h\upsilon - E_B - \varphi$$

where E_K is the measured kinetic energy of the emitted photo-electron, $h\upsilon$ the energy of the exciting radiation, E_B the binding energy (BE) of the electron in the solid and φ the work function of the surface i.e. the energy required to get the electron free of the surface.

2.5.4 Elemental Information

The kinetic energy of a particular photoelectron depends on the energy of the photon that excited the atom and therefore will vary if different X-ray sources are used. In order to have a fixed value that is comparable with different sources, the BE of a photoelectron is used as an indication of which element the electron came from and, in this way, the elemental composition of the surface can be ascertained. XPS detects all elements with an atomic number $Z \geq 3$, so it cannot detect Hydrogen ($Z=1$) and Helium ($Z=2$). Tables of BE of each electron in each element are available. The elements in a sample can be identified directly from a survey scan from the characteristics photoemission lines.

2.5.5 Quantification

The probability of a particular photoelectron being excited and emitted from an atom following an interaction with a photon is known as photoionization cross-section of the electron. But each element and orbital has a different cross-section for absorption of X-rays. In addition, the electron energy analyser has a different transmission function for electrons of different kinetic energies i.e. not all electrons of all kinetic energies pass through the analyser with the same probability. Thus the ionisation cross section and transmission function are different for different elements and different orbitals. Each type of analyser also has a different transmission function. Therefore sensitivity factors (the measure of the likelihood that an electron from a particular element will reach the detector) are experimentally derived using standard materials of known composition.

In order to calculate the relative amounts of each element in a compound or mixture we measure the areas under the elemental peaks of the spectrum. We divide the areas by the number of scans and, finally, we divide this area by the sensitivity factor. As a result, an indication of the surface composition is obtained.

2.5.6 Spin-Orbit Coupling

Energy splitting of a photoelectron peak is commonly found in an XPS spectrum, because of the interaction between the spins of the electron, ***s***, (positive or negative) and its orbital angular momentum, *l*. This interaction leads to a splitting of the degenerate state into 2 components with different binding energies. The energy splitting depends on the total electronic angular momentum, *J*.

Different electronic orbitals have different extent of energy splitting. But, the spin orbital splitting for a core level electron of a particular element in different compounds are nearly the same. Also, the intensity ratios of the doublet peaks for a core level electron in different compounds are the same. So, the spin energy splitting and intensity ratio (Fig. 2.12) help us identify different elements.

Every electron has an orbital angular momentum l, which is characteristic of the electron velocity and orbital radius. It can be quantized since the electron can travel only in certain discrete orbitals and can take values 0,1,2,3.. corresponding to s,p,d,f.. orbitals. Each orbiting electron has also spin (positive or negative), which induces an inherent magnetic field. The magnetic field has a spin momentum, characterized by a spin quantum number s, which can take values ± 1/2.

The combination of the orbital angular momentum and the spin momentum create the total electronic angular momentum, which is a vector sum of the two momenta. This vector summation can take place in 2 different ways: *j* - *j* coupling and *L* - *S* coupling.

j-j COUPLING

In this summation, the total angular momentum of a single isolated electron is obtained by summing vectorially the individual electronic spin and orbital angular momenta. It is characterized by the quantum number j, where $j = l + s$ with values 1/2, 3/2, 5/2 etc. Summation is performed for all electrons, resulting in the total atomic angular momentum, with a quantum number J, where $J = \Sigma j$.

Under the *j-j* coupling scheme the nomenclature is based on the principal quantum number n, and on the electronic quantum number *l* and *j* (Table 2.1).

Quantum number			**Spectroscopic notation**
n	***l***	***j***	
1	**0**	**1/2**	**1s**
2	**0**	**1/2**	**2s**
2	**1**	**1/2**	$\mathbf{2p_{1/2}}$
2	**1**	**3/2**	$\mathbf{2p_{3/2}}$
3	**0**	**1/2**	**3s**
3	**1**	**1/2**	$\mathbf{3p_{1/2}}$
3	**1**	**3/2**	$\mathbf{3p_{3/2}}$
3	**2**	**3/2**	$\mathbf{3d_{3/2}}$
3	**2**	**5/2**	$\mathbf{3d_{5/2}}$

Table 2.1 Spectroscopic notation

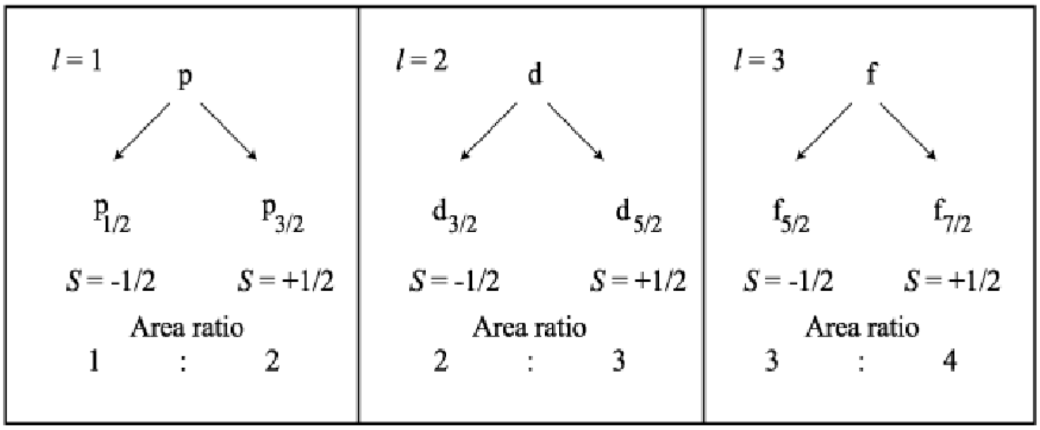

Figure 2.12 Summary of intensity ratios for different electronic orbitals

L-S COUPLING

L - *S* coupling is another way to carry out the summation of the total angular momentum. In this summation, one first sums all individual electronic angular momenta, and then all the individual electronic spin momenta. These two total momenta are then characterized by two quantum numbers: the total atomic *orbital* angular momentum quantum number *L,* which is equal to Σl, and the total *spin* quantum number *S,* which is equal to Σs. Coupling of the two total momenta will give the total atomic angular momenta, characterised by the quantum number J, where J = / L±S / and can take any integral values between /L-S/ and /L+S/

2.5.7 Shake-up Satellites

After photoemission the atom is left positively ionised. This causes a substantial reorganisation of the valence electrons, which relax inwards until a new stable state is reached. This process is called relaxation, and the speed of it will depend on the element in question and its immediate environment. It may also involve excitation of one of them to a higher unfilled level ('shake-up'). The energy required for this transition is not available to the primary photo-electron and thus this two-electron process can lead to a discrete structure on the low kinetic energy (KE) side of the photo-electron peak, which is called a shake-up satellite and has diagnostic value in the interpretation of data.

2.5.8 Chemical Shift

Atomic orbitals from atoms of the same element in different chemical environments possess different binding energies. This is called the Chemical Shift effect and it ranges from 0.1 to 10 eV. Chemical shifts arise as a result of variations in electrostatic screening experienced by core electrons as the valence electrons are drawn towards or away from the specific atom. Differences in oxidation state, molecular environment, co-ordination number will all cause chemical shifts, with the oxidation state playing usually a major role in the effect. An increase in the oxidation state of an atom means that valence electrons are removed, the attraction of the remaining electrons from the nuclei is increased and as a result so is the binding energy.

2.5.9 Surface Sensitivity

Photoelectron spectroscopy is a surface sensitive technique. Its surface sensitivity can be explained in terms of the inelastic mean free path of electrons, λ. The inelastic mean free path, λ, is defined as the distance travelled by an electron between successive inelastic collisions. When the energy of the electron is larger than 100 eV, the higher the kinetic energy of the electron the longer the inelastic mean free path (Fig. 2.13).

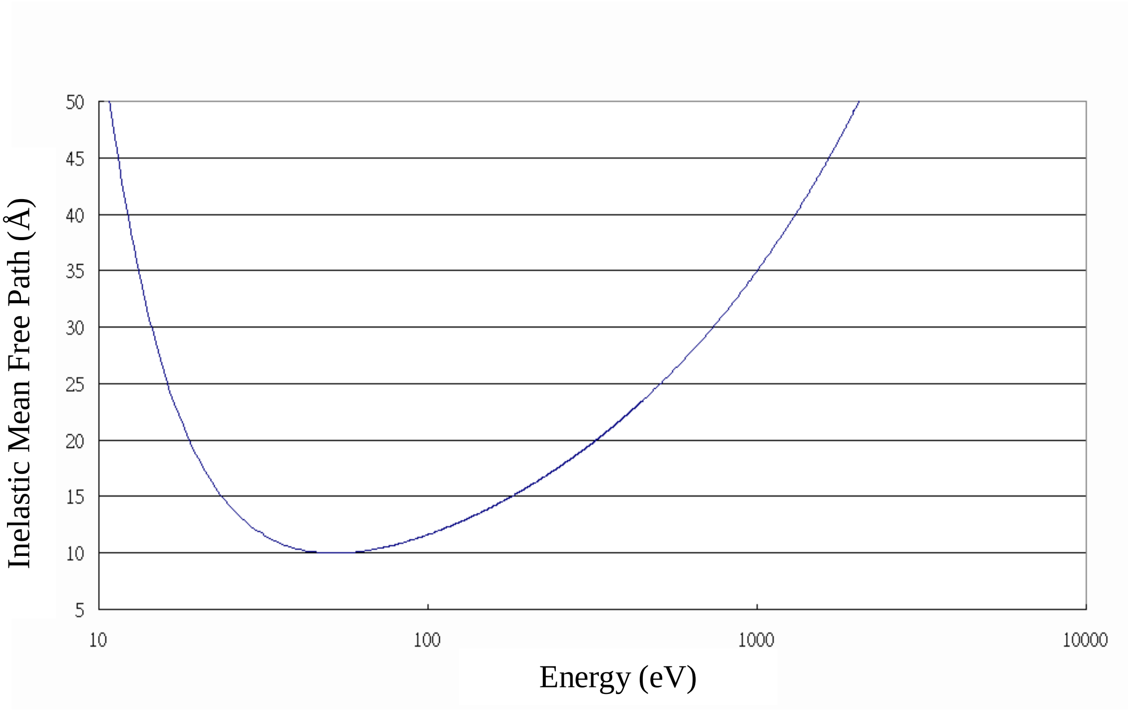

Figure 2.13 The Universal Pathlength Curve - Inelastic mean free path of electron at different energies [63].

When X-ray photons enter below a sample surface, photoelectrons are produced. Some travel out from the surface without losing any energy. Some of them lose energy owing to inelastic collisions (Fig. 2.14).

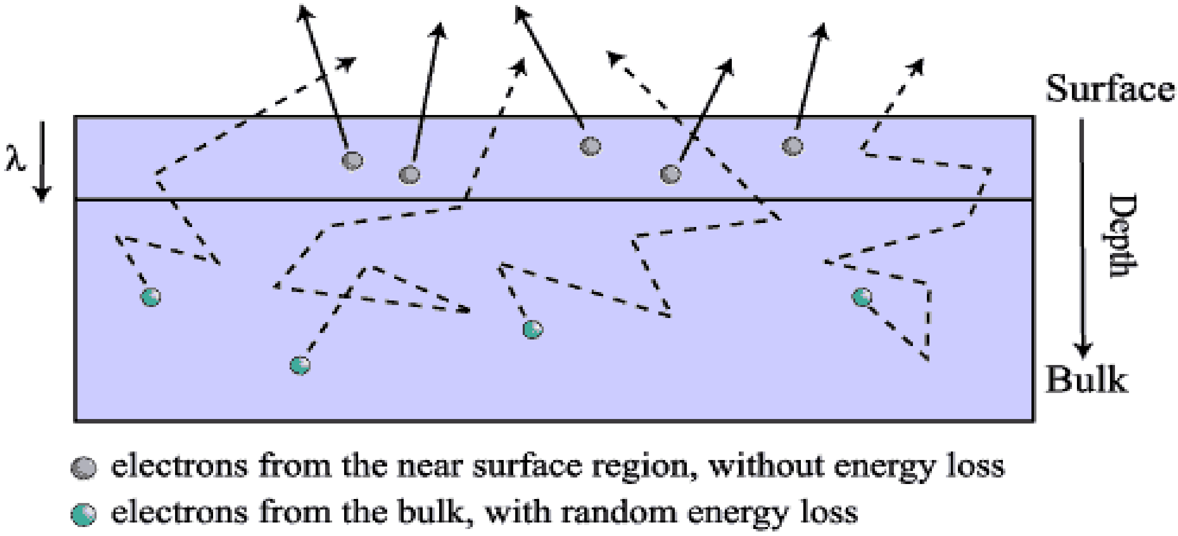

Figure 2.14 Schematic diagram showing the elastic or inelastic collisions of excited photoelectrons depending on the sample depth of origin.

It has been shown that the intensity of ejecting electrons through a medium with no energy loss will follow an exponential decay function. When using XPS, 95% of the photoelectron signals come from the surface region of 3 λ thick. The remaining 5% of signals come from the deeper region. Typically we get signal from 10 Å into a surface although this depends on the energy of the photoelectron. This explains the surface sensitivity of XPS.

Taking that into consideration, if we orient the sample in a way so that electrons are coming out at an angle to the sample surface causes the XPS instrument to become more surface sensitive. λ remains the same, but the electrons emitting from the sample now are coming from closer to the sample surface. The ‘probe’ depth at a particular angle is given by $d\sin\theta$ as shown in Fig. 2.15.

Notably, there are problems associated with ultra-high vacuum techniques in providing reliable data for hydrated surfaces or surfaces existing at atmospheric conditions. For example, information on hydrated surfaces is lost since all water is evaporated before measurements can be made. This can lead to salts being deposited out of solutions, thus giving a false impression of concentration of ions in solutions at the surface. It also means that proteins lose their conformation. That is why surface measurements may be substantially different in ultra-high vacuum compared to the state of the surface in air or in the body when water is present. High pressure XPS is now becoming a reliable technique and is helping to bridge the pressure gap.

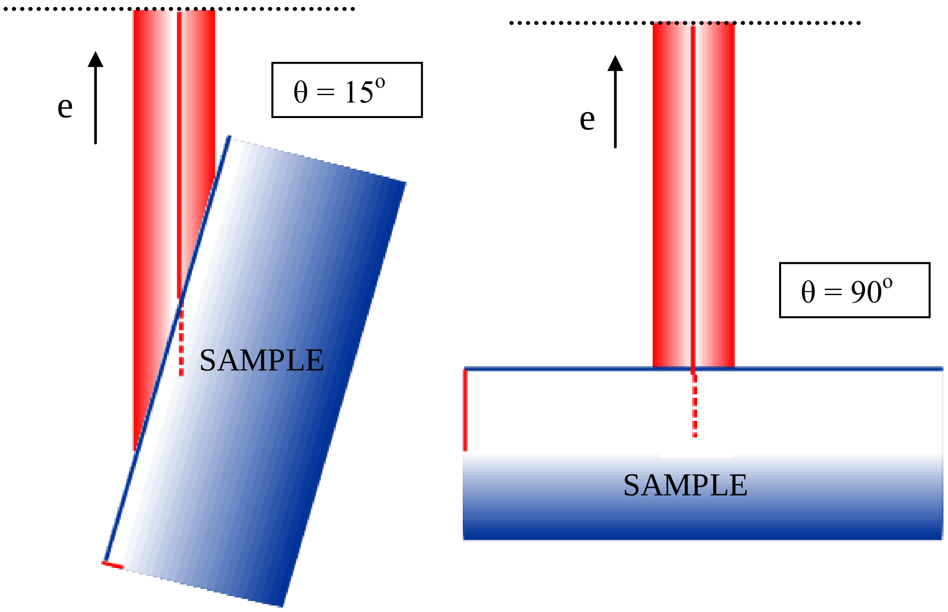

More Surface Sensitive

Less Surface Sensitive

Figure 2.15 Information depth = $d\sin\theta$ [61, 65]

d = Escape depth ~ 3 λ

θ = Emission angle relative to surface

λ = Inelastic Mean Free Path

2.6 Raman Spectroscopy

2.6.1 History

The Raman Effect was named after one of its discoverers, the Indian scientist Sir C.V. Raman who won the Nobel Prize in Physics in 1930 for this. He used sunlight, a narrow band photographic filter to create monochromatic light, and a “crossed filter” to block this monochromatic light and found that a small amount of light had changed frequency and passed through the "crossed" filter. The theory of the Raman Effect was further developed by physicist G. Placzek between 1930 and 1934. The principal light source was at that time the mercury arc, but this has been replaced nowadays by lasers [3].

2.6.2 Introduction to Raman Spectroscopy

Raman spectroscopy [3] is very useful as a technique for the analysis of a wide range of substances –solids, liquids and gases. It is very straightforward, non-destructive and does not require any form of sample preparation. It involves illuminating a sample with monochromatic light and using a spectrometer to examine light scattered by the sample.

By means of Raman spectroscopy one can get a full picture of the sample’s properties, which include: Chemical composition and component identification, molecular structure characterisation, distribution of components at micron and sub-micron scales as well as stress measurements.

One of the major advantages of Raman spectroscopy is that the samples used can be very small, such as very small single crystals, single grains of powder, individual polymer filaments or liquid samples of just 1 nL. In addition, the samples can be oriented, since Raman scattering from water is weak, enabling studies of aqueous samples. Moreover, high pressure or temperature cells can be used in situ in reactors.

However, interference from fluorescence, often from trace impurities, can obscure the Raman spectrum of the major component. Ultraviolet (UV) or near-IR (Infra-Red) excitation can reduce this problem. Laser excitation can lead to photochemistry in the focused laser beam and multiphoton processes may alter the spectrum.

A Raman Spectrometer is composed of four major parts (Fig 2.16) [3]:

An excitation source (Laser), a sample illumination system and light collection optics, a wavelength selector (Filter or Spectrophotometer) and lastly, a detector (Photodiode array-PDA, charge coupled device-CCD or photomultiplier tube-PMT). Fig. 2.16 applies only for dispersive Raman instruments and not for FT-Raman.

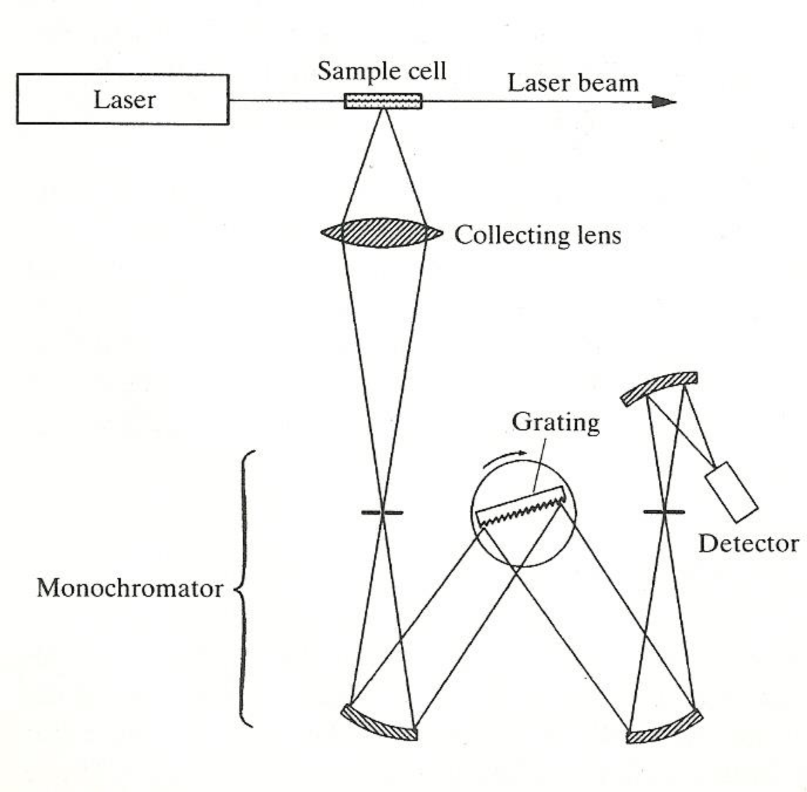

Figure 2.16 Schematic diagram of a Raman Spectrometer [3] .

Typically, a sample is illuminated with a laser beam. Light from the illuminated spot is collected with a lens and sent through a monochromator. Wavelengths close to the laser line due to elastic Rayleigh scattering are filtered out while the rest of the collected light is dispersed onto a detector.

Raman spectroscopy is a useful technique for material identification, since different materials have different vibrational modes, and therefore characteristic Raman spectra. There is one important distinction to make between the Raman spectra of gases and liquids, and those taken from solids - in particular, crystals. For gases and liquids it is meaningful to speak of the vibrational energy levels of the individual molecules that make up the material. Crystals, on the other hand, do not behave as if comprising molecules with specific vibrational energy levels; instead the crystal lattice undergoes vibration. These macroscopic vibrational modes are called *phonons*.

2.6.3 Raman Scattering and Raman Shift

When a beam of light passes through a transparent material, a relatively small amount of light (radiation energy) is scattered. The majority of the scattered light will be of the same frequency to that of the incident beam, if monochromatic radiation or radiation of a very narrow frequency band is used (*Rayleigh scattering*). At the same time, a small amount of the scattered light will be of higher or lower frequencies compared to the incident beam (*Raman scattering*).

A better understanding of the Raman Scattering can be achieved using the quantum theory of radiation, according to which light is a stream of particles, called photons, which have energy $h\upsilon$, where h is Planck’s constant and υ their frequency. Photons undergo collisions with the molecules of the material they go through and these collisions can be either elastic, in which case the photons are deflected unchanged, or inelastic, where energy has been exchanged during the collision. The amount of energy a molecule can gain or lose as a result of the inelastic interaction with the photon abides certain laws of quantum mechanics and is equivalent to the difference in the vibrational and / or rotational energy between the initial and final molecular state. If the final vibrational state of the molecule is more energetic than the initial state, then the emitted photon will be shifted to a lower frequency in order for the total energy of the system to remain balanced. This shift in frequency is referred to as a Stokes Shift, while the radiation scattered with a lower frequency is named Stokes radiation. If the final vibrational state is less energetic than the initial state, then the emitted photon will be shifted to a higher frequency, and this is described as an Anti-Stokes Shift, whereas the radiation scattered with a higher frequency is known as Anti-Stokes radiation.

Raman scattering is an example of inelastic scattering because of the energy transfer between the photons and the molecules during their interaction. The Raman Effect comprises a very small fraction, about 1 in $10^{7,}$ of the incident photons. A simplified energy diagram that illustrates these concepts is given below (Fig. 2.17).

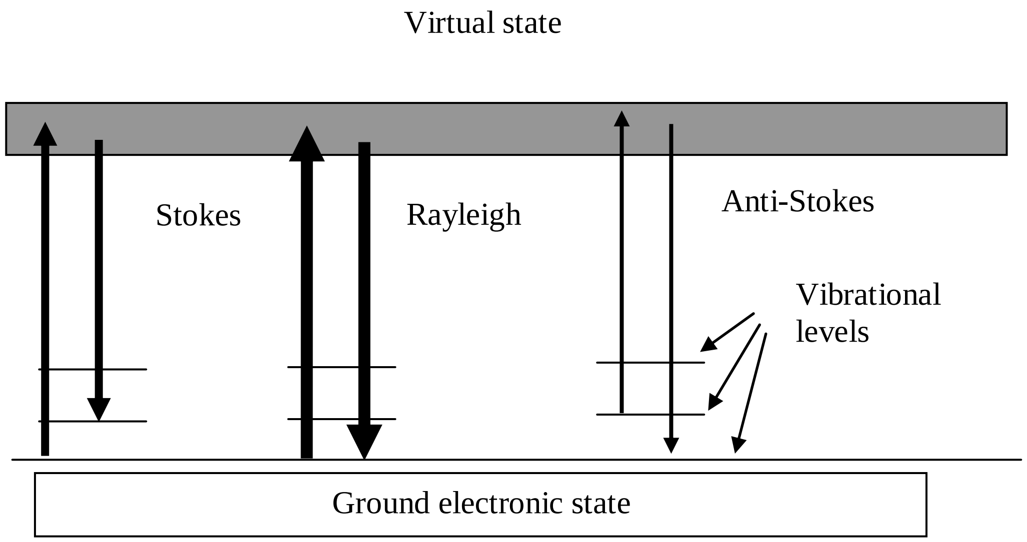

Figure 2.17 Energy level diagram showing the states involved in Raman signal. The line thickness is roughly proportional to the signal strength from the different transitions [1, 4].

On the grounds that Stokes radiation relates to an increase in the molecular energy, while Anti-Stokes radiation involves the molecule losing energy (which can only happen if the molecule is initially in an excited rotational and/or vibrational state), the former is generally more intense than the latter. The same is for the Stokes / anti-Stokes lines at a typical Raman spectrum, as seen on the diagram below. In Raman spectroscopy, usually the more intense Stokes line is measured. The intensity of the Raman signal is generally very weak, which necessitates the use of highly sensitive equipment. Additionally, in order to increase the signal intensities, lasers are used as the exciting radiation source, since they provide intense monochromatic radiation (Fig. 2.18).

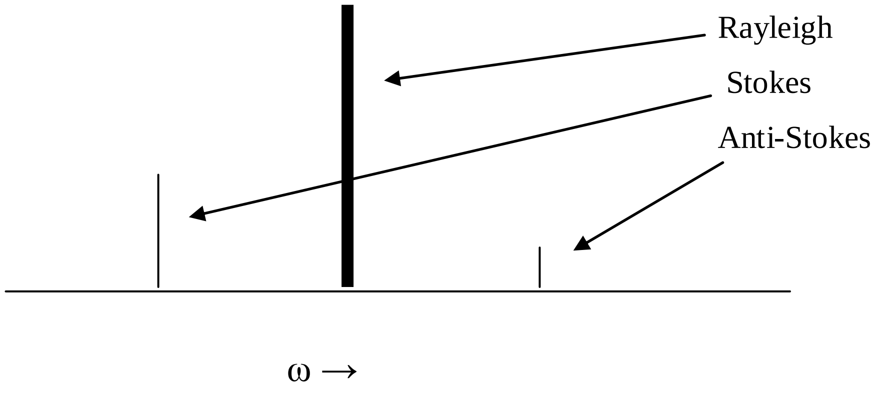

Figure 2.18 Schematic diagram of a rotational Raman spectrum [1]

2.6.4 Raman Activity Rule - Molecular Polarizability

When a molecule in positioned into a static electric field it gets distorted, since the positive pole of the field attracts its electrons and the negative pole its positively charged nuclei. As a result, an induced electric dipole moment is being set up in the molecule and the molecule is polarised. The size of the dipole μ depends on how easily the molecule can be distorted (polarizability, α) as well as on the magnitude of the applied field, E.:

$$\mu = \alpha E$$

The polarizability of a molecule is not the same in all directions. It is possible to represent it though by drawing a *polarizability ellipsoid*. This is defined by a three-dimensional surface whose distance from the electrical centre of the molecule is proportional to $1 / \sqrt{a_i}$, where a_i stands for the polarizability along the line joining point i on the ellipsoid with the electrical centre. Consequently, where the molecular polarizability is least, the axis of the ellipsoid is greatest, and vice versa as displayed on the following diagram of a water molecule (Fig. 2.19).

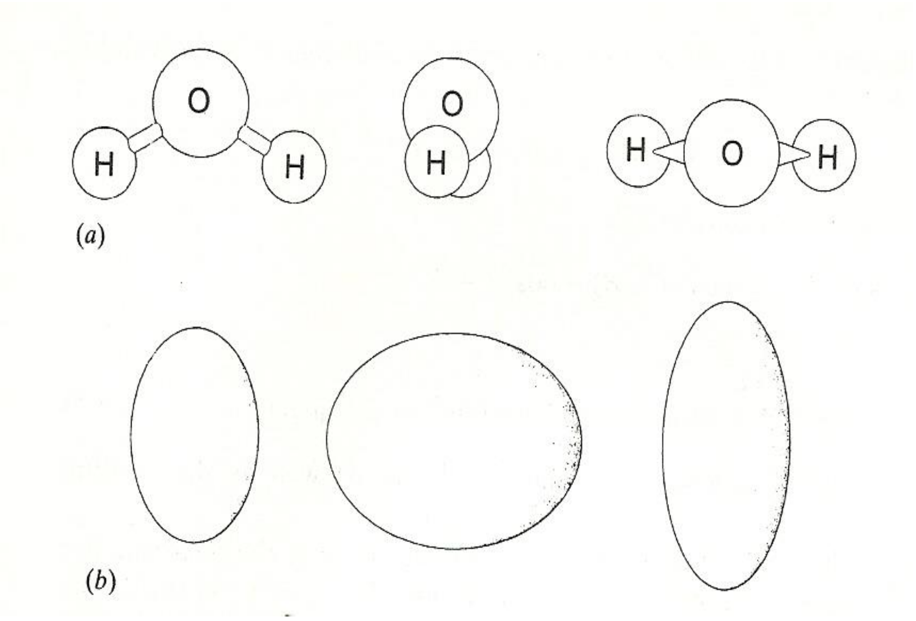

Figure 2.19 The water molecule (a) and its polarizability ellipsoid (b), seen along the three main axes [3].

As a general rule:

In order for a molecular rotation or vibration to be Raman active it must cause some change in a component of the molecular polarizability. A change in polarizability is shown by a change in either the direction or the magnitude of the polarizability ellipsoid.

In addition, symmetrical vibrations give rise to intense Raman lines, while asymmetric ones are usually weak and occasionally unobservable.

Raman spectroscopy provides critical information about lattice vibrations that make Raman apart from complementary to IR a versatile tool complementary to XRD. Vibrational information is specific to the chemical bonds and symmetry of molecules. For that reason, it provides a fingerprint by which the molecule can be identified. In solid-state physics, spontaneous Raman spectroscopy is used to, among other things, find the crystallographic orientation of a sample. Just as with single molecules, a solid material has also characteristic phonon modes that can help an experimenter identify it [66, 67].

Finally, there are limitations of Raman spectroscopy on biological issues. Although higher power and/or longer signal integration may improve Raman signal, such settings are detrimental to biological samples due to sample thermal degradation [68]. Therefore, the laser wavelength, power level and integration time for biological samples must be carefully selected.

2.7 Optical 3D Profilometry

Optical profilometry [69] is a fast, non-destructive and non-contact surface metrology technique, which enables fast data acquisition over relatively large areas. It uses the wave properties of light to compare the optical path difference between a test surface and a reference surface.

An optical profiler (Fig. 2.20) is a type of microscope in which light from a lamp is split into two paths by a beam splitter. In one path the light is directed onto the test material surface, while in the other path the light is directed onto a reference mirror. Reflections from the two surfaces are then recombined and projected onto an array detector. Given that the distance from the beam splitter to the reference mirror is the same distance as the beam splitter is from the test surface, constructive and destructive interference occurs in the combined beam wherever the length of the light beams vary. This creates the light and dark bands known as interference fringes, which appear when the path difference between the recombined beams is on the order of a few wavelengths of light or less. Taking into consideration that the reference mirror is as flat as possible- any optical path differences result from height variances on the test surface. The interference beam is focused into a digital camera, in which constructive interference areas appear lighter, whereas destructive interference areas appear darker. This interference contains important information about the surface contours of the test surface.

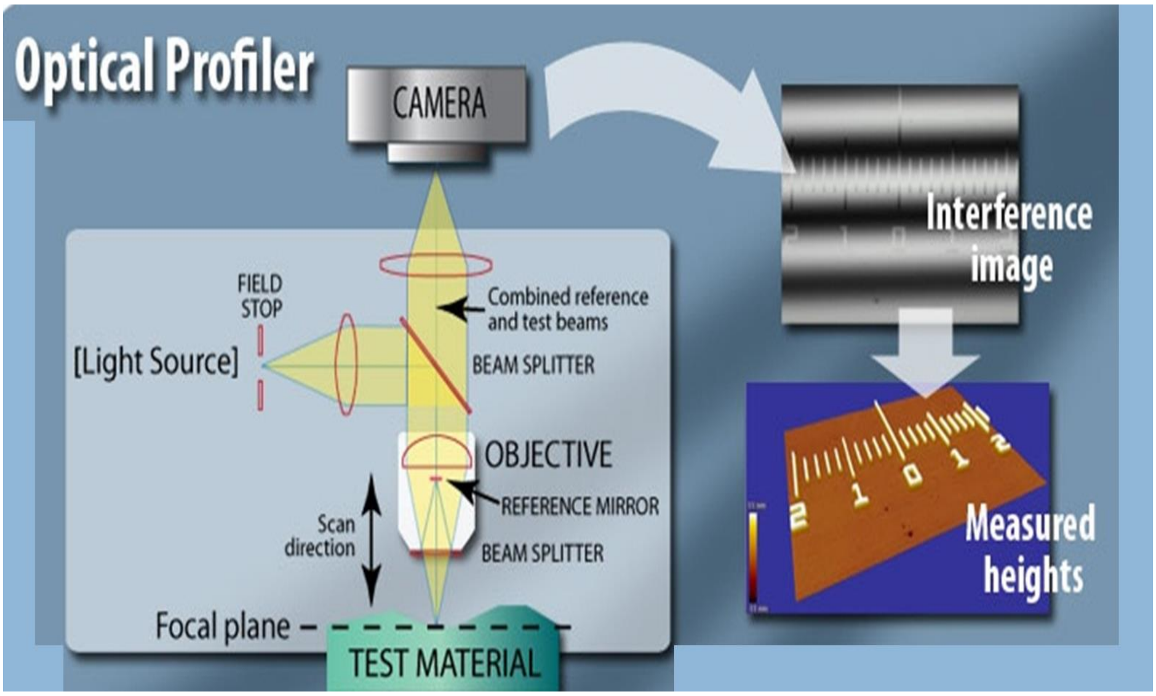

Figure 2.20 Schematic diagram of an Optical Profilometer [70].

The surface measurement achieved through the optical profilometry determines surface topography, thus confirming a surface's suitability for its function. The concept of surface measurement entails surface shape, surface finish, surface profile roughness (Ra) or in a surface area roughness (Sa), surface texture, asperity and structural characterization. Surface roughness is a quantitative calculation of the relative roughness of a linear profile or area, expressed as a single numeric parameter.

In three dimensional optical profilometry, roughness refers to surface area roughness (Sa), which is additionally able to report average profile roughness (Ra) through a surface by calculating the average of several profiles. Some of the most common applications include surface topography and coating thickness measurements, as well as 3D imaging. Amplitude, spatial, hybrid and functional parameters are required to fully characterise surface roughness [71].

While Ra remains useful as a general guideline of surface texture, it typically proves too general to describe the surface's functional nature. A surface with sharp spikes, deep pits, or general isotropy may all yield the same average roughness value. Ra makes no distinction between peaks and valleys, nor does it provide information about spatial structure. That is why 3D parameters can be employed to provide greater insight into surface finish and performance [72].

In order to quantify surface measurement, R parameters were initially developed for two-dimensional, stylus type profilers. Most of these were later adapted for three-dimensional use too, for applications such as optical profilers which provide true 3D measurements. The optical profilometer that was used for our measurements provides S parameters, which give surface, spatial as well as hybrid information for 3D surfaces, by providing 3D equivalents to the standard 2D R-Parameters (S_a for R_a, S_q for R_q etc.) in addition to extra information relevant to 3D surfaces only. The most commonly used S parameters are displayed in Table 2.2 [73].

Term	**Definition**	**Use**
S_a	The *Roughness average* is the arithmetic mean of the absolute values of the surface departures from the mean plane.	S_a is normally used to describe the roughness of machined surfaces. It is useful for detecting variations in overall surface height and for monitoring an existing manufacturing process. A change in Sa usually signifies a change in the process.
S_q	The root mean square (RMS) roughness, obtained by squaring each height value in the dataset, then taking the square root of the mean.	For finish of optical surfaces. Represents the standard deviation of the profile and is used in computations of skew and kurtosis. Sq cannot detect spacing differences or the presence of infrequent high peaks or deep valleys.
S_z	The *Ten Point Average* of the absolute heights of the five highest peaks and five deepest valleys.	For evaluating surface texture on limited access surfaces, particularly where the presence of high peaks or deep valleys is of functional significance. The S_z calculation reduces the effects of odd scratches or irregularities.
S_p, S_v	*Maximum profile peak height* and *Maximum profile valley depth* are the distances from the mean line/surface to the highest/lowest point in the evaluation length/area.	Peak height provides information about friction and wear on a part.
S_{ku}	*Kurtosis* is a measure of the “spikiness” of the surface, or the distribution of spikes above and below the mean line. For spiky surfaces, $S_{ku} > 3$;	Kurtosis is useful for evaluating machined surfaces and is sometimes specified for the control of stress fracture. S_{ku} is high when a high proportion of the surface falls within a narrow range of

Table 2.2 S-Parameters for surface measurements

	for bumpy surfaces, $S_{ku} < 3$; perfectly random surfaces have kurtosis of 3. Kurtosis is also a measure of the randomness of surface heights.	heights. If most of the surface is concentrated close to the mean surface level, S_{ku} will be different than if the height distribution contains more bumps and scratches. The farther the value is from 3, the less random (i.e., the more repetitive) is the surface.
S_{sk}	*Skewness* measures the asymmetry of the profile about the mean plane. Negative skew indicates a predominance of valleys, while positive skew is seen on surfaces with peaks.	S_{sk} can illustrate load carrying capacity, porosity, and characteristics of nonconventional machining processes. Surfaces that are smooth but are covered with particulates have positive skewness, while a surface with deep scratches/ pits will exhibit negative skewness. If S_{sk} exceeds ±1.5, you should not use average roughness alone to characterize the surface. Skewness is very sensitive to outliers in the surface data.

Table 2.2 S-Parameters for surface measurements

2.8 Titanium as a dental biomaterial

The most commonly used materials in dental implantology are titanium and titanium alloys. Titanium is a metal with low weight, high strength/weight ratio, low modulus of elasticity, exceptional biocompatibility, outstanding corrosion resistance and easy shaping and finishing [20]. These properties explain why it is the most widely used material in the manufacturing of dental implants, in the commercially pure form (cp Ti) or as an alloy. The most common alloy is Ti_6Al_4V and comprises 90% by weight titanium, 6% aluminium (decreases specific weight and improves elastic modulus) and 4% vanadium (decreases thermal conductivity and increases hardness). Titanium and its alloys are resistant to corrosion at biological pH and potential because of the formation of an insoluble titanium oxide layer on the surface. In air, the oxide, usually TiO_2, begins to form within nanoseconds (10^{-9} s) and reaches a thickness of 20–100 A° in 1 s. It is very adherent to the parent Ti and impenetrable to oxygen [74]**.** Titanium oxidizes (passivates) on contact with room temperature air and normal tissue fluids. When an implant is placed within a very tight fitting site in bone, areas scratched or abraded would repassivate in vivo [75]. All these qualities justify the uniqueness of this metal and are really valuable to their use for dental implants.

The topography and surface chemistry of the implant surface is extremely important for the establishment of the osseointegration. The study of this surface and the attempt to improve the bone-implant interface as a result, in order to achieve better osseointegration and at a faster rate after the initial surgical insertion of the implant is of major research interest in the last years in dental implantology. To achieve that, several surface analysis techniques have been utilised. XPS, Raman spectroscopy, 3D Profilometry, Contact Angle Goniometry and AFM, as the most representative are mentioned below.

Viornery *et al.* (2002) [76] used phosphoric acid as a titanium surface modifier to improve bone bonding and did surface analysis with XPS. Three phosphoric acids (methylenediphosphonic acid or MDP, propane-1,1,3,3-tetraphosphonic acid or PTP, and ethane-1,1,2-triphosphonic acid or ETP) were synthesized and grafted on bare polished Ti discs (Ti P) and XPS analysis as well as time-of-flight secondary ion mass spectrometry (ToF-SIMS) suggested a chemical link between titanium surface and phosphoric acid molecule. To assess the bioactivity of the modified discs, they were incubated inside

Hank's solution for 1, 7, 14 days and XPS analysis showed only slightly higher calcium levels compared to the reference Ti P surface, with ETP showing the best performance of the three modifiers.

De Maeztu *et al.* (2003) [77] did a histomorphometric analysis on 88 implants placed in rabbit tibial bone. The implants were made of c.p. Ti and Ti_6Al_4V and were surface treated with different ion implants (C^+, CO^+, N^+, Ne^+). The results of the surface analysis (Scanning Electron Microscopy or SEM, Energy-dispersive X-ray Spectroscopy or EDS, XPS) indicated statistically significant improvement of bone integration (% bone-implant contact) for C^+ and CO^+ implant groups. In these groups XPS suggested a Ti-O-C bone-implant interface entailing covalent type bonds where the C atom belongs to a complex organic molecule. These bonds are stronger and more stable than the ones usually found between bone and titanium oxide and correspond to the protein-metal oxide bond formed during ion treated implant positioning in the living animal.

Morra *et al.* (2003) [78] suggested that different implant surface topographies correspond to different surface composition and, thus, different surface chemistry. They divided 34 commercially used implants in four surface-topography-based categories (machined, sand-blasted, acid-etched and plasma sprayed) and using XPS they showed that acid-etched and plasma-sprayed surfaces had higher titanium and lower carbon concentration than machined surfaces and suggested surface chemistry may be a variable controlling biologic response too.

Morra *et al* (2005) [79] used a collagen-coated titanium implant to study the microhardness and surface chemistry at the implant-bone interface in a short-term rabbit model. Surface analysis was done with XPS, while an indentation test measured the bone hardness. Results of the XPS, showing decomposition of the C1s peak proved that surface-immobilised collagen preserved all the molecular features of the control nonimmobilised reference. In addition, microhardness measurements confirmed that newly formed bone at the bone/collagen-coated-implant interface was harder than at the interface of the control (commercially pure titanium) implant and bone, suggesting that collagen coating enhances bone maturation and mineralisation.

Vanzillotta *et al* (2006) [80] examined the effect of different surface treatments of c.p. Ti implants on *in vitro* bioactivity. C.P. Ti sheets were submitted to three different surface treatments, followed by etching with an HCl / H_2SO_4 solution. Part of each sample was then either anodic or thermal oxidated and immensed in a Simulated Body Fluid (SBF) solution. Analysis of samples was performed using XPS, SEM and profilometry and it was suggested that the *in vitro* bioactivity of titanium after different surface treatments can be enhanced in a SBF solution at 37°C.

Berardi *et al.* (2008) [81] used XPS analysis, as well as SEM / Energy-dispersive X-ray Spectroscopy (EDX) analysis to assess the surface microstructure and the purity of new laser-treated implant surfaces. A diode-pumped solid state laser (DPSS) with Nd: YAG source operating in Q-Switching mode was used on titanium samples and the results showed surfaces with a total absence of contamination as well as very regular roughness. Lopes *et al.* (2003) [82] studied the effect of laser radiation of implants to improve bone healing. Fourteen rabbits were inserted a titanium implant to their tibia. Eight of the implants were first irradiated with lambda 830nm laser (Thera Lase, DMC, Sao Carlos, SP, Brazil, 21.5 J/cm^2, 10mW, spot size 0.60mm), while the other six acted as the control group. The animals were sacrificed 15, 30 and 45 days after the implantation and Raman spectroscopy was performed on the implants. Significant differences on inorganic as well as organic components were found between the irradiated implants and the controls, as well as between the irradiated ones, the longer they stayed implanted. It was suggested that low level laser therapy does indeed improve bone healing. In addition, Lopes *et al.* (2005) [83] used near-infrared Raman spectroscopy to evaluate the incorporation of hydroxyapatite of calcium (CHA; similar to 960 cm^{-1}) on the healing bone around dental implants submitted or not to low-level laser therapy (LLLT) (lambda 830 nm) and concluded that LLLT does improve bone healing.

Liu *et al.* (2008) [84] tested how the fluoride-ion implantation would affect titanium biocompatibility. By means of plasma immersion ion implantation technique, fluoride ions were inserted into smooth pure titanium surface. XPS as well as SEM analysis was used to analyse the surfaces, whereas in vitro co-culture assays were performed to evaluate the biocompatibility of MG-63 cells to the modified titanium. Study results showed that titanium biocompatibility could be increased by fluoride-ion implantation.

In a study by Stajer *et al.* (2008) [74] XPS and AFM were used to study the effects of different F^- containing caries-preventive prophylactic rinses and gels on the roughness and surface structure of c.p. Ti. Aqueous 1% NaF solution (3800 ppm F^-, pH 4.5) or high (12,500 ppm) F^- content gel (pH 4.8) strongly corroded and modified the surface composition. XPS indicated formation of a strongly bound F^--containing complex (Na_2TiF_6). AFM showed an increase in roughness (Ra) of the surfaces (Fig. 2.21): 10-fold for the NaF solution and smaller for the gel or a mouthwash (250 ppm F^-, pH 4.4). Human epithelial cell attachment and proliferation were investigated by dimethylthiazol-diphenyl tetrazolium bromide (MTT) and protein content assays. The study concluded that the adverse effects of a high F$^-$ concentration and low pH should be taken into consideration when prophylactic gels are utilized by patients with implants, or other dental appliances made of titanium.

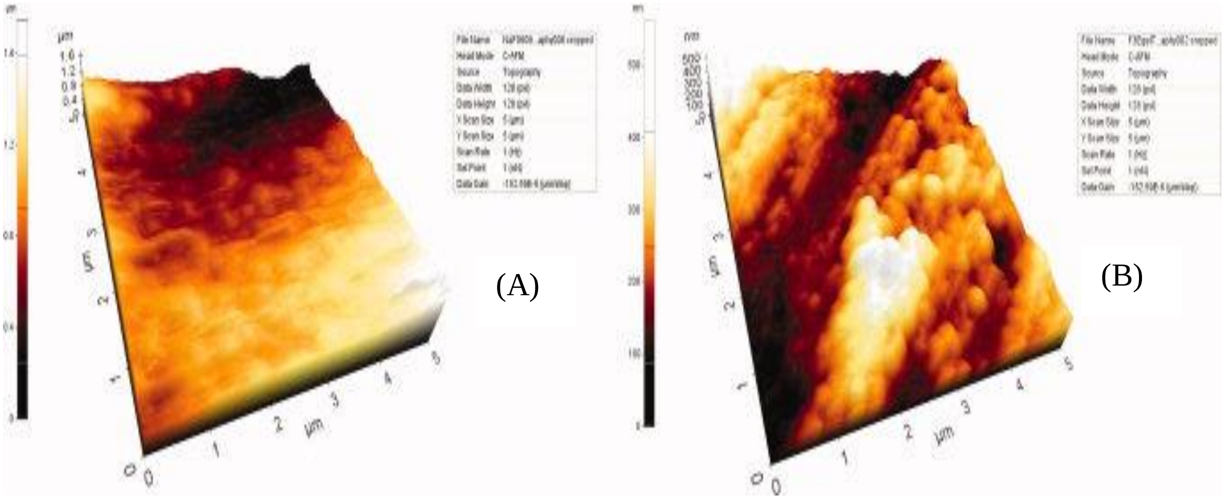

Figure 2.21 3D AFM pictures (A) of a Ti disc treated with 1% NaF (3,800 ppm F$^-$, pH 4.5), and (B) of a characteristic gel-treated (12,500 ppm F$^-$, pH 4.8) Ti sample [74]. The Ti discs treated with NaF solution displayed an almost 10 times increase in R_a and for gel-treated samples the AFM picture revealed deep corrosive regions and granular forms. Image size: 5 × 5 μm.

Kang *et al.* (2009) [85] studied the surface chemistry and morphology of four commercially available implants (TiUnite, Osseospeed, Osseotite and SLA) using XPS and Auger Electron Spectroscopy (AES) for surface chemistry analysis and depth profile of characteristic elements, while SEM was used for morphology description. XPS analysis was performed before and after Argon sputtering (Fig. 2.22). The study showed major differences in the surface properties of the four implants resulting from different surface treatments (blasting and acid etching for Osseospeed, Osseotite and SLA, electrochemical oxidation for TiUnite). The treatment in the first three implants does not alter the surface chemical composition of titanium, comprised mainly of TiO_2, although it does change the morphology. On the other hand, the surface treatment of TiUnite not only causes P incorporation into an anodic titanium oxide layer, but also creates microporous surfaces.

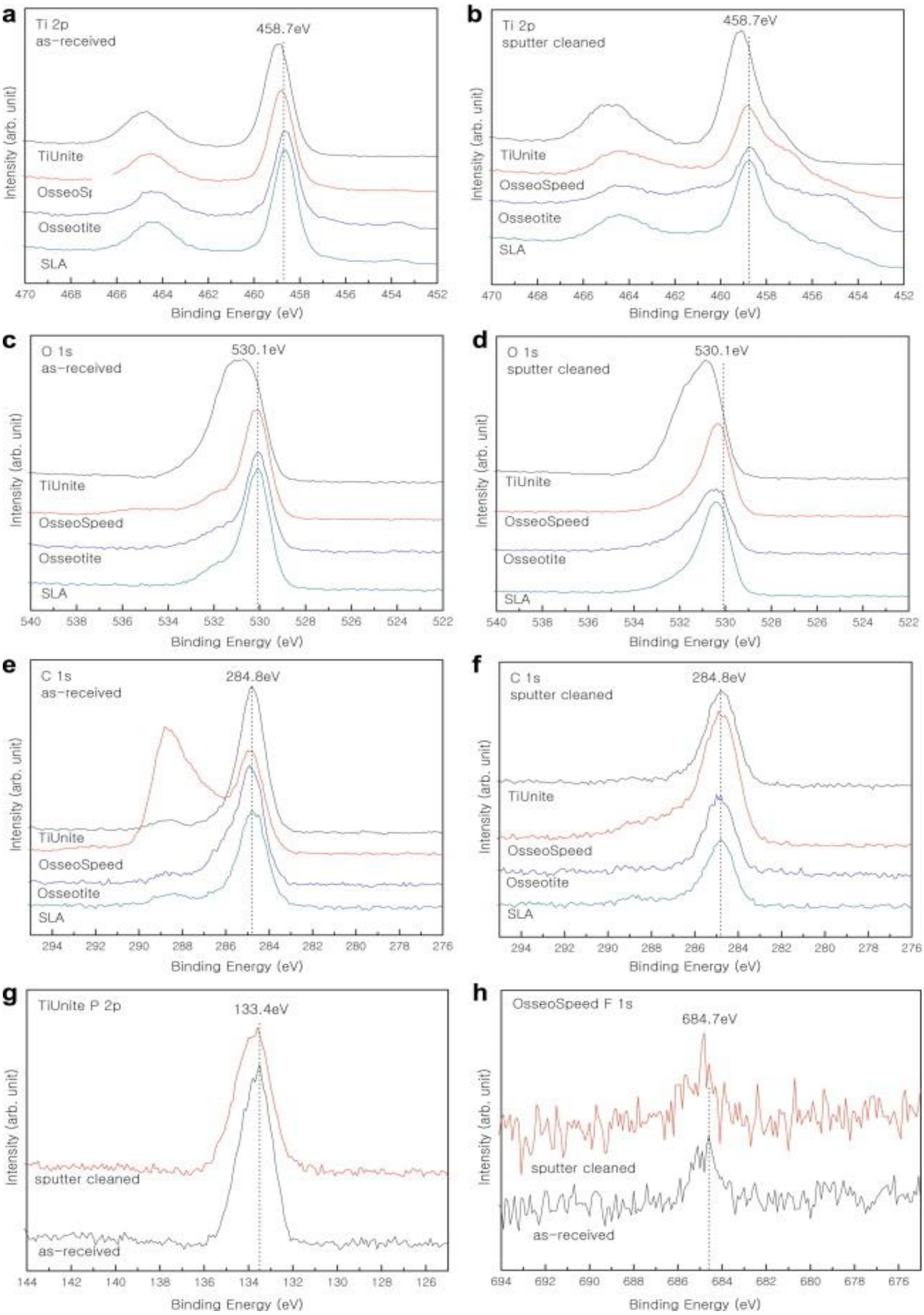

Figure 2.22 High-resolution XPS spectra of the as-received and sputter-cleaned samples: (a) and (b) Ti 2p spectra, (c) and (d) O 1s spectra, (e) and (f) C 1s spectra in all the samples; (g) P 2p spectra in TiUnite; (f) F 1s spectra in OsseoSpeed. Dashed lines indicate the binding energy of peak position on the as-received surfaces [85].

Watanabe *et al.* (2009) [86] studied the initial biological response following sand-blasted c.p. Ti dental implant placement to rat bone, using XPS for surface analysis. Semi-cylindrical bullets, 1.1 mm in diameter and 3.5 mm in length, were placed into the femurs of Wistar rats and then removed after either 3 hours or 7 days. In both cases, Ti, O, C and N were observed, while the adsorbed film (mainly proteins) was calculated to about 2.5nm. Ca and P were found in very small amounts, while the Ca/P ratios in both cases were very small compared to hydroxyapatite (HA). Ca and P distributions showed no distinct correlation between them, suggesting, thus, that no calcium phosphate compounds were formed in vivo in either implantation interval.

Petrini *et al.* (2006) [87] used XPS and SEM analysis to confirm the formation of a mixed zinc and titanium oxide on titanium surfaces, in an attempt to test if zinc oxide on titanium surface can act in as similar way as it does in the pharmaceutical industry, i.e. having antibacterial effects. After performing antibacterial assays, it was proved that zinc modification of titanium oxide surfaces can indeed reduce the viability of five strains of streptococcus in the oral cavity, suggesting this chemical modification as a new way of increasing implants' success rates, by diminishing the risk of bacterial infection.

Another attempt to create Ti surfaces that could prevent bacterial colonisation Xua *et al.* (2010) [88] studied surfaces of pure Ti (c.p. Ti), that were modified with increasing concentrations of Zn, using plasma immersion ion implantation and deposition (PIIID). XPS was used to characterise elemental surface compositions, whereas Streptococcus mutans were seeded onto the modified surfaces for 48 hours and then analysed with SEM to evaluate bacterial responses. It was shown that Zn can in this way be introduced onto a titanium surface, resulting in a modified surface that prevents adhesion of S.mutans.

Zinelis *et al* (2010) [34] performed surface analysis on two commercially available Zirconia implants -WhiteSky and Zit-Z- using XPS, Raman microanalysis, High-Voltage Energy-dispersive X-ray Spectroscopy (HV-EDX), Low Vacuum Scanning Electron Microscopy (LV-SEM) and X-Ray Diffraction (XRD). Studying chemical composition, XPS showed the presence of C, O, Zr and Y (collar) plus Al (root) at implant surfaces. Zr, Y and Al were detected in single, fully oxidized states. Na, K and Cl contaminants were found in trace amounts at implant root parts. Raman microanalysis revealed that the monoclinic zirconia volume fraction was higher at root surfaces than the collar, whereas no monoclinic phase was found at bulk regions. Data from the above surface analysis tools used, suggest that certain differences found between the tested implant systems may play a role in the different cellular and tissue response the two systems induce.

Lai *et al.* (2011) [89] used XPS to characterise nanocomposite ZrCN/amorphous carbon (a-C) coatings with different carbon contents that were deposited on a bio-grade pure Ti implant material. For the deposition of ZrCN/a-C coatings a cathodic-arc evaporation system with plasma enhanced duct equipment was used, and reactive gas (N_2) and C_2H_2 activated by the zirconium plasma in the evaporation process were utilised for the deposition.

Pisarek *et al.* (2011) [90] showed that titanium dioxide (TiO_2) layers formed on titanium substrates by etching in a solution of sodium hydroxide (NaOH) or hydrogen peroxide/phosphoric acid (H_2O_2/H_3PO_4, with a volume ratio of 1:1) are appropriate pretreatments for apatite-like coating deposition. Biomimetic calcium phosphate coatings were deposited on porous TiO_2 layers, by means of a two-step procedure (etching in an alkaline or acidic solution followed by soaking in Hanks' medium). The characterisation of topography of the TiO_2 layers was done with High-Resolution Scanning Electron Microscopy (HR-SEM) and AFM techniques, whereas XPS, as well as AES and Fourier Transform Infrared Spectroscopy (FTIR) techniques, were used to characterize the titanium dioxide layers before and after deposition of the calcium phosphate coatings, but also after protein adsorption.

Zhang *et al.* (2011) [91] tested the biocompatibility of SLA surfaces (sand blasted with long-grit corundum and acid etched) with further alkali and heat treatment (ASLA) or hydrogen peroxide and heat treatment (HSLA) for use in dental implantology. Surface analysis was performed using XPS, SEM, contact angle and roughness measurements. Surface bioactivity was further assessed by MC3T3-E1 cell attachment, proliferation, morphology, alkaline phosphatase (ALP) activity and calcium deposition on the sample surface. Cylindrical samples were inserted in beagles’ mandible and when assessed again, after micro-CT and histological examination it was shown that ASLA and HSLA surfaces had increased the bioactivity of the traditional SLA surface, while they demonstrated good levels of osseointegration.

Weinlaender *et al.* (1992) [92] used a Raman microprobe to investigate the crystallographic properties of three commercially plasma-flame-sprayed hydroxyapatite (HA) coatings on dental implants. Microspectra (5 μm) and macrospectra (100 μm) of the thin ceramic layers have been measured and compared to the spectra of amorphous and crystalline HA as well as to the spectra of tricalciumphosphate. All three coatings examined demonstrated spectra similar to the amorphous HA, but additionally they showed an extra band in their spectra indicative of some structure within the amorphous phase.

Frauchiger *et al.* (2004) [93] developed a new electrolyte containing both calcium - stabilized by complexation with ethylenediamine tetraacetic acid (EDTA) - and phosphate ions at pH 14. The anodic plasma-chemical (APC) process was used to modify c.p. titanium surfaces causing single-step combined chemical and morphological modification of titanium surfaces. The Ca-EDTA complex, negatively charged at high pH, promotes incorporation of high amounts of calcium into the APC coatings during the anodic (positive) polarization. XPS, Glow Discharge Optical Emission Spectroscopy (GD-OES), Raman spectroscopy (Fig. 2.23), SEM and tensile testing were used to assess this coating's surface properties, as well as to compare it to uncoated c.p. titanium surfaces and Ca-free APC coatings.

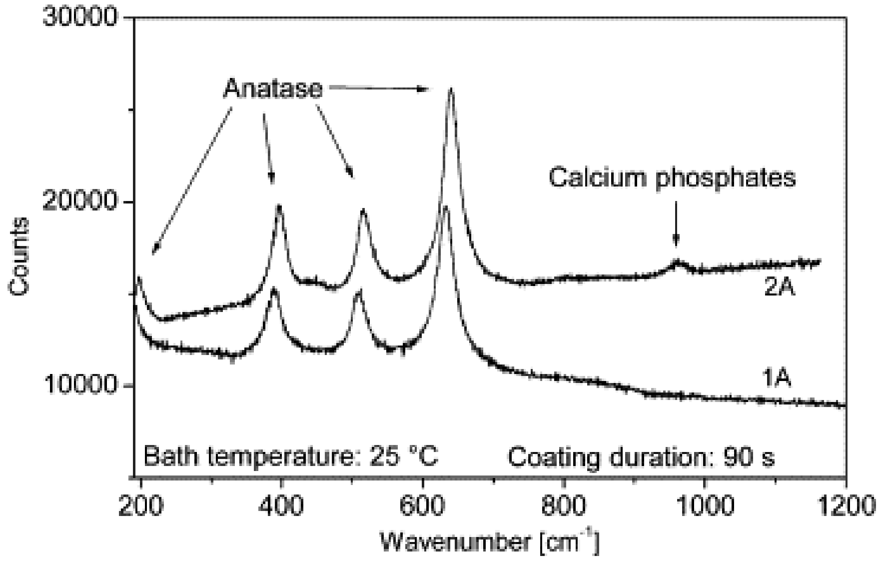

Figure 2.23 Raman spectra of samples 1A and 2A. The main crystal phase on both surfaces is anatase (TiO_2). The position of the additional peak found on surface 2A is typical for amorphous calcium phosphate. Samples 1A and 2A represent grade 4 cp titanium discs, 1mm in thickness and 7mm diameter. Same parameters were used for the fabrication of coatings in both samples, apart from the current, which was 80 mA for the 1A and 150 mA for the 2A [93].

Titanium nitride surface coatings - obtained by means of Plasma nitriding - have been widely used as wear resistant and biocompatible layers on titanium alloys. Micro-probe Raman Spectroscopy was used by Vasconcellos *et al.* (2007) [94] in order to investigate the TiN layer on a Ti_6Al_4V-ELI alloy, plasma nitrided at different substrate temperatures and, thus, to observe the changes in stoichiometry. Area ratios of the Ti and N related peaks were shown to be dependent on sample temperature during nitriding.

Machado *et al.* (2009) [95] studied the osseointegration of porous dental implants, which were made of grade 2 titanium and part of which underwent thermal and chemical treatment so as to deposit a biomimetic coating. The aim of the study was to evaluate the effect of this coating on the osseointegration. Raman spectroscopy, along with SEM and EDS were used to characterise the implant surface. Thirty albino rabbits were used and three coated and three control implants were inserted into their tibia, which were removed 15, 30 and 45 days. Calcium and Phosphorus were found on the surface with EDS, whereas Raman spectra exhibited an intense peak, characteristic of hydroxyapatite. Significantly more newly formed bone was apparent in 15 days, while the coated implants demonstrated a higher resistance to displacement by mechanical tests in 30 and 45 days.

Zirconia is an interesting and attractive material for use in dental implantology. Compared to titanium it has excellent esthetic properties [34] and shows limited plaque accumulation [96, 97] and similar peri-implant tissue compatibility [98]. On the other hand, fully ceramic implants have serious mechanical problems, mainly brittleness, and, additionally, there is no possibility of post implant position adjustments. Bozzini *et al.* (2011) [99] suggest a metal-based implant, consisting of metallic Zr, for the bulk of the implant and an electrochemically grown zirconia coating, resulting in contact of the ceramic with the biological environment but isolating the underlying metal from it. In this way, excellent mechanical properties are ensured for the implant bulk and superior bio-mechanical properties for the implant surface. The surface was exposed to SBF solution with and without glycine and electrochemical measurements revealed excellent corrosion resistance of Zr in both environments but better when glycine is added as well. Raman spectroscopy (Fig. 2.24), in addition to FTIR and visible reflectance spectroscopies were used to analyse the surface before and after the exposure to SBF solutions.

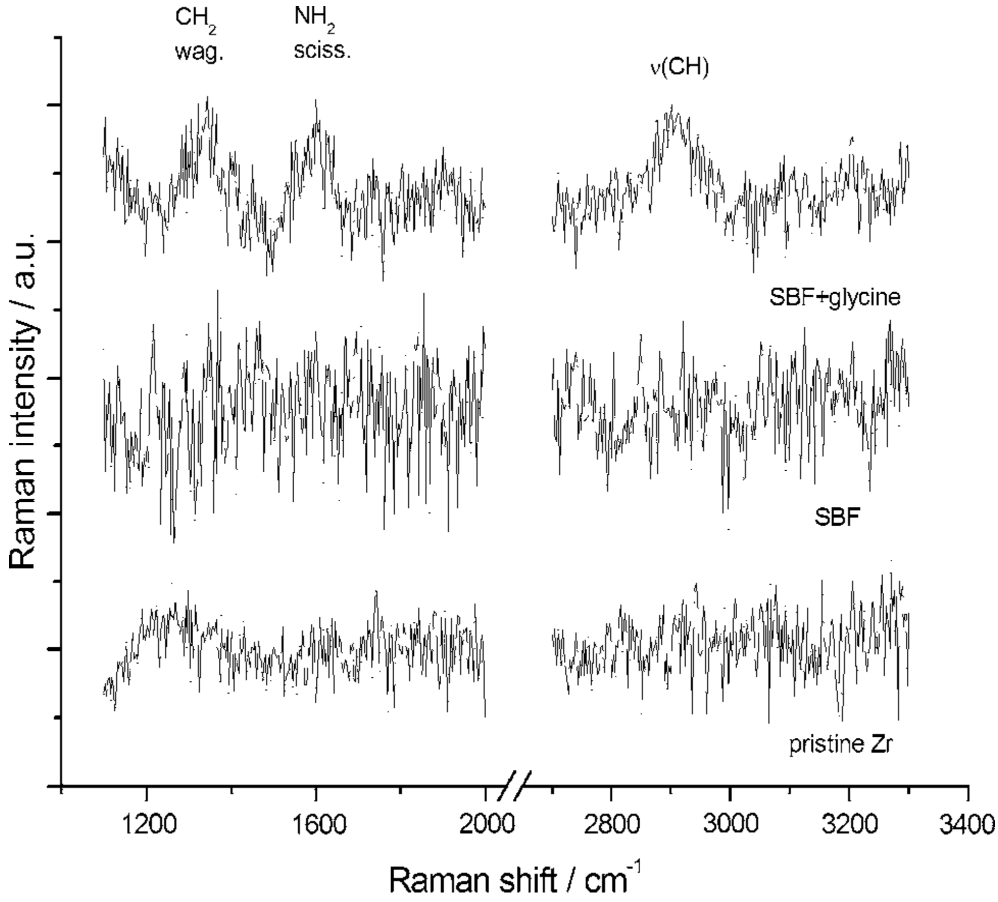

Figure 2.24 Surface Raman spectra of Zr surfaces before and after exposure for 170 h to SBF without and with added glycine [99]. The data are rather noisy, but there are clear signs in the two upper most spectra.

One surface modification made to enhance osseointegration includes Hydroxyapatite coating of the titanium surface. Hydroxyapatite (HA: $Ca_{10}(PO_4)_6OH_2$) is a biocompatible and bioactive ceramic material, which unfortunately shows poor adhesion to titanium substrate in the long term and increased levels of degradation. In an attempt to improve the mechanical properties, Melero *et al.* (2011) [100] incorporated TiO_2 in the HA coating, producing coatings made of HA 80% and TiO_2 20% (by weight) on Ti_6Al_4V by High-Speed Thermal Spray. Raman spectroscopy and XRD were used to characterise the crystalline phases, the microstructure of the coating was made with SEM, while its ability to form an apatite layer was assessed through immersion to SBF with positive results.

AlSamak *et al.* (2012) [101] studied the morphological and structural characteristics of four different types of orthodontic mini-implants made of Ti_6Al_4V alloy. Surface texture and elemental composition were examined by scanning electron microscopy and energy dispersive X-Ray microanalysis. Surface 3D roughness was estimated by optical profilometry. No significant differences were detected in amplitude surface roughness parameters (S_a, S_z) between the implants. However, differences were found in hybrid (S_{dr}, S_{ds}) and functional (S_{ci}) parameters. Significant differences were found in the surface area of the threaded parts. The statistically significant differences found in 3D surface roughness parameters (hybrid and functional) and pull-out strength may account for variations in their clinical performance.

Silva *et al.* (2000) [102] studied four commercially pure titanium cylindrical dental implants with different surface conditions: as-machined, Al_2O_3 blasted with Al_2O_3 particles, plasma-sprayed with titanium beads and electrolytically coated with hydroxyapatite. The surface roughness was quantitatively characterised using Optical Profilometry. It was found that the plasma-sprayed implant and the hydroxyapatite implant demonstrated the roughest surface, followed by the alumina-blasted implant and, last, the as-machined one.

Juodzbalys *et al.* (2003) [103] investigated the creation of an acid etched implant surface -using different acids and exposure times- that would result in a surface similar to the one gained after sandblasting as well as acid etching; they compared this surface with existing surfaces of commercially available screw-type implants. The surfaces of five commercially available screw-type implants and the experimental ones were comparatively analysed using optical profilometry and it was concluded that, in general, the experimental surface was significantly rougher than the selected commercially available implants and similar to the SLA treated surface.

Dental implants with hydroxyapatite thin-film coatings have demonstrated improved bone-to-implant bonding, since fibrous capsule formation is prevented after implantation. The interest in hydroxyapatite specifically as a biomaterial developed mainly due to its chemical resemblance to apatite [104], a natural mineral comprising most of the inorganic components in bones and teeth, and its spontaneous interfacial osseointegration when implanted [105]. In an attempt to accurately characterize the physical and chemical properties of its surfaces, Lu *et al.* (2000) [105] examined the surfaces of six biologically interesting calcium phosphate (CaP) phases (hydroxyapatite, dibasic calcium phosphate dihydrate, dibasic calcium phosphate, monobasic calcium phosphate, β-tribasic calcium phosphate, octacalcium phosphate) with X-ray photoelectron spectroscopy (XPS) and time-of-flight secondary ion mass spectrometry (TOF-SIMS). They found that the intensity of an O (1s) shake-up satellite correlates with the phosphate oxygen content.

Together with the Ca/P and O/Ca XPS peak ratios, this feature helps provide identification of the CaP phase(s) present in the surface of unknown samples and establish their mole fractions, as proven with a bone sample.

To gain a better understanding of interactions at the metal oxide surface and the processes involved with hydroxyapatite incorporation into living tissue and metal oxides, Chusuei *et al.* (1999) [106] exposed calcium phosphate (CaP) in aqueous solution to thin-film TiO2 surfaces at predetermined times ranging from 10 min to 20 h using a liquid reaction apparatus (LRA). Surface analysis was then performed using X-ray photoelectron (XPS) and Auger electron (AES) spectroscopies and time-of-flight secondary ion mass spectrometry (ToF-SIMS) with polyatomic primary ions. XPS revealed that ‘CaP’ nucleated and grew on the TiO_2 surface, with phosphate groups growing on top of an initial 2-dimensional (2D) Ca-rich layer. AES depth profiling of a 4-h solution exposure complemented this finding and gave additional evidence for 3-dimensional (3D) phosphate islands forming on top of the calcium. The predominant phase on the surface was brushite, as shown with ToF-SIMS analysis of CaP adsorbed on the surface.

Jung *et al.* (2012) [107] studied the surface characteristics and bond strength produced using a novel technique for coating hydroxyapatite (HA) onto titanium implants. HA was coated at a low temperature on the titanium implant surface using a super-high-speed (SHS) blasting method with highly purified HA. Crystallinity was evaluated on the novel HA-coated disc by X-ray diffraction analysis. Surface roughness and contact angles were measured. Resorbable blast medium (RBM) discs were prepared and used as control discs. To evaluate exfoliation of the coating layer, implant surgery on mandibles from 7 mongrel dogs was performed two months after extraction of premolars. The used novel HA-coated implants were removed two months after placement and their surface was microscopically evaluated. These HA-coated implants showed increased roughness, crystallinity, and wettability when compared with RBM implants, while a uniform HA coating layer was formed on the titanium implants with no deformation of the titanium surface microtexture.

Among other factors, hydrophilicity is believed to play a role in the osseointegration of dental implants. The proliferation of the cells increases with surface wettability and the fibroblasts have greater adhesion on hydrophilic surfaces than on hydrophobic surfaces [108]. Rupp *et al.* (2011) [109] analysed the dynamic wetting behaviour of nine screw-type implant systems from eight manufacturers by tensiometry, and examined its relationship to surface topography. Contact angle and 3D profilometry measurements were taken, whereas all implant surfaces were characterized by SEM. A range from fully wettable/superhydrophilic to virtually unwettable/hydrophobic was observed on the implant surfaces examined. Contact angle measurements with values from 0^o (SLActive) to 138^o (OsseoSpeed) varied considerably, demonstrating statistically significant differences between implants.

Increased wettability may also contribute to re-osseointegration of failing implants due to peri-implantitis [110]. Duske *et al.* (2012) [111] used an argon plasma jet with different oxygen admixtures to treat titanium discs with different topologies, i.e. machined, SLA, SLActive, diamond bur-treated or Airflow-treated. More specifically, a cold atmospheric pressure gas-discharge plasma was applied to reduce water contact angles on titanium discs with different surface topography and to improve the spreading of osteoblastic cells. Water contact angles were measured before and after plasma treatment. Contact angle of titanium discs (baseline values: 68^o-117^o) were significantly reduced close to 0^o irrespective of surface topography after the application of argon plasma with 1.0% oxygen admixture for 60 s or 120 s, indicating that cold plasma could be potentially helpful in the treatment of periimplantitis.

Lu *et al.* (2012) [112] showed that the storage method significantly influences the physicochemical properties and bioactivity of the titanium surface. Acid-etched titanium discs (Sa = 0.82 μm) were placed in a sealed container (traditional method) or submerged in the ddH_2O/NaCl solution (0.15 mol L^{-1})/ $CaCl_2$ solution (0.15 mol L^{-1}), and new titanium discs were used as a control group. Preventing titanium surfaces from contact with the atmosphere reduced hydrocarbon contamination and increased hydrophilicity extensively on the surfaces without changing surface topography. XPS analysis showed that the carbon concentration of the titanium surface in a sealed container increased with storage time, indicating the hydrocarbon contamination in the ambient atmosphere is unavoidable, while the carbon level of the discs stored in solution was stable and only changed slightly even after four weeks storage time. This study has revealed that the storage method significantly affected their biocompatibility, including protein adsorption and osteoblast cell culture. Storing the titanium discs in solution can protect the surface from the hydrocarbon contamination of surrounding environment and enhance surface energy.

Ueno *et al.* (2010) [113] studied the effect of ultraviolet photoactivation of titanium on osseointegration on a rat model. The objective of the study was to determine whether ultraviolet (UV) light treatment of titanium implants could improve osseointegration in order to sufficiently overcome the negative aspects of shorter implants in a rat femur model. Acid-etched 2 mm (longer implants) and 1.2 mm (shorter implants) titanium implants were used. Some of these implants were treated with UV light for 48 hours prior to surgery. The strength of osseointegration generated by these implants was determined using a biomechanical implant push-in test in a rat model. Peri-implant osteogenesis was evaluated by SEM for tissue morphology and energy dispersive X-ray spectroscopy for elemental composition. It was suggested that UV treatment of the shorter implants significantly increased their push-in value, resulting in a 100% higher value than untreated longer implants at week 2 and a push-in value that was equivalent to that of the untreated longer implants at weeks 4 and 8. Scanning electron micrographs and energy dispersive X-ray spectroscopic examinations after push-in testing revealed that the UV-treated implant surfaces were covered more extensively by bone or tissue remnants containing calcium and phosphorous than the untreated surfaces. The authors suggested that UV pre-treatment of titanium surfaces led to them converting from hydrophobic to superhydrophilic, thus enhancing osseointegration deficiencies for shorter implants, although the cause-result relationship between the acquired superhydrophilicity and biologic effects remained unclear.

Ueno *et al.* (2010) [114] also studied the enhancement of a bone-titanium integration profile with UV-photofunctionalized titanium in a gap healing model. In order to evaluate the potential of UV-photofunctionalized titanium surfaces to overcome compromised bone-titanium integration, titanium in rod and disk forms was acid etched and then stored for 4 weeks under dark ambient conditions. Titanium rods with and without UV pre-treatment were placed into a rat femur with (contact healing) or without (gap healing) contact with the innate cortical bone. A biomechanical push-in test, micro-CT bone morphometry and surface elemental analysis were performed after 2 weeks of healing. The results showed that UV-treated implants in the gap healing condition produced a strength of bone-titanium integration equivalent to that of untreated implants in the contact healing condition. Bone volume around UV-treated implants was 2- to 3-fold greater than that around the untreated implants in the gap healing model. The rate of cell proliferation, alkaline phosphatase activity, and calcium deposition in femoral periosteal cells and in bone marrow-derived osteoblasts indicated a synergistic effect of UV-treated titanium with biological signals from bone marrow-derived osteoblasts. Despite the limitations of the study, it was suggested that UV-photofunctionalized titanium surfaces may overcome the challenging condition of bone-titanium integration without cortical bone support. UV treatment of implants induced marked improvements in the behaviour of bone formation and quantity and quality of bone tissue around the implants.

Ultraviolet light-induced superhydrophilicity of TiO_2 was discovered in 1997 [115]. In this procedure, UV irradiation is thought to create surface oxygen vacancies at bridging oxygen sites. Wetting results from alteration of surface chemistry by removal of hydrocarbon due to the photocatalytic activity of TiO_2 [116] .

In addition to titanium surfaces, the use of ultraviolet light as a way to enhance hydrophilicity was also tested on tetragonal zirconia polycrystals (TZP). Watanabe *et al.* (2012) [117] studied the changes in surface properties of tetragonal zirconia polycrystals (TZP) after hydrophilic treatment, and attempted to determine the effect of such changes on initial attachment of osteoblast-like cells. The water contact angle was determined and surface analysis was performed using an X-ray photoelectron spectroscopy. Blast/ Etch, O2-Plasma and UV specimens showed superhydrophilicity, and these hydrophilic treatments to TZP elicited a marked decrease in carbon content and an increase in hydroxyl groups. The initial attachment of osteoblast-like cells was enhanced, while a change in cell morphologies was noted. This study concluded that Blast/ Etch, O2-Plasma, or UV treatment have potential in the creation and maintenance of superhydrophilic surfaces and enhancing initial attachment of osteoblast-like cells.

The use of UV-radiation on titanium surfaces was also studied as a sterilization method. Riley *et al.* (2005) [110] tried to evaluate whether the TiO_2 at the surface of a dental implant is sufficiently photoactive to eradicate bacteria when illumined with low intensity light, taking into consideration that commercial titanium dental implants are coated with nanostructured $TiO_{2.}$ The photoactivity of dental implants was established by studies of the photoenhanced decomposition of Rhodamine B (a staining fluorescent dye). In vitro studies to establish the influence of irradiating an implant with UV light that is immersed in a solution containing Escherichia Coli were performed, showing that that under low UV intensity irradiation, bacteria are killed at a rate of approximately 650 million/cm^2 of implant per minute. The clinical significance of the study laid on the suggestion that illumination of dental implants with UV light may be a suitable treatment for periimplantitis.

Wennerberg and Albrektsson (2010) [71] published “a review of current knowledge and opinions on implant surfaces” in an attempt to identify essential surface parameters, to present an overview of surface characteristics at the micrometer and nanometer levels of resolution relevant for the four most popular oral implant systems, to discuss potential advantages of nanoroughness, hydrophilicity, and biochemical bonding and, last, to suggest a hypothetical common mechanism behind strong bone responses to novel implant surfaces from different commercial companies. Four major companies' oral implants were tested and the results demonstrated variation in average surface roughness (Sa) from 0.3 to 1.78 μm and in the developed surface area ratio (Sdr) from 24% to 143%. When the different implants were examined at a nanometer level, similarly significant variation was also evident in Sa with regard to nanometer roughness. Interestingly, novel implants from Biomet 3i, AstraTech, and Straumann differed from their predecessors in physicochemical properties, microroughness as well as nanoroughness. Subsequently, scanning electron microscopy examination of these novel implant surfaces at high magnification revealed the presence of nanoroughness structures that were not present in their respective predecessors. This finding provided a probable mechanism that could explain the stronger bone responses to these implants compared to adequate controls, initiating in this way a scientific interest in the newly discovered nanostructures.

Svanborg *et al.* (2010) [118] studied twelve different commercial screw-shaped oral implants with various surface modifications using scanning electron microscopy and a white light interferometer, appropriate for detection of nanoscale roughness in the vertical dimension. In an attempt to evaluate if there is any correlation between nanometer surface roughness and the more well-known micrometer roughness on the implants, they found that an implant that was smooth on the micrometer level was not necessarily smooth on the nanometer level. For that reason, it was suggested that a nanometer-scale characterization might be useful in order to fully comprehend the relationship between the properties of an implant surface and its osseointegration behaviour.

Modification of dental implant surfaces with nanoscale characteristics has been described as a way to improve osseointegration. Jimbo *et al* (2012)[119] described a nanoscale Hydroxyapatite (HA)-coated implant that improved bone nanomechanical properties. Twenty threaded titanium alloy implants, half prepared with a stable HA nanoparticle surface and half grit-blasted, acid-etched, and heat-treated (HT), were inserted into rabbit femurs. Morphological and topographical characterization was performed prior to surgical insertion. Following three weeks of healing, the samples were removed. Nanoindentation was performed and it was proven that the tissue quality was indeed significantly enhanced around the HA-coated implants.

In order to test whether nano-Hydroxyapatite may result in enhanced osseointegration compared to nano-titania structures, Meirelles *et al.* (2008) [120] applied

Hydroxyapatite (HA) or titania nanostructures on smooth titanium implant cylinders. Microstructures were removed from the surface to ensure that the observed bone response depended only on the nanotopography and/or chemistry of the surface. The study showed that nano-titania-coated implants had an increased coverage area and feature density, forming a homogenous layer compared to nano-HA implants. No proof of increased bone formation to nano-HA-modified implants was noted compared to nano-titania-modified implants. It was suggested that the presence of specific nanostructures dependent on the surface modification exhibiting different size and distribution did modulate in vivo bone response.

Meirelles *et al.* (2008) [120] also suggested for the first time that that early bone formation is dependent on the nanosize hydroxyapatite features, but it is uncertain if this is an isolated effect of the chemistry or of the nanotopography or a combination of both. For the purpose of the study, electropolished titanium implants were prepared to obtain a surface topography in the absence of micro structures, since these alter bone formation. The implants were then split into two groups. The test group was modified with nanosize hydroxyapatite particles, whereas the other group served as a control group and was therefore left uncoated. Topographical evaluation showed increased nanoroughness parameters for the nano-HA implant and higher surface porosity compared to the control implant. Chemical characterization revealed calcium and phosphorous ions on the modified implants, whereas the control implants consisted of pure titanium oxide. Histological evaluation demonstrated significantly increased bone formation to the coated ($p < 0.05$) compared to uncoated implants after 4 weeks of healing.

Wennerberg *et al.* (2012) [121] investigated the evolution of nanostructures on the SLActive surface, as a function of time, storage conditions, material dependence and tried to identify the time frame in which the reorganization of the outermost titanium oxide layer into well-defined nanostructures takes place. They used Titanium grade 2 discs in seven different modes (different surface treatments and storage conditions). SEM, interferometry, contact angle measurements and XPS were used for the surfaces' evaluation. It was demonstrated that the evolution of nanostructures took 2 weeks; thereafter they exhibited stability over time. In conclusion, they showed that acid etching in conjunction with storage in aqueous solution (either water or NaCl solution) is responsible for the reorganization of the outermost titanium oxide layer into well-defined nanostructures.

3. MATERIALS AND METHODS

3.1 Sample Selection

In order to do the surface analysis on the above implant surfaces, Titanium disks (5mm diameter x 1mm height) were obtained from Straumann Schweiz (Basel, Switzerland). 6 SLA disks were received in aluminium foil sealed in a plastic bag and 6 SLActive discs were received in sealed plastic containers filled with saline solution.

The above discs were treated with the same processes used on the commercial products. They are made of cp Ti (grade 2) and after production they were surface treated as follows. The SLA samples have been sand blasted and acid etched on one side and then washed, while the other side has only been acid etched and washed afterwards. On the other hand, the SLActive samples have undergone the same treatment initially with the only difference lying after the acid etching stage, where they were rinsed under protective N_2 gas conditions and stored in isotonic NaCl solution. Just like on the SLA samples, one side of the SLActive samples has not been sandblasted. In order to distinguish the surface of interest, the non-sandblasted side on all samples has characteristic concentric rings on it, which are readily visible under an optical microscope.

With regard to the study of the surface chemical composition of the samples, only a single crystal of rutile TiO_2 was studied under a Raman spectrometer as an anatase crystal was not available. The same crystal was used to calculate the contact angle of water on rutile.

The methods used for the study included: X-Ray Photoelectron Spectroscopy (XPS), Raman spectroscopy, Optical 3D Profilometry and Contact Angle measurements. Hanks' Balanced Salt Solution or HBSS (Sigma Aldrich, UK) is a cell culture medium and its composition is given in Table 3.1 below. In this work it is used to simulate the tissue fluid environment around the implant [122-124].

HANKS solution	
0.137 M NaCl	5.4 mM KCl
0.25 mM Na_2HPO_4	0.44 mM KH_2PO_4
1.3 mM $CaCl_2$	1.0 mM $MgSO_4$
4.2 mM $NaHCO_3$	Phenol Red

Table 3.1 HANKS solution composition

3.2 Experimental Methodology

3.2.1 Optical 3D Profilometry

The surface roughness was measured with optical 3D optical profilometry. Given that mechanical and chemical attachment are the main mechanisms of bone-implant attachment, implant surface roughness affects mechanical attachment by allowing the bone to grow through the pores or around other features associated with roughness on the implant surface. In addition, surface roughness has been associated with increased cell response to titanium implants [46, 125] indicating that roughness does contribute to osseointegration not only mechanically. The hydrophobic character of a surface can be altered by changes in surface tension and surface energy, increasing the adsorption of organic molecules like proteins and, thus, positively increasing its biocompatibility. Other studies [126, 127] investigating the effect of roughness on bone attachment, have also shown the positive correlation between increased surface roughness and improved tissue response to titanium dental implants.

In this experiment, a ContourGT 3D optical surface profiler (Veeco) was used for measurements in order to assess the surface profiles of the samples. This instrument uses light interference detected by a CCD camera. The settings used were 50 x magnification, back scan and length of scans were both 10 µm, the threshold was set at 0.001 % and green light source was used. Initial scans were performed and after tilt correction, measurements were taken. No other corrections were made. Both SLA and SLActive discs were measured as received only. SLActive discs were dried by dabbing them with a paper towel before measurements. We would have preferred air, N_2 or low vacuum drying but these were not available due to time constraints. Three random SLA and SLActive specimens were selected and measured, carrying out one measurement for each sample. Data were obtained using the Vision 64 Software. The surface roughness parameters measured were S_a (arithmetic mean deviation), S_q (root mean square roughness), S_z (ten point height over the complete surface), S_p (maximum profile peak height), S_v (Maximum profile valley depth), S_{sk} (skewness) and S_{ku} (kurtosis). We decided to limit our measurements only to the amplitude parameters as this is the most commonly used parameter. Due to time constraints further measurements were not possible.

3.2.2 Contact Angle Goniometry

The surface wettability was tested using an FTÅ188 Contact Angle and Surface Tension Analyser (First Ten Angstroms Inc.) several times for each sample. The sessile drop method was used to measure contact angles in this experiment on a plane surface with distilled water. These are the most common measurements made with video instruments. An approximately 6 μl droplet of pure water was suspended from the tip of the microliter syringe supported above the sample stage. Once the drop - produced by hand - settled on the surface, an image of the droplet was captured using a CCD camera attached to the equipment (spreading time of just a few seconds). The contact angle was then calculated using the FTA32 software. The camera looks at the drop from its side and measures the liquid-vapour profile and the liquid-solid baseline and the software solves for the contact angle. The snapshot that was analysed each time was always checked by eye and, if necessary, the baseline used in the calculation was adjusted. Due to surface effects, differences between the right and left hand side angles were observed; for that reason, an average value of the two measurements was taken each time.

Both SLA and SLActive discs were initially studied as received. (SLActive were dried first). In addition, measurements were made on the side of the test disks that were only acid-etched, in order to assess the impact of sandblasting in the wettability of the specimens. 2 specimens x 6 measurements and 1 specimen x 5 measurements were taken.

Mean value of the measurements performed on each surface was calculated (i.e. the mean of the 6 or 5 measurements per sample). In addition, measurements were made on a single crystal of rutile TiO_2 (100). Tests on both sides of the single crystal were run three times each side, six in total.

3.2.3 Raman Spectroscopy

In order to determine the phase of the surface oxide in real dental implant materials Raman spectroscopy was used on both types of discs. Spectra were taken and measured using a 1000 Micro-Raman Spectrometer (Renishaw) with CCD camera (detection system) under the following conditions: 3000-150 cm^{-1} range, around 1 cm^{-1} resolution, 1800 lines/mm grating, laser wavelength of 515 nm and laser intensity at the sample of only a few mW. The microscope was focused using a white light, which then was switched to the laser before the measurement was taken. The microscope operated using a 50X (130 x 174.7 μm^2) magnification lens, which resulted in a laser spot size with magnitude in the range of tens of microns. Three scans were taken and averaged for each sample in order to remove or reduce the effects of stray light and other noise.

The titanium surface oxidizes spontaneously forming a titanium dioxide (TiO_2) layer in air. TiO_2 is most commonly found in one of two crystal structures, rutile and anatase [128].

The most common Raman active peaks of Anatase, Rutile, Brookite and amorphous titania are shown below in Table 3.2. The Raman peak at around 240 cm^{-1} is known to be a compound vibrational peak due to multiple-Phonon scattering processes, which is also considered as a characteristic Raman peak of Rutile type TiO_2 [129].

Anatase	Exhibits a strong band at 144 cm^{-1} and six Raman-active peaks at 144 cm^{-1} (E_g), 197 cm^{-1} (E_g), 399 cm^{-1} (B_{1g}), 513 cm^{-1} (A_{1g}) and 640 cm^{-1} (E_g) [130].
Rutile	Exhibits Raman-active peaks at 143 cm^{-1} (B_{1g}), 447 cm^{-1} (E_g), 612 cm^{-1} (A_{1g}) and 826 cm^{-1} (B_{2g}). An additional band that is observed at around 250 cm^{-1} is usually treated as a secondary scattering feature [130].
Brookite	Shows 36 Raman active modes ($9A_{1g}+ 9B_{1g}+ 9B_{2g}+ 9B_{3g}$) and the most intense Raman band at around 153 cm^{-1}. Some of the Raman active peaks are as follows: at 127, 154, 194, 247, 412, 640 cm^{-1} (A_{1g}), at 133,159,215,320,415,502 cm^{-1} (B_{1g}), at 366, 395, 463, 584 cm^{-1} (B_{2g}) and at 452 cm^{-1} (B_{3g}) [131].
Amorphous titania	Exhibits bands near 680, 580, 450, 350 and 250 cm^{-1} [132].

Table 3.2 Anatase, Rutile, Brookite and Amorphous Tiatania Raman peaks and –in brackets- their vibrational modes [130-132].

The same surface treatment was carried out for both for SLA and SLActive discs:

Ti disks as received (ar)
Rinsed in distilled H_20
Rinsed in Acetone/Ethanol/Distilled H_20
Hanks' 2 months, UV treatment
Hanks' 2 months, no UV treatment

A high intensity Hg vapour UV source was used, which produces UV at 253.7 nm and 184.9 nm. The latter is responsible for the ozone production.

Depending on the type of the sample, a variety of scanning periods and runs were used. It was found that generally longer running times were required for SLA samples than for SLActive samples. As a result, SLA samples were generally run for 150 seconds by 5 runs, while SLActive samples were run for 30 seconds by 1 run. For the first part of the experiment, 6 samples were studied, 3 SLA and 3 SLActive discs. 1 SLA and 1

SLActive disc were studied as received, while another set of SLA and SLActive discs were rinsed in distilled water and studied afterwards. A third set of the two discs were rinsed with Acetone, Ethanol and distilled water before measurements were taken. Three scans of each sample were taken for all the above sets of discs and the average for each sample was calculated.

For the second part of the experiment 2 SLA discs and 2 SLActive discs were used. 1 SLA disc was UV treated for 20 min, while the other SLA disc was not. The same procedure was applied to the SLActive samples. Samples were incubated at 38°C for 24 hours and then stored in distilled water. They were then incubated for further 48 hours before being stored in Hanks' solution at room temperature for about two months (for convenience). Three scans of each sample were again taken and the average was calculated.

3.2.4 X-Ray Photoelectron Spectroscopy (XPS)

In order to quantify the elemental composition and chemical state on the titanium discs as well as to monitor the changes in the surface of Titanium before and after exposure to biological fluids we used the Kratos Axis Ultra XPS Spectrometer at Nottingham University, UK.

The samples as received (*n* = 2) were placed in the ultra-high vacuum chamber of the X-ray photoelectron spectrometer. Three random regions were located on each sample and analysed under the following conditions: Al Ka (1486.7 eV) monochromated anode, a 165 mm mean radius hemispherical electron energy analyser, 10^{-9} mbar pressure, around 90◦ electron take-off angle and 5mm×5mm sampling area. Selected 45° take-off angles scans were also obtained, where the take-off angle is defined as the angle between the surface normal and the axis of the analyser lens.

Survey scans (80eV pass energy) were taken from each region to identify the elements present on the surface. Then, high resolution narrow scans (20eV pass energy) were recorded over the predominant peaks and the elemental binding states were determined. All spectra were aligned on the binding energy scale to the C 1s peak arising from adventitious hydrocarbons (–CH2–, 284.8 eV BE, 0.278 Relative Sensitivity Factor). The core level data were analysed using the CASA XPS software package (Casa Software, UK). A Shirley background was subtracted from the data and 70:30 Gaussian: Lorentzian peaks fitted to give binding energy positions. The fitted peak areas in conjunction with relative intensity factors allowed the elemental ratios at the surface to be quantified. The depth of analysis for metals is estimated to around 3 nm [133] at normal emission. This reduces to sin45^o at the grazing emission i.e. around 2.1 nm.

The same treatment took place both for SLA as well as SLActive discs:

Ti disks as received (ar)
UV treatment
Hanks' 24h at 38 ^{o}C (UV and no UV treatment) and rinse with ultrapure water
Hanks' 72h at 38 ^{o}C (UV and no UV treatment) and rinse with ultrapure water

A high intensity Hg vapour UV source was used, which produces UV at 253.7 nm and 184.9 nm. The latter is responsible for the ozone production.

For the first part of the experiment two SLA discs and two SLActive discs were used. One SLA disc was UV treated for 20 min, while the other SLA disc was not. The same procedure was carried out for the SLActive samples. X-Ray Photoelectron spectroscopy measurements were taken for all four samples. Following the above measurements, all samples were put in Hanks solution and incubated for 24 hours at 38^0 C in a water bath. The samples were rinsed with ultrapure water and X-Ray Photoelectron spectroscopy measurements were taken for all 4 samples again.

After XPS analysis the samples were placed in doubly distilled deionized water. Immediately prior to the final allocation of XPS time the samples were removed from the distilled water and incubated in Hanks' solution for 48 hours at 38^o C in a water bath. Again the samples were rinsed in ultrapure water prior to XPS analysis.

3.3 Statistical analysis

Statistical variance testing of XPS data could not be carried out between the SLA and SLActive materials since only one sample of each group was analysed by XPS. Whilst three areas of the samples were studied this does not allow us to draw definitive conclusions about the differences between the two sample sets. However the XPS data allow qualitative comparisons of the surface chemistry to be made. The roughness parameters between the implant groups were evaluated by a t-test. The experimental results are expressed as mean ± standard deviation (SD). In all comparisons a 95% confidence level was used (α:0.05). Statistical analysis of the roughness parameters and contact angle measurements was performed by SPSS software Version 20.

4. RESULTS AND DISCUSSION

4.1 Optical Profilometry

Surface profile images of SLActive and SLA samples are displayed at Figures 4.1 and 4.2 respectively.

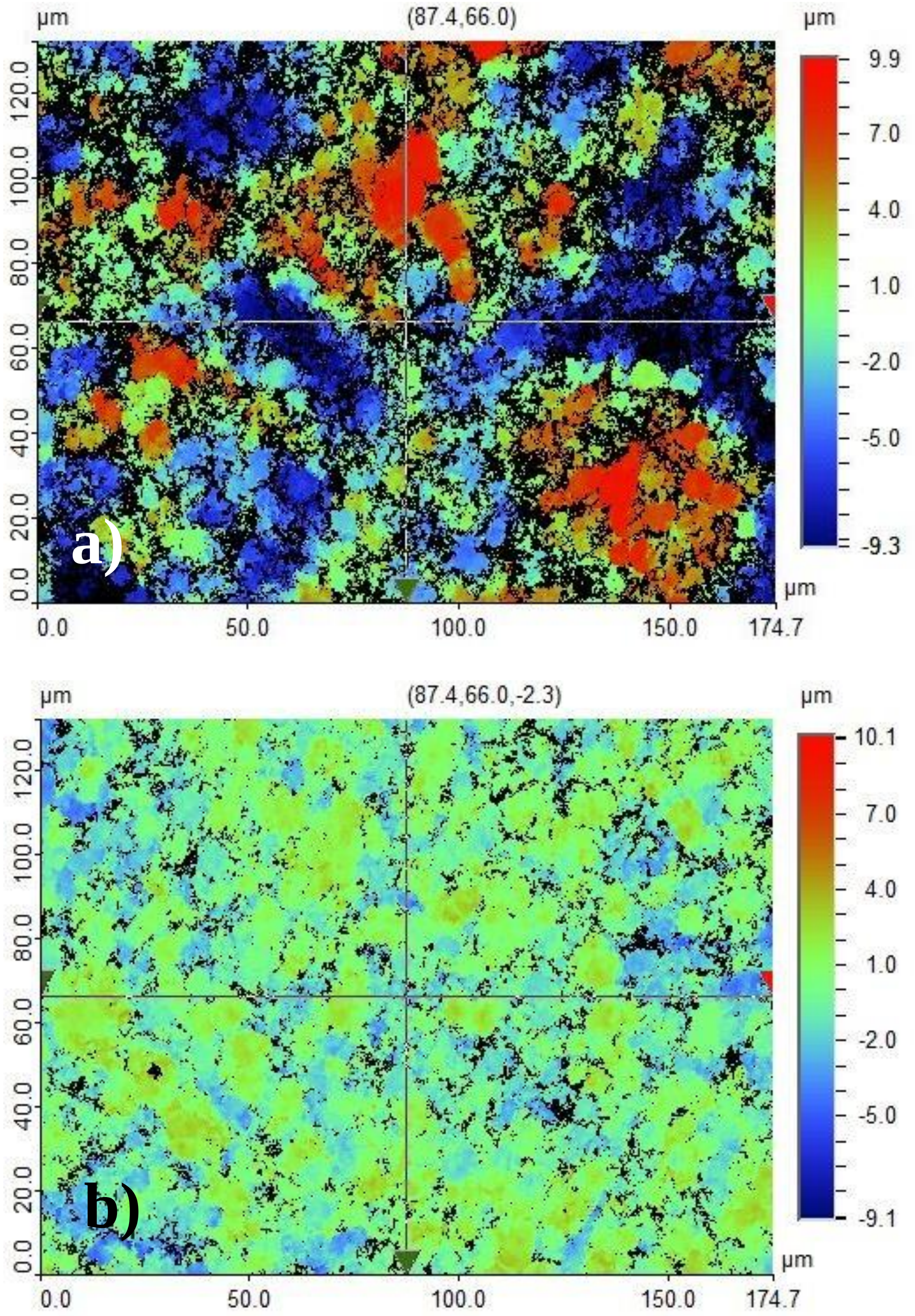

Figure 4.1 Surface 3D profilometry images of a) SLActive and b) SLActive without sandblasting

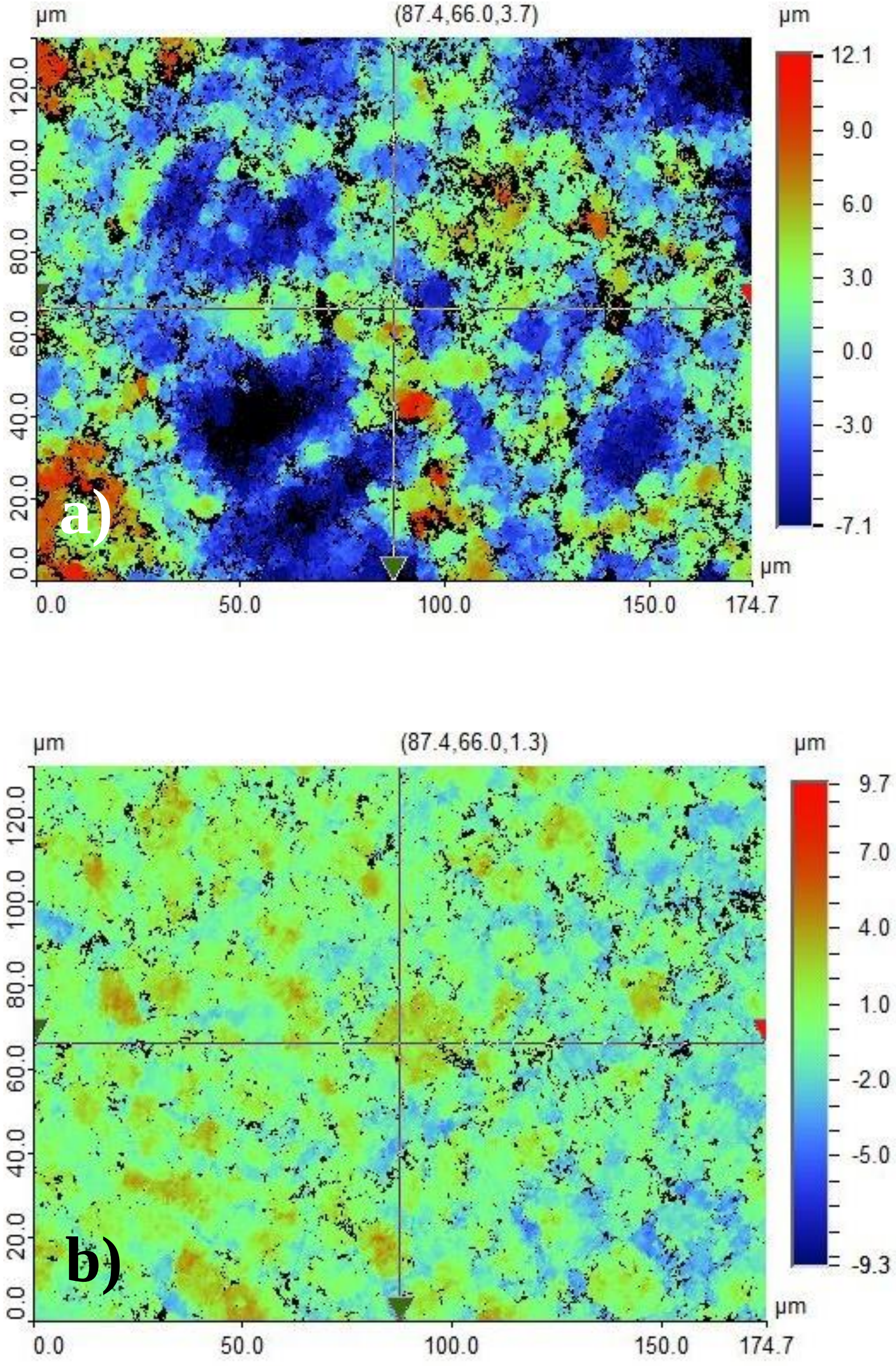

Figure 4.2 Surface 3D profilometry images of a) SLA and b) SLA without sandblasting

The parameters values of surface roughness are presented in Table 4.1.

Roughness (µm)	**Sa**	**Sku**	**Sp**	**Sq**	**Ssk**	**Sv**	**Sz**
SLA 1	2.9	3.1	12.6	3.5	0.5	-7.2	19.8
SLA 2	2.8	2.6	12.3	3.6	0.1	-7.6	20.0
SLA 3	2.9	2.5	13.8	3.5	0.4	-6.7	20.5
SLA	**2.9(0.1)a**	**2.7(0.3)b**	**12.9(0.8)c**	**3.5(0.1)d**	**0.3(0.2)e**	**-7.2(0.5)**	**20.1(0.4)f**
SLActive 1	3.9	2.1	10.4	4.6	0.0	-10.6	20.5
SLActive 2	3.2	2.3	11.9	3.8	0.1	-11.2	23.1
SLActive 3	3.3	2.6	13.1	4.1	-0.3	-11.8	24.9
SLActive	**3.5(0.4)a**	**2.3(0.3)b**	**11.8(1.4)c**	**4.2(0.4)d**	**-0.1(0.2)e**	**-11.2(0.6)**	**22.8(2.2)f**

Table 4.1 Roughness measurements of SLA and SlActive discs (µm). Mean values in bold and standard deviation in brackets. (All t-tests, n=3). Same letters per column indicate means with no statistically significant difference (P>0.05).

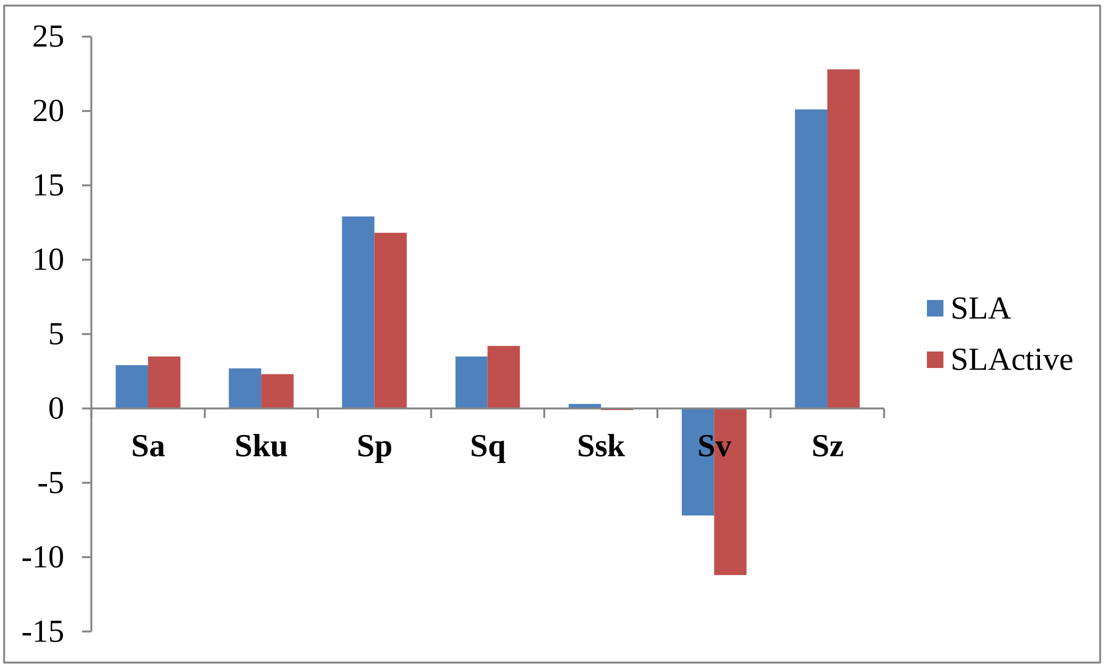

Figure 4.3 Roughness parameters of SLA and SLActive discs (µm). Columns represent mean values.

Table 4.1 shows that the SLActive disks had a rougher surface with an average value of Sa= 3.4 μm, while the SLA disks had a less rough surface with an Sa value of 2.9 μm. Apart from statistically significant difference in the Sv values (P=0.001<0.05), the two surfaces showed no major differences in the rest of the roughness parameters values. The SLActive surfaces demonstrated a slightly higher value (Sa) than SLA, consistently for all the surfaces tested, although not statistically significant (P=0.053 >0.05). This differs from the results published by Wennerberg *et al.* (2012) [121], who found the surface roughness of SLActive and SLA to be the same to two decimals (Sa=2.19 μm). They used though interferometry to calculate Sa values for both implant groups, while the measuring area was 250 x 200 μm^2.

Measurements of non-sandblasted (ns) SLA and SLActive surfaces revealed significant differences in Sa values in samples from the above values, which is expected of course, since the process of sandblasting is designed to create a macrorough surface. More specifically, SLActive (ns) displayed a Sa=1.34 μm and SLA (ns) a Sa=1.28μm.

SLA surface roughness has been studied quite extensively. With regard to 3D roughness evaluation, Sa values for SLA vary in the literature from 1.2 μm (Zhao et al., 2005) [134] to 3.99 μm (Szmukler-Monkler *et al.*, 2004) [135]. Other studies showed values of 1.6 μm (Albrektsson and Wennerberg, 2004) [13], 1.98 μm (Jarmar *et al.*, 2008) [136] and 1.55 μm (Zinelis *et al*, 2012) [137]. There are also a lot of studies which performed a 2D roughness evaluation of the surface and gave Ra values of 2.0 μm (Buser *et al.*, 1999)[138], 2.06 μm (Le Guehennec *et al.*, 2008) [139], 3.22 μm (Rupp *et al.*, 2006) [8] and 3.68 μm (Albrektsson and Wennerberg, 2004) [13]. On the other hand, SLActive surface roughness has not been studied as much. Zhao *et al.* (2005) [134] found a S_a value of 1.2 μm, while Zinelis *et al.* (2012) [137] 1.57 μm. It has to be mentioned though that these values correspond to the roughness of the (usually) small scanned area and are not indicative of the whole rough implant surface. The Sa and Ra values depend on the measuring method and increase as the scanned surface increases [36]. That is why studies of the same implants often report different values for the same implants. In addition, roughness measurements performed on implant buttons differ from those made on real implants, which require filtering to remove waviness.

The surface topography is not easy to measure and different results can be obtained when different measurement and data filtering techniques are being used (Wennerberg *et al*, 1996) [140]. In order to avoid misinterpretation of data derived from various instruments and techniques, Wennerberg et al (1996) [140] published guidelines for the measurement of surface topography.

R_a has been a popularly -and often only- used height parameter to describe implant surface roughness in the literature. It should be taken into consideration that surfaces with very different topographies may indeed have very common Ra values and this parameter on its own can only give limited information on a surface's roughness [141, 142]. Parameters describing surface variation in the spatial direction are necessary to achieve reliable surface characterization [143]. Such parameters are S_{ds} (summit density: number of summits per unit area) and S_{dr} (developed interfacial area ratio: developed versus an ideal reference area ratio). Zinelis *et al.* (2012) [137] studied SLA as received samples and SLActive samples (after ultrasonication with water) and, although no statistical significant differences were found in the amplitude parameters (S_a, S_q, S_z), the spatial (Sdr, Sds) demonstrated significantly higher values in the SLActive category ($p<0.05$).

With the recent nanometer-range characteristics of implant surfaces, where the relevant lateral dimensions may be in the nanometer scale, appropriate tools are necessary for reliable and accurate quantification of the surface roughness [144]. In other words, surface roughness needs to be evaluated in both micro- as well as nanometer scale.

4.2 Contact Angle Goniometry

Tables 4.2 & 4.3 show the results of the contact angle goniometry measurements.

	SLA	SLA (no sandblasting)	SLActive	SLActive (no sandblasting)
1a	96.58	108.57	<5	<5
1b	101.2	115.09	<5	<5
1c	102.71	126.43	<5	<5
1d	103.08	132.25	<5	<5
1e	103.17	133.7	<5	<5
1f	103.29	133.9	<5	<5
2a	107.74	134.59	<5	<5
2b	123.57	134.87	<5	<5
2c	126.06	135.59	<5	<5
2d	129.15	128	<5	<5
2e	111.21	131.41	<5	<5
2f	106.69	132.09	<5	<5
3a	108.97	129.26	<5	<5
3b	119.76	124.43	<5	<5
3c	110.19	107.9	<5	<5
3d	115.38	133.57	<5	<5
3e	124.54	115.43	<5	<5

Table 4.2 Contact Angle measurements (^{o}), as received samples 1, 2 and 3 (raw data).

Contact angle (degree)	SLA	SLA (no sandblasting)	SLActive	SLActive (no sandblasting)	Rutile
Sample 1	101.67	125.00	<5	<5	-
Sample 2	117.40	132.76	<5	<5	-
Sample 3	115.77	122.19	<5	<5	-
Mean	111.61	126.62	<5	<5	77.03
SD	8.65	5.50	-	-	4.43

Table 4.3 Contact Angle measurements (^{o}), as received samples. Mean values for the 3 samples and Standard deviation (SD).

SLA surfaces, both sandblasted and non-sandblasted, displayed varying results, ranging from 96.58 ^{o} to 129.15 ^{o} for the sandblasted and 107.9 ^{o} to 135.59^{o} for the non-sandblasted respectively. The SLA discs had a mean contact angle measurement value of 111.61^{o} indicative of a particularly hydrophobic surface, whereas the non-sand blasted side of the discs had a higher contact angle value of 126.62^{o}. It was found that the non-sandblasted side of the SLA discs had a statistically significantly (t-test, $P<0.01$) higher contact angle (15.01 ± 3.3^{o}), showing that sand-blasting as a surface treatment may have contributed in increasing the wettability of the disc surface.

On the other hand, with regards to the SLActive discs, it was difficult to form a satisfactory profile image of a sessile drop. They exhibited complete wetting forming a layer of water across the surface, with a contact angle approaching zero (less than 5 degrees), thus the SLActive surfaces are defined as having super hydrophilic properties. The same result was found on the non-sandblasted side of the disc. This implies that sandblasting has no effect on the wettability of the SLActive surface.

A single crystal of rutile TiO_2 (100) showed relatively constant results with contact angle values ranging from 72.80^{o} to 83.88^{o} and a mean value of 77.03^{o}.

De Wild (2005) [145] investigated the hydrophilicity of SLActive dental implants compared to standard SLA by Dynamic Contact Angle analysis (DCA). The initial contact angle of SLA completely differs from SLActive. Repeated force loops of Wilhelmy-electrobalance measurements on SLA implant show hysteresis (Δm), which in turn indicates contact angle hysteresis: The first advancing mean water contact angles were $\theta^{1st}_{adv}>90°$ for SLA, but 0° for SLActive. Thus, the SLActive samples show maximum hydrophilicity in contrast to hydrophobic SLA.

The surface energy and hydrophilicity of SLA was found by Schwarz *et al.* (2007) [146] to be very low compared to SLActive. In addition, Rupp *et al*. (2006) [8] measured an average contact angle of 139.9^{o} for SLA and 0^{o} for SLActive, i.e. complete wetting of the surface by water.

Taking into consideration that both SLA and SLActive are similarly microstructured (see section 4.2), the difference in surface wettability may be attributed to the change of surface composition. While the SLActive surface remains stable due to its insertion in isotonic NaCl solution, the SLA surface is contaminated by atmospheric hydrocarbons which reduce its surface energy. Notably, the contact angle of a titanium disc can very easily change from hydrophilic to hydrophobic, since it only takes a few seconds before the exposed surface is contaminated by a monolayer of hydrocarbons and other inorganic impurities. Storing titanium discs in solution can therefore protect from hydrocarbons contamination and, thus, enhance surface energy.

In general, the hydrophilicity, which enhances the initial adsorption of plasma proteins can indeed be increased by a post etch chemical modification and storage in an aqueous solution (Schwarz *et al.*, 2007) [147], by heat treatment of the native surface increasing the thickness as well as crystallinity of the surface oxide (Feng *et al.,* 2002) [148] or by photocatalytic phenomena upon irradiation by UV light (Sawase *et al.*, 2008) [149].

The contact angle measurements above demonstrate considerable differences between the samples. Surface roughness affects these measurements and from surface profilometry measurements we know that SLA and SLActive have similar surface roughness values. The latter are, of course, considerably rougher that their non-sandblasted equivalents.

SLA surface has a smaller contact angle compared to its non-sandblasted (smoother) equivalent, thus it is more hydrophilic. As stated above, contact angle can be shifted due to surface topography changes. It can be inferred thus, that sandblasting has decreased SLA’s hydrophobic behaviour. On the other hand, both sandblasted and non-sandblasted SLActive surfaces displayed complete wetting of their surfaces, hence they are both super hydrophilic. Because of this, it is not possible by means of sessile drop method to see any effect that surface roughness may have on the hydrophilic behaviour of these surfaces.

Lastly, a rutile single crystal (which is expected to be covered in adventitious hydrocarbons) displayed a contact angle of 77.03^{o}, which is smaller than SLA and far greater than SLActive. This could suggest that surface structure does affect wetting behaviour as well, since the above three surfaces appear to have different surface crystal structures. It should be noted also that the single crystal will have been covered in adventitious hydrocarbon.

4.3 Raman Spectroscopy

The crystallinity of the specimen's surface will affect its Raman spectrum. In most cases Raman scattering is sensitive to the degree of crystallinity in a sample. Typically a crystalline material yields a spectrum with very sharp, intense Raman peaks, whilst an amorphous material will show broader less intense Raman peaks. These two states (e.g. fully amorphous or fully crystalline) can be considered as spectral extremes, and a Raman spectrum from an intermediate state (e.g. partially crystalline) will have characteristics that are intermediate in terms of peak intensity and width (sharpness).

Raman spectra for SLA, SLActive and TiO_2 (100) rutile single crystal are displayed at Figures 4.4 - 4.6, 4.7 - 4.9 and Figure 4.10 respectively.

Both SLA and SLActive samples were tested as received, after washing in de-ionised water and after washing in acetone, ethanol and de-ionised water. No peak position differences were detected due to these cleaning processes.

SLA spectra are displayed below in Figures 4.4 – 4.6.

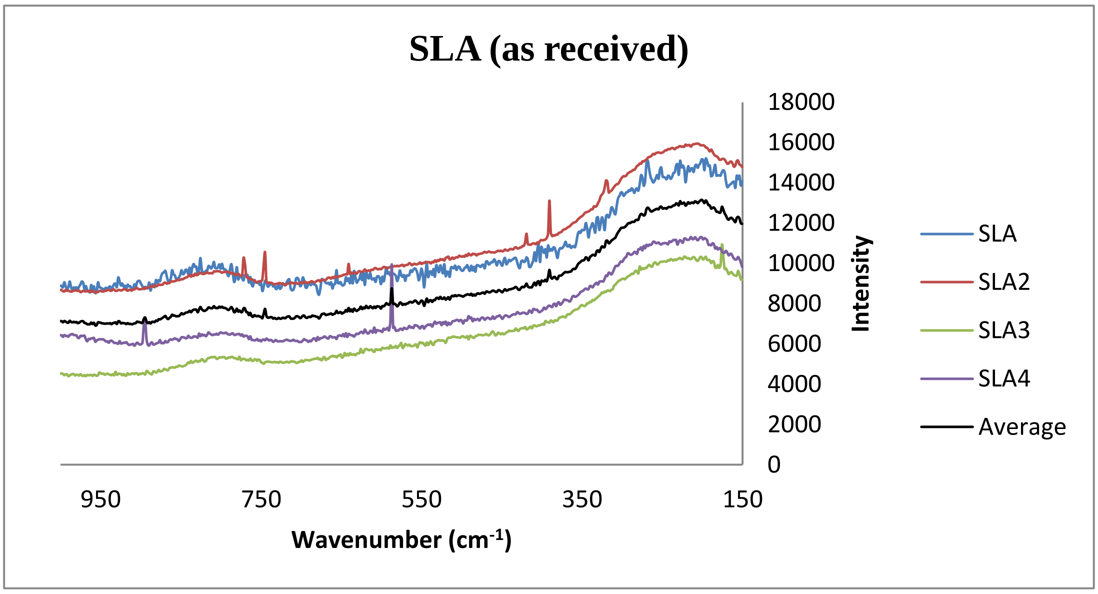

Figure 4.4 Raman Spectra of SLA discs, as received. SLA, SLA2, SLA3 and SLA4 represent measurements on different positions on the same sample.

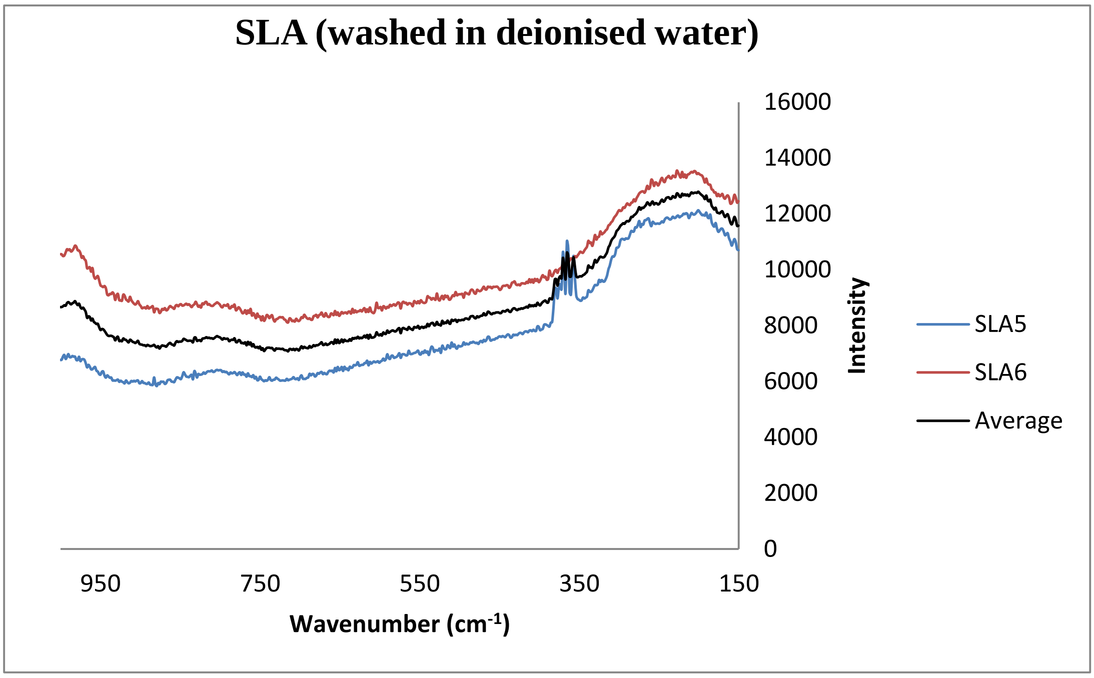

Figure 4.5 Raman Spectra of SLA discs, after being washed in distilled water. SLA5 and SLA6 represent measurements on different positions on the same sample.

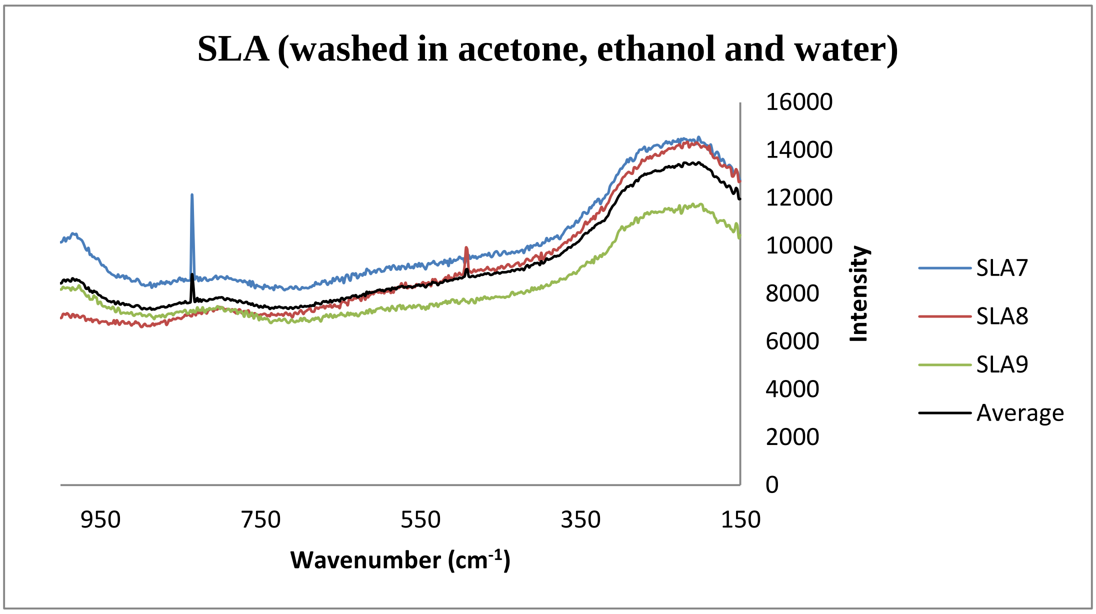

Figure 4.6 Raman Spectra of SLA discs, after being washed in acetone, ethanol and distilled water respectively. SLA5 and SLA6 represent measurements on different positions on the same sample.

SLA spectra demonstrated no well-defined peaks, indicative of non-crystalline structure (amorphous titania). Just broad falls and rises in the intensity were detected, whereas the spectra from both the sandblasted and non-sandblasted surfaces appeared identical.

SLActive spectra are displayed below in Figures 4.7 – 4.9.

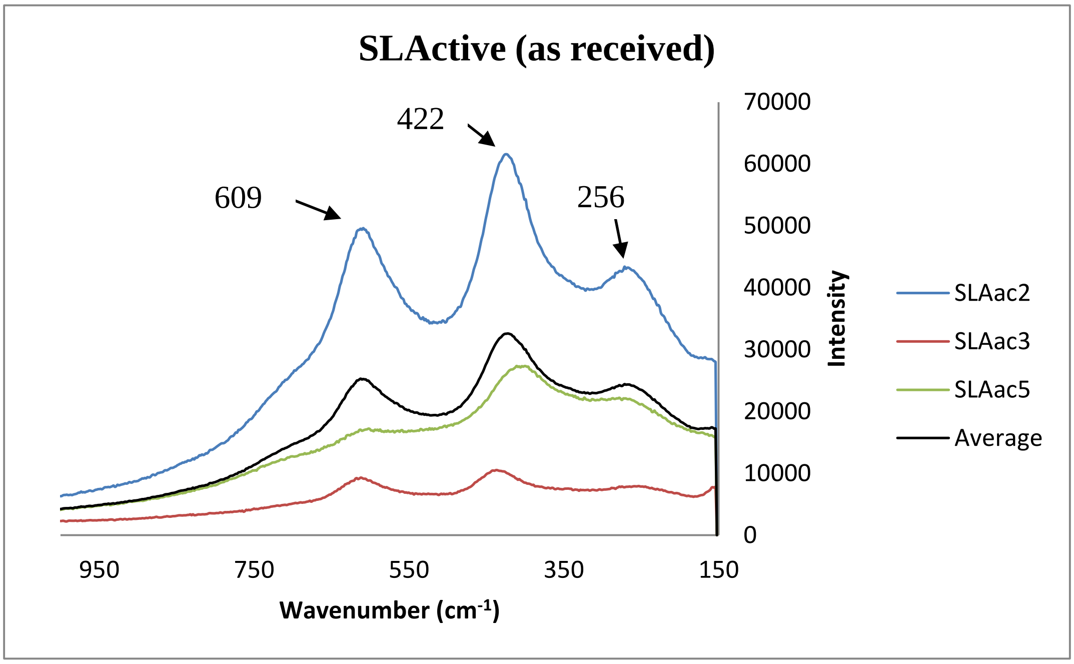

Figure 4.7 Raman Spectra of SLActive discs, as received. SLAac2, SLAac3 and SLAac5 represent measurements on different positions on the same sample.

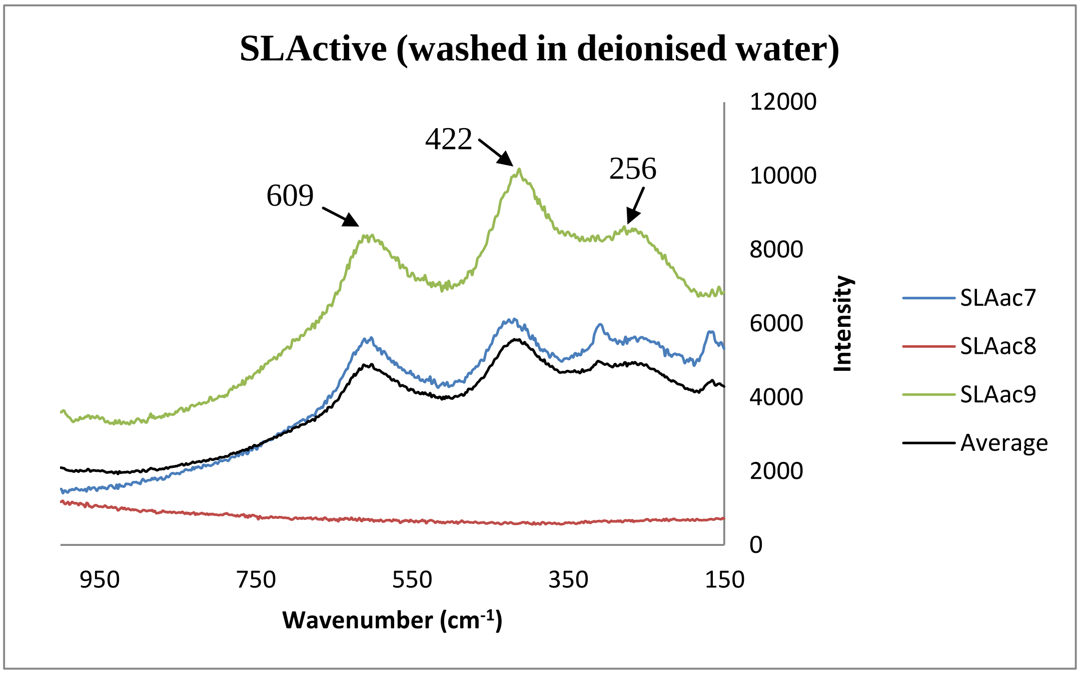

Figure 4.8 Raman Spectra of SLActive discs after being washed with distilled water (two distinct spectra visible). SLA5 and SLA6 represent measurements on different positions on the same sample.

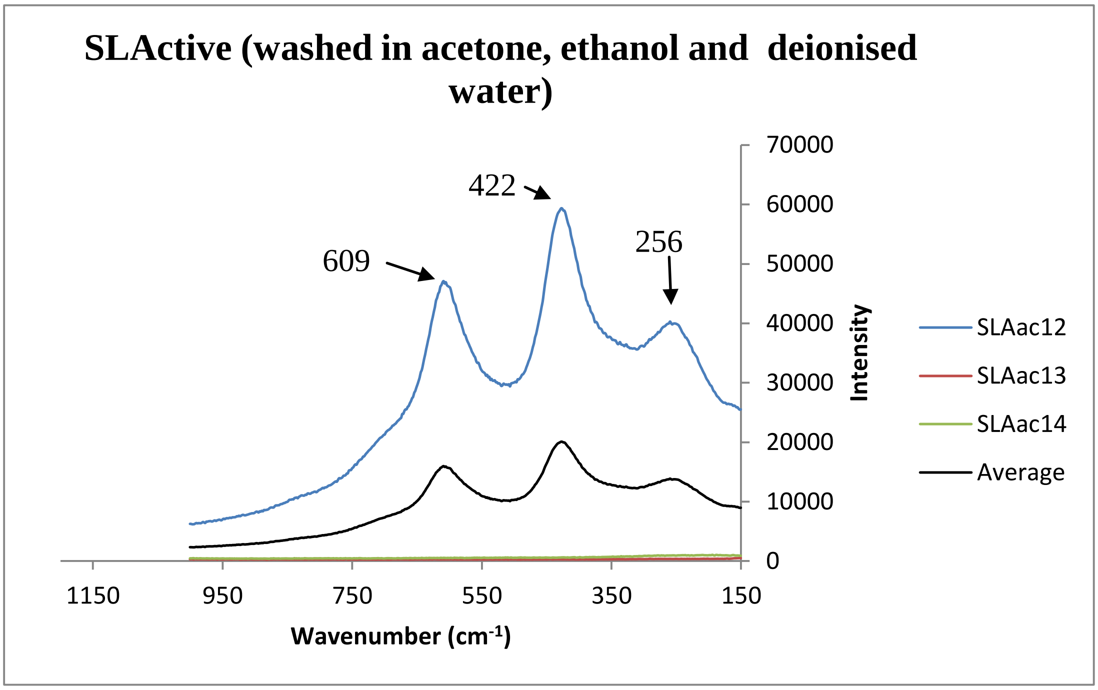

Figure 4.9 Raman Spectra of SLA discs, after being washed in acetone, ethanol and distilled water respectively. SLAac12, SLAac13 and SLAac14 represent measurements on different positions on the same sample.

The Raman spectra from different points on the SLActive surface following different washing methods shown in Figures 4.7 – 4.9 gave rise to two distinct spectra. The majority of the spectra showed strong peaks at 609, 422 and 256 cm^{-1} nm, although the intensity of these features varied at different points on the surface. Some areas, however, gave rise only to broad featureless spectra similar to those observed on the SLA surface (see e.g. Fig. 4.8, SLAac8 spectrum and Fig. 4.9 SLAac14 spectrum). These two spectra were also measured on the non-sandblasted side of the samples.

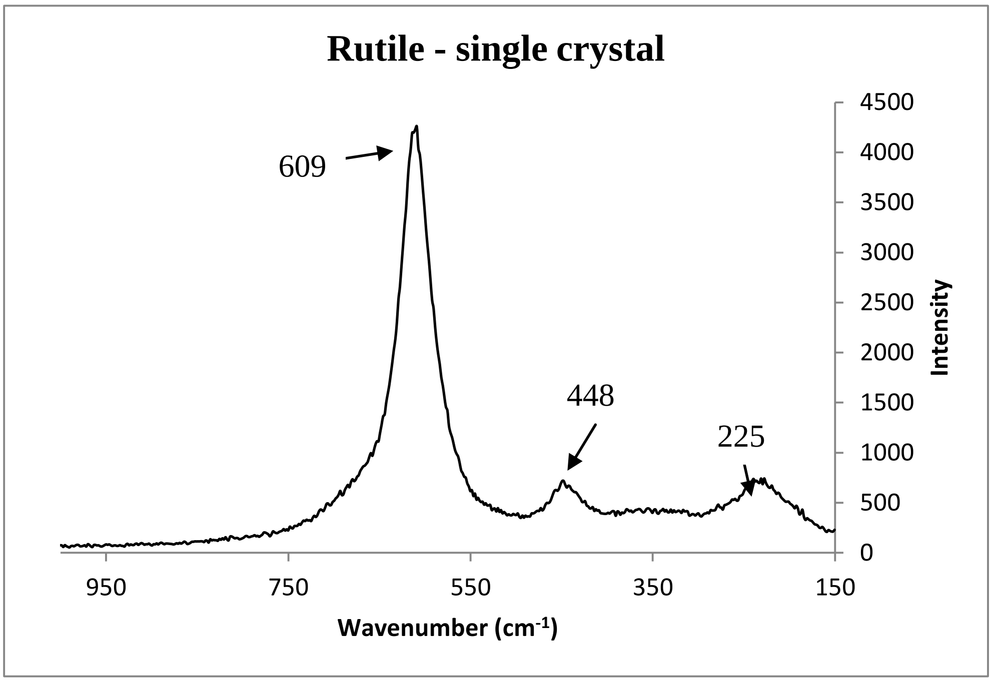

Figure 4.10 Raman Spectra of Rutile (TiO_2) single crystal.

A TiO_2 (100) rutile single crystal (Fig.4.10) displayed narrow peaks at 609, 448 and 225 cm^{-1}. The above spectrum had to be measured at 1% laser power due to the intensity of the 609 cm^{-1} peak which saturated the CCD detector.

Initial results from Raman spectroscopy of SLA and SLActive discs (Fig. 4.4 – 4.9) show two clear types of material. The SLA displayed a generally amorphous structure, whilst SLActive displayed both a similar structure to SLA and a more crystalline appearing structure, which resembles that of rutile $TiO_{2.}$ As mentioned previously, amorphous materials generally give weaker relative intensities and broader peaks than crystalline materials. Hence on the more amorphous SLA material longer scan times were required to obtain similar signal to noise ratios.

It was observed that the spectra of the SLActive materials were strongly dependant on the focus of the laser. This suggests that there was some change in structure relatively close to the surface of the material. This sensitivity was not that intense in the SLA sample discs, which may imply the existence of a relatively thicker layer on the SLA surface. An observation also made was that a Raman spectrum taken on a surface scratch on an SLA sample displayed the more crystalline appearing peaks observed on SLActive samples (Fig 4.11 and 4.12), corroborating the above suggestion. Since the depth of analysis in Raman is much greater than XPS, a possible explanation is the presence of well-organized, thick organic contamination zone (possibly residues from the manufacturing process).

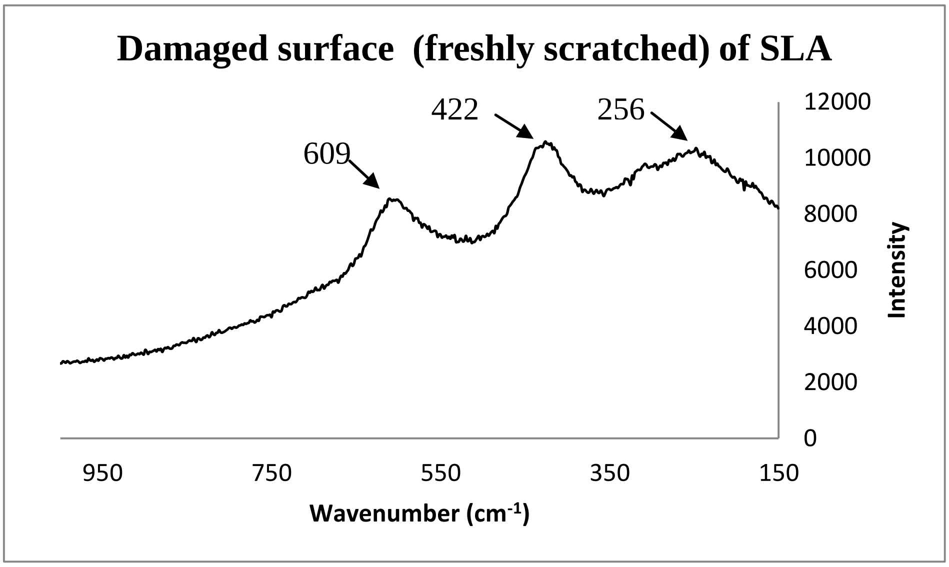

Figure 4.11 Raman Spectra of scratched area of an SLA disc.

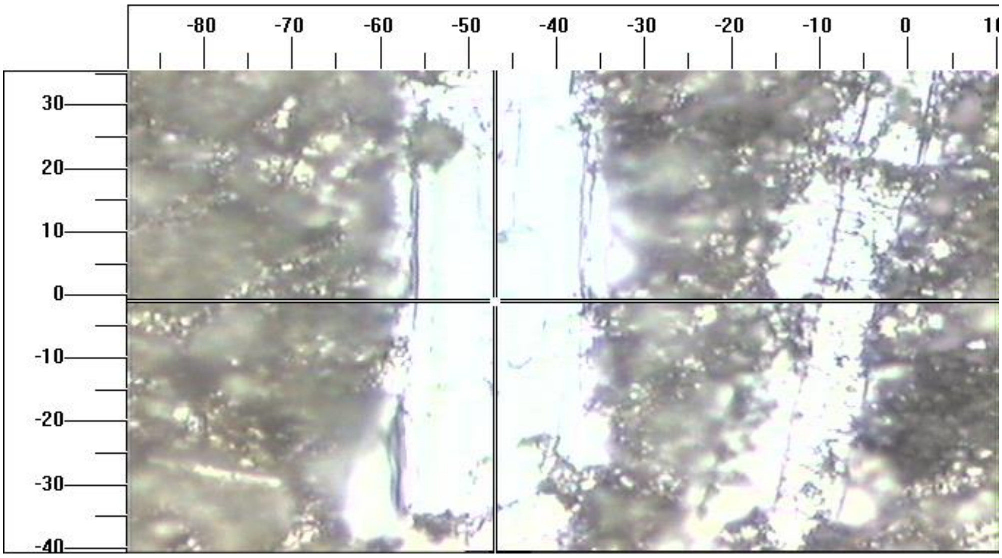

Figure 4.12 Image of scratched area of an SLA disc (magnification x 50).

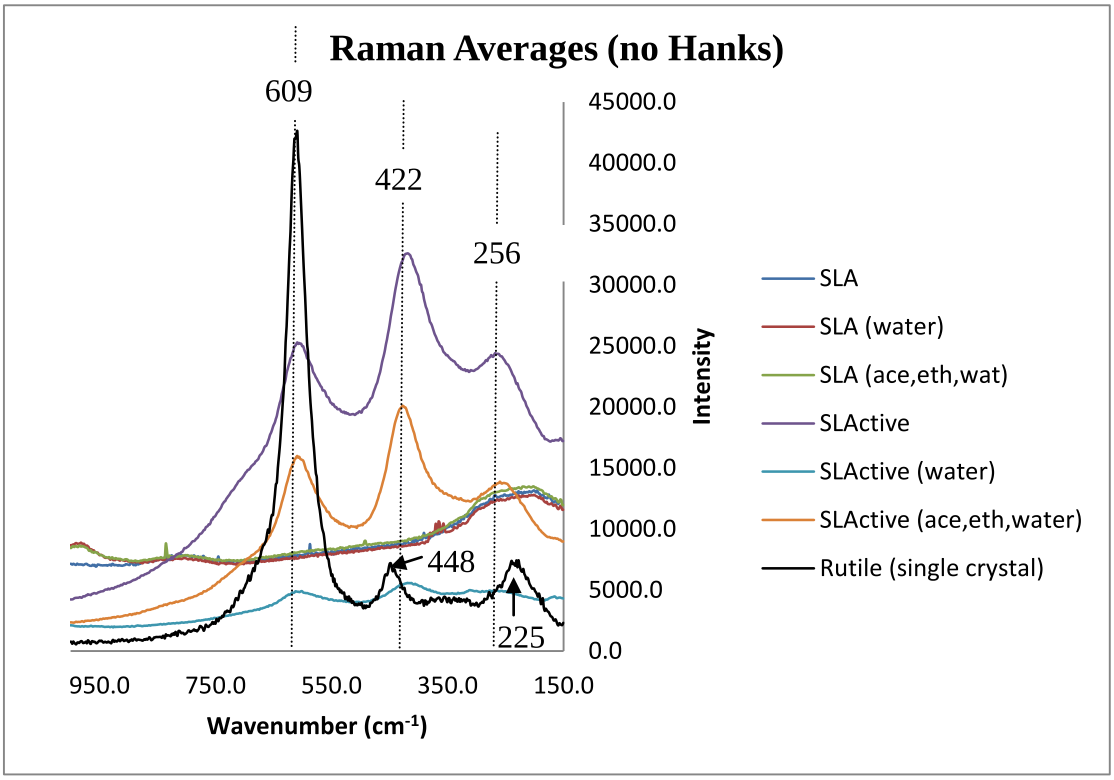

Figure 4.13 Summary of Raman peaks: averaged and intensities adjusted for clarity.

A summary of all average spectra of the SLA and SLActive discs is displayed in Fig 4.13. In both samples and the two types of peaks there is an approximate set of peaks that are consistent with both being the same material, the minor wavenumber shifts is also most likely to occur due to the differences in crystallinity of the samples' surfaces.

The common feature in the SLActive spectra is the presence of broad Raman shifted lines at 609 cm^{-1} and 422 cm^{-1}, which have been assigned to nano-rutile phase TiO_2 [6]. There is also a third broad peak present in the graphs at 256 cm^{-1}. This peak at around 250 cm^{-1} is considered a multiphonon peak. Parker and Siegel (1990) [6] studied nanophase TiO_2 and the peak positions for nanorutile, nanoanatase as well as their single crystal counterparts are displayed at Table 4.4 below. The peak at 609 cm^{-1} is seen at both rutile single crystal (SC) and SLActive samples. Rutile SC has a second peak at 448 cm^{-1}, whereas SLActive samples have it at 422 cm^{-1}, which indicates that nano-phase TiO_2 material found on SLActive discs is based on the rutile structure.

On the other hand, anatase is generally identified by the presence of its strongest peak at 144 cm$^{-1,}$ as well as smaller lines near 640, 515 and 205 cm^{-1}. Anatase nano-TiO_2 displays a further shifted peak at 154 cm^{-1}. Such peaks are not observed at this experiment. We cannot rule out though a peak at 144 cm^{-1} or 154 cm^{-1}, since the spectrometer filter cuts out wavenumber shifts of less than 150 cm^{-1} to limit noise, while any peaks just above the 150 cm^{-1} threshold may be lost if they are weak, since the background noise at these wavenumber shifts is higher than at larger shifts. Sul *et al.* (2002) [150] suggested that the degree of crystallinity and the commonly thin nature of the titanium oxide can make it difficult to obtain signal intensities above the noise level with Raman spectroscopy.

Nanophase TiO_2	Single crystal rutile TiO_2	Epitaxial film anatase TiO_2
154±1	…	154±1
424±4	447±3	…
612±4	612±3	…

Nanophase TiO_2 154±1 cm^{-1} line FWHM = 25.5 cm^{-1}
Epitaxial TiO_2 film 144 cm^{-1} line FWHM = 11 cm^{-1}

Table 4.4 TiO_2 Raman peak positions (cm^{-1}) [6]

The tests suggest that SLA surface is comprised mainly of amorphous titania (or hydrocarbons) [151], while SLActive consists of areas of amorphous titania (or hydrocarbons) as well as regions of crystallinity, suggestive of nano-rutile crystals, but no large crystals. It was observed that the SLActive spectra were strongly dependant on the focus of the laser. This implies that there must be some change in structure relatively close to the surface of the tested material. Some spectra suggested a completely amorphous material, whereas others displayed the SLActive type peaks (nano-rutile). Occasionally, the same sample area could display both kinds of spectra if it was refocused and, than, retested. A possible explanation for this, is that an amorphous layer exists above a crystalline surface. A logical formation process for this would be if a crystalline surface was created by the initial processing, as seen on Raman spectra of SLActive samples. Subsequent storage in plastic containers -SLA samples- would allow faster hydrocarbon contamination which justifies the amorphous carbon formation on the sample surfaces.

SLA and SLActive surfaces have rarely been studied using Raman spectroscopy. In addition, it is the second time that crystalline phases of these surfaces have been considered, the prior published work being a study by Zinelis *et al.* (2012) [137] who used RFTIRM.

The effect of immersion in Hanks' solution

The spectra below (Fig. 4.14 - 4.17) show the Raman spectra of SLA and SLActive after incubation / immersion in Hanks' solution

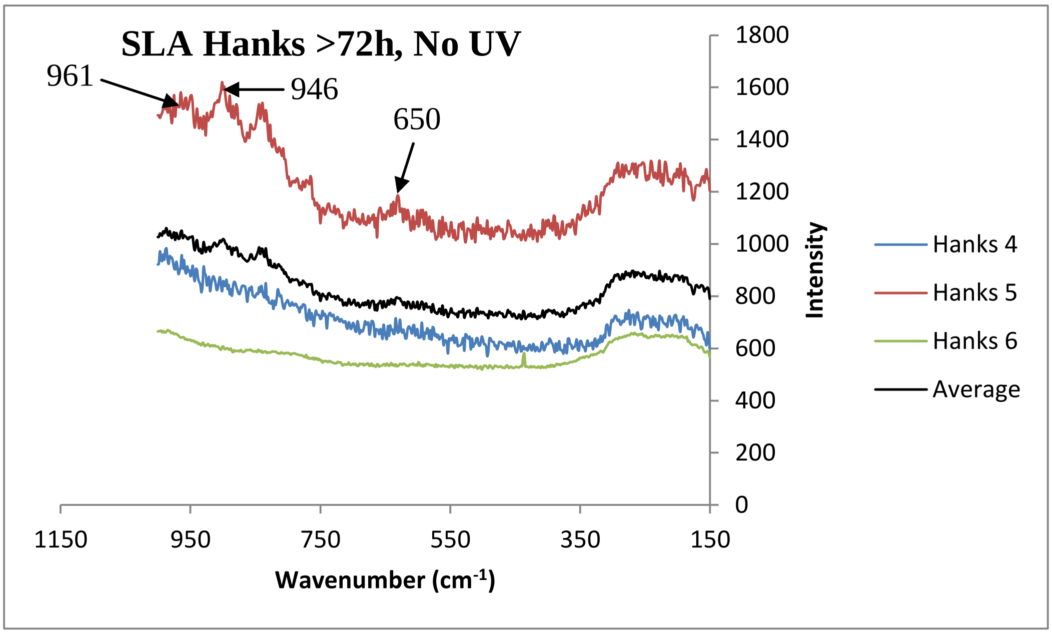

Figure 4.14 Raman spectra of SLA disc in Hanks for 2 months without UV treatment. Hanks 4, Hanks 5 and Hanks 6 represent measurements on different positions on the same sample.

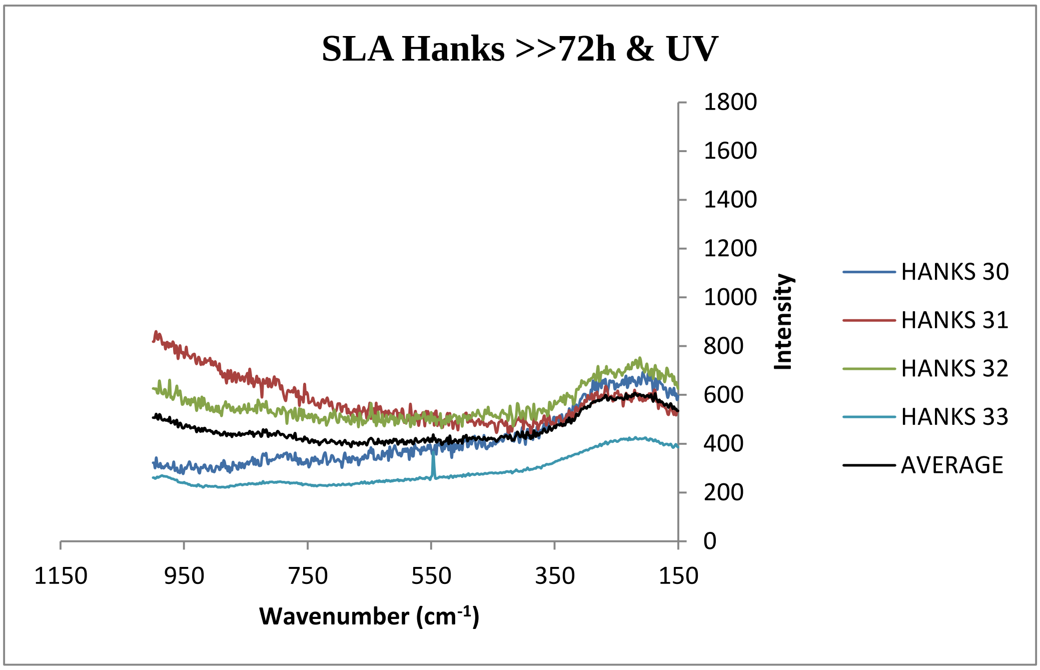

Figure 4.15 Raman spectra of SLA discs in Hanks for 2 months with UV treatment. Hanks 30, Hanks 31, Hanks 32 and Hanks 33 represent measurements on different positions on the same sample.

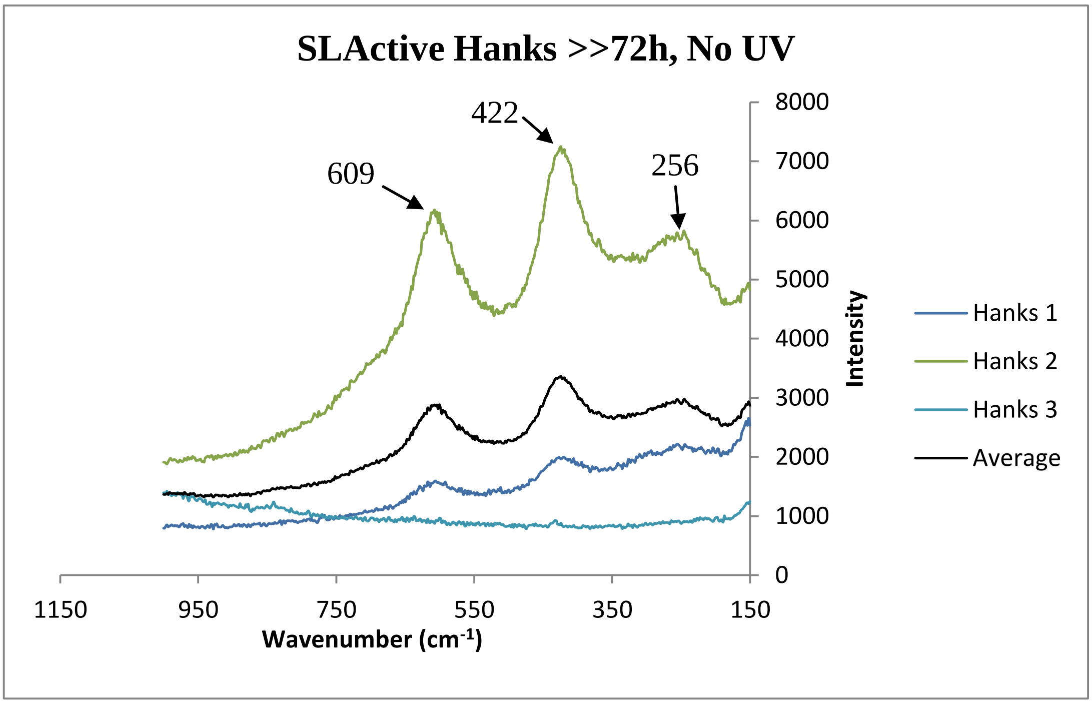

Figure 4.16 Raman spectra of SLActive discs in Hanks for 2 months without UV treatment. Hanks 1, Hanks 2 and Hanks 3 represent measurements on different positions on the same sample.

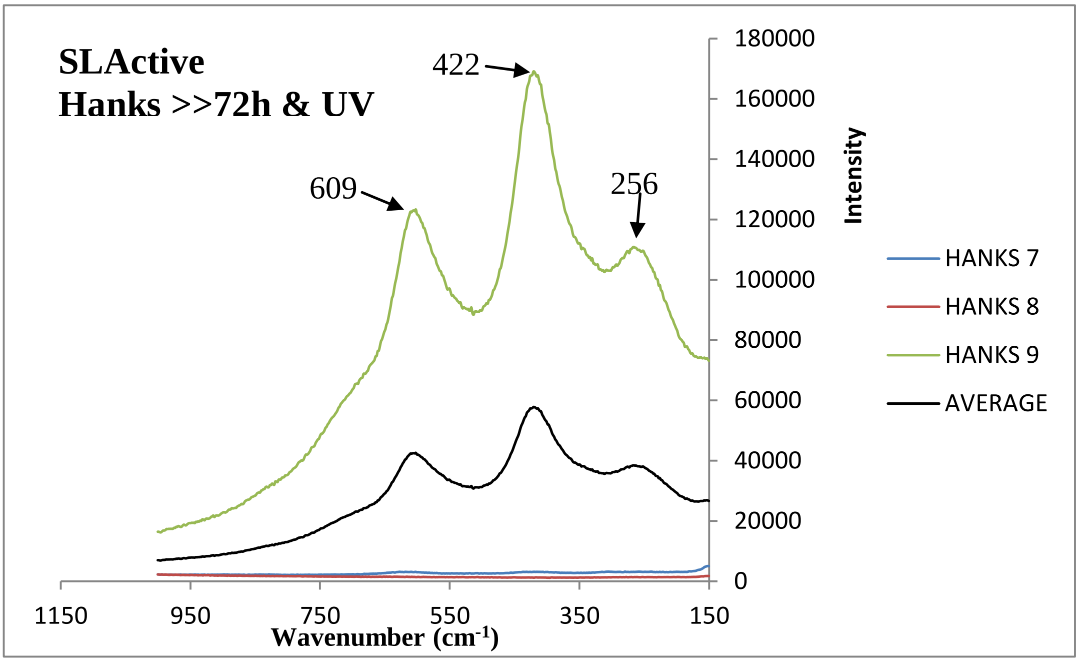

Figure 4.17 Raman spectra of SLActive discs in Hanks for 2 months with UV treatment. Hanks 7, Hanks 8 and Hanks 9 represent measurements on different positions on the same sample.

With intensities adjustment for clarity and ease of comparison (Spectra divided by 10 for SLAactive Hanks 72h/UV) the final diagram for the average spectra of samples in Hanks for over 72h is as follows (Fig. 4.18):

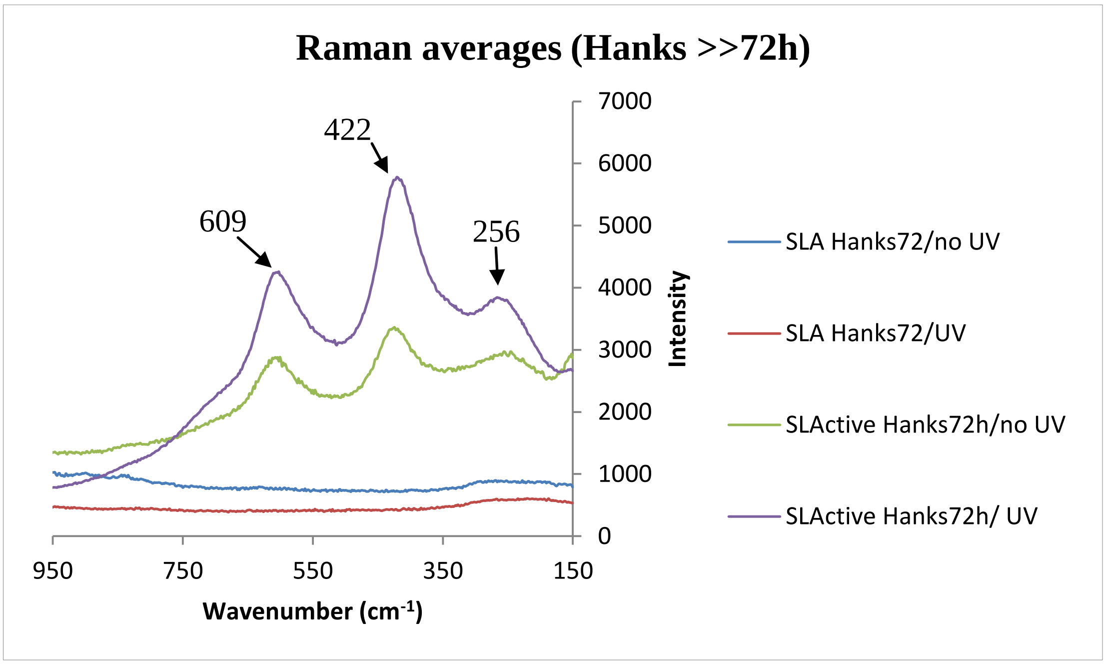

Figure 4.18 Raman spectra from SLA and SLActive disks with and without UV treatment after 72h incubation at 38°C and 2 months in Hanks solution at room temperature.

As seen on Raman spectra above, incubation of sample discs at Hanks Solution for more than 72 hours did not result in any distinct changes in crystallinity of the surfaces. However, on the non-UV treated SLA surface (Fig 4.14) there is some evidence of Calcium phosphate growth. The peaks at around 800-950 cm^{-1} and 650 cm^{-1} have been observed in various calcium phosphate and dentin Raman spectra and they are associated with PO_4^{2-} vibrational modes [152, 153]. Similar features are not observed in the non-UV treated SLActive Raman spectra (Fig. 4.16). This may be because the peaks are relatively weak compared to the TiO_2 peaks in the SLA sample.

The UV treatment of samples indicated that SLActive samples that were not UV treated displayed weaker peaks than the UV treated ones. This could be due to the removal of hydrocarbon from the UV treated SLActive samples due to the photocatalytic activity of TiO_2 [116].

4.4 X-Ray Photoelectron Spectroscopy (XPS)

4.4.1 Qualitative Spectral Analysis

The XPS survey spectra recorded from as received samples at a pass energy of 80 eV are displayed below (Fig. 4.19):

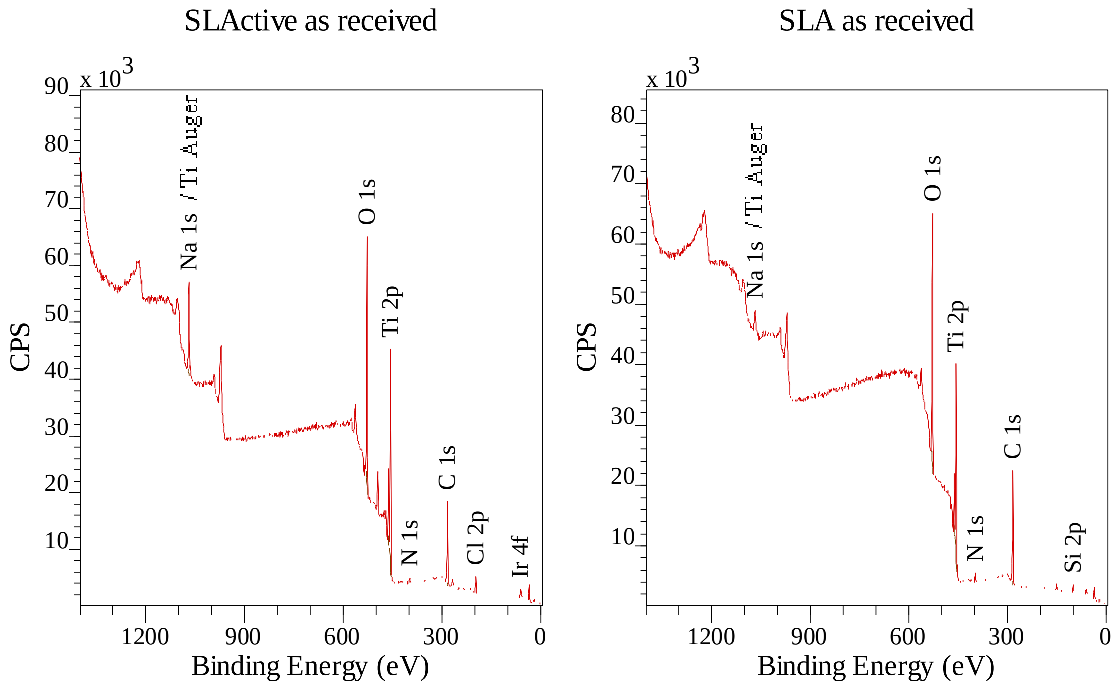

Figure 4.19 XPS wide spectra of SLActive and SLA samples as received.

On all samples Ti, O, C and N signals were always detected by XPS. Ca was also detected on all samples, as well as traces of Cl, P, Na, Cu, Zn, Si. The dominance of the Ti and O signals shows that the surface consists mainly of a titanium oxide layer. The relatively strong C signal can be assigned mainly to surface contamination by absorbed carbon-containing (organic) molecules, which is a normal observation for air-exposed surfaces. The C signal is not as intense on SLActive spectrum, due to the fact it is transferred from the etching solution to aqueous storage under nitrogen and, hence, less exposure to surface contaminants takes place.

Figures 4.20 - 4.22 show survey spectra of the SLA and SLActive samples following UV treatments and incubation in Hanks' solution for 24 and 72 hours.

Following UV treatment of the SLA and SLActive samples (Fig. 4.20) there is very little change in the spectrum apart from the appearance of a small amount of F species in the SLActive sample. It is likely that this is due to contamination from the UV/ozone cleaning environment.

Following immersion in Hanks' solution for 24 hours (Fig. 4.21) the Cl 2p disappears from the SLActive surfaces. There is no other observable change in any of the samples with or without UV treatment.

After 72 hours in Hanks' solution (Fig. 4.22) we see clear evidence of Ca and P at the surface suggesting the growth of 'CaP' on the surfaces apart from the UV treated SLA sample.

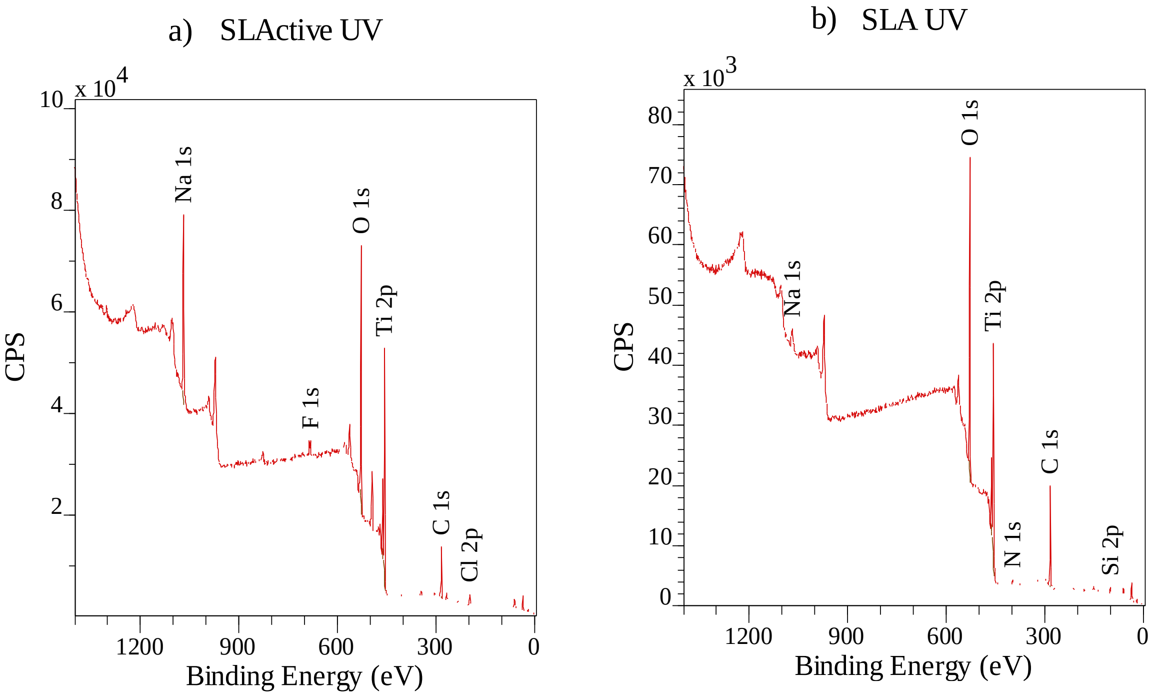
a) SLActive UV

b) SLA UV

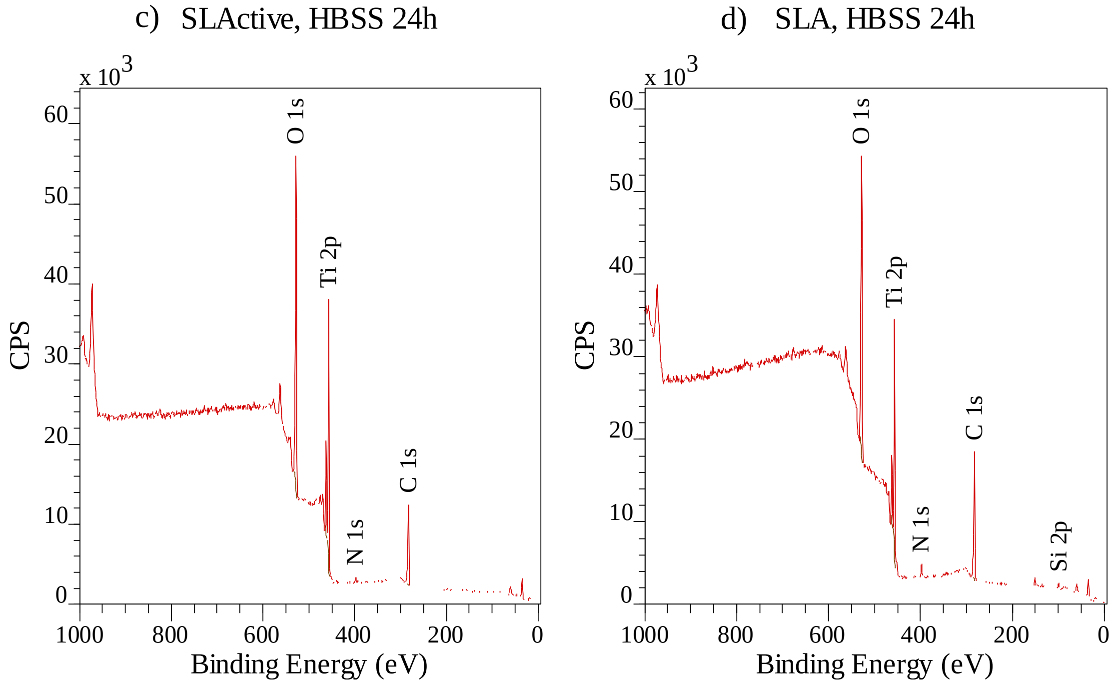
c) SLActive, HBSS 24h

d) SLA, HBSS 24h

Figure 4.20 XPS wide spectra of SLActive and SLA samples after UV treatment (a, b) or after insertion in HBSS for 24h (c, d).

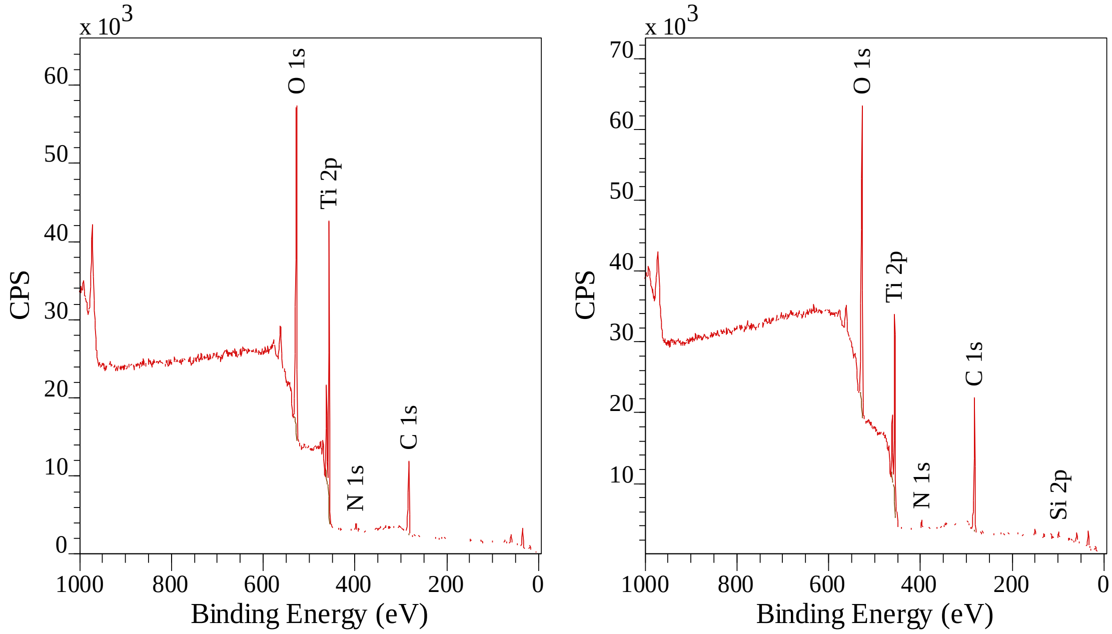

a) SLActive UV, HBSS 24h

b) SLA UV, HBSS 24h

c) SLA UV, HBSS 24h, graz.em.

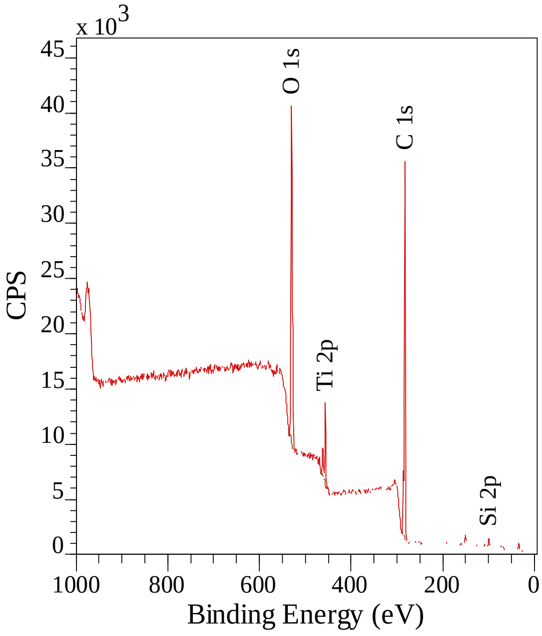

Figure 4.21 XPS wide spectra of SLActive (a) and SLA (b) samples after UV treatment and consecutive insertion in HBSS for 24h. XPS wide spectra (45° grazing emission) of SLA (c) samples after UV treatment and consecutive insertion in HBSS for 24h.

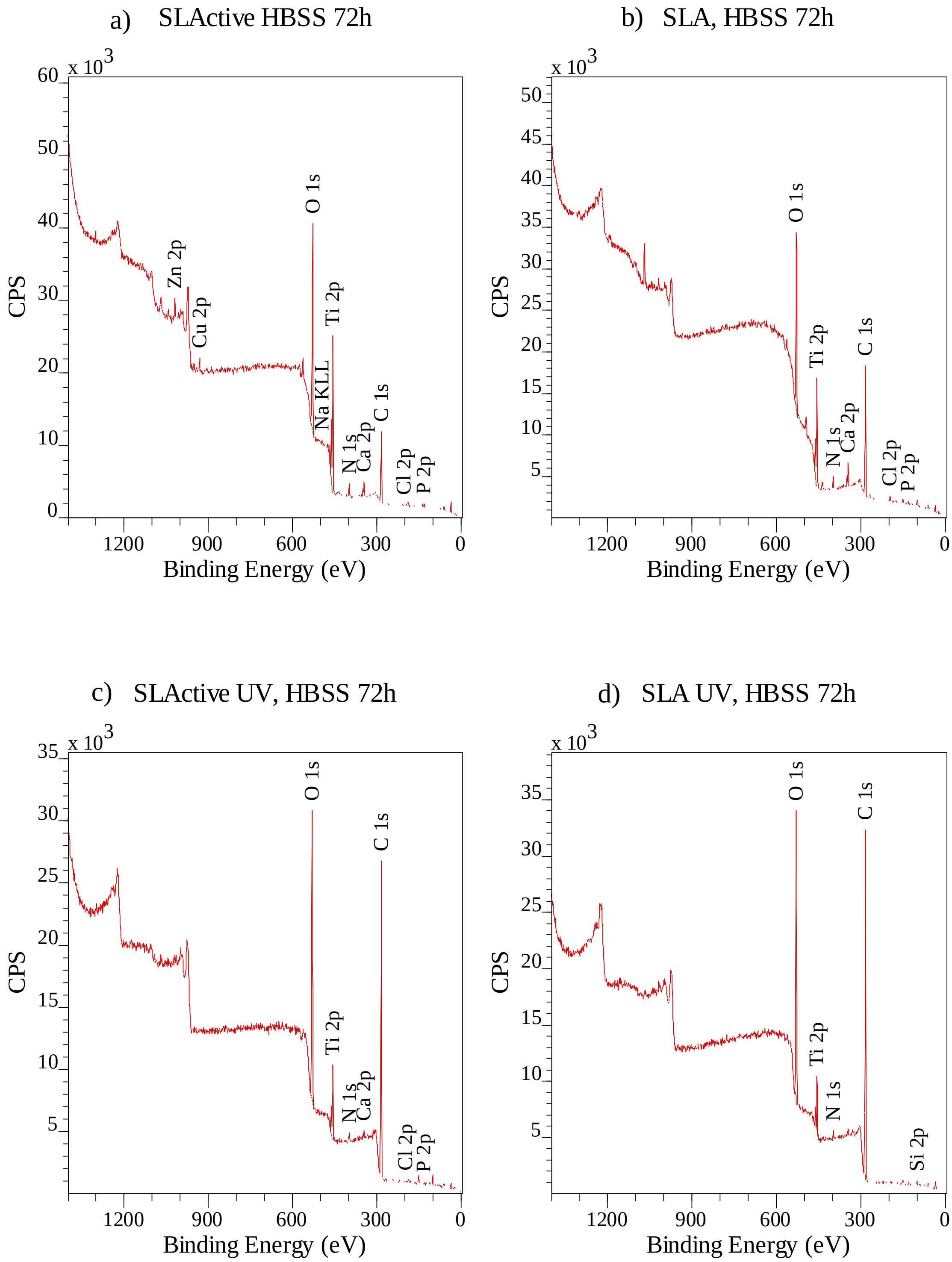

Figure 4.22 XPS wide spectra of SLActive and SLA samples after insertion in HBSS for 72h (a, b) and after UV treatment and consecutive insertion in HBSS for 72h (c, d).

High resolution Ti 2p spectra recorded at a pass energy of 20ev are displayed below:

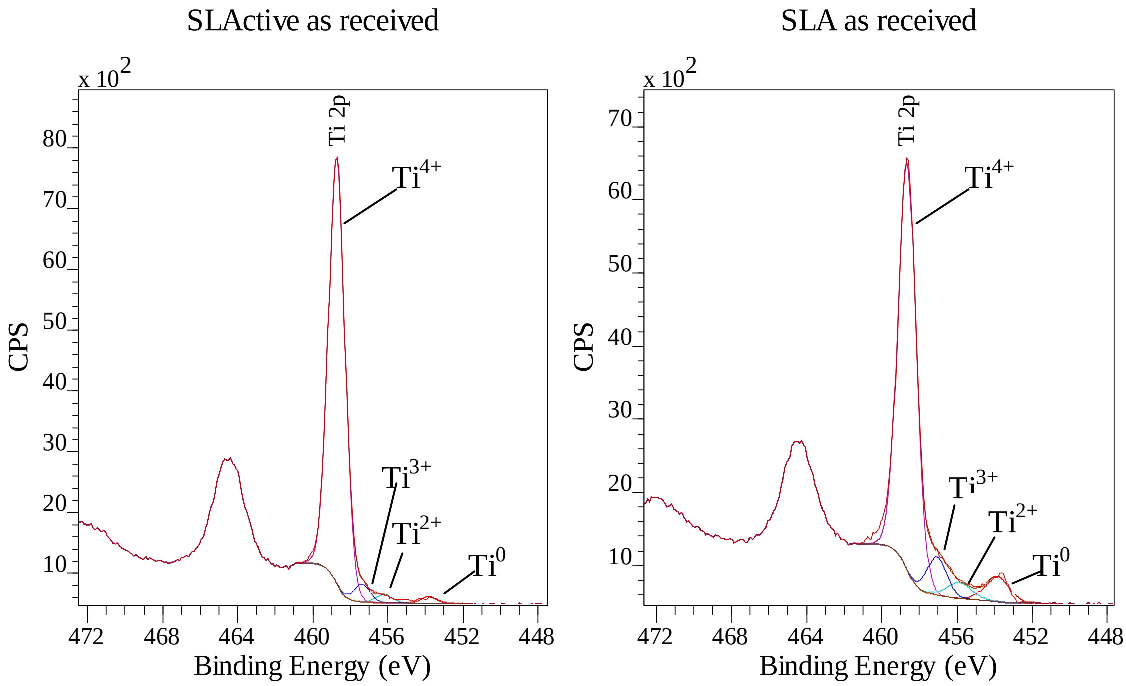
SLActive as received

SLA as received

Figure 4.23 XPS Ti 2p spectra of SLActive and SLA samples as received.

Fig. 4.23 displays typical spectra of the Ti 2p region from the surface of the as received samples. The Ti 2p is a doublet peak consisting of spin orbit split Ti $2p_{1/2}$ and Ti $2p_{3/2}$ peaks. We will only consider the Ti $2p_{3/2}$ distribution for the analysis. This peak is dominated by a peak at a band energy of 459 eV, but a small peak at 454 eV is also detected. The main peak is assigned to Ti^{4+} (TiO_2), while we assign the small one to metallic Ti [154]. The presence of a “metallic” peak in the spectra is attributed to the fact that the surface oxide is thin enough to allow photoelectrons from the metal just beneath the metal-oxide interface to escape through the oxide. This effect has been used to estimate the thickness of the surface oxide [155]. In addition, there are small intensity contributions in the region between the Ti^{4+} and the Ti metal peaks in the high-resolution Ti 2p spectra. Their existence is attributed most likely to the presence of sub-oxides (TiO and Ti_2O_3) at the metal-oxide interface [8, 134]. Such signals coming from lower oxidation states of Ti may be also due to defects in the TiO_2 surface oxide, e.g. interstitial Ti atoms and/or O vacancies. The existence of small amounts of carbide (TiC_x) or nitride (TiN_x) in the surface oxide could also explain the presence of this peak [155].

a) SLActive UV

b) SLA UV

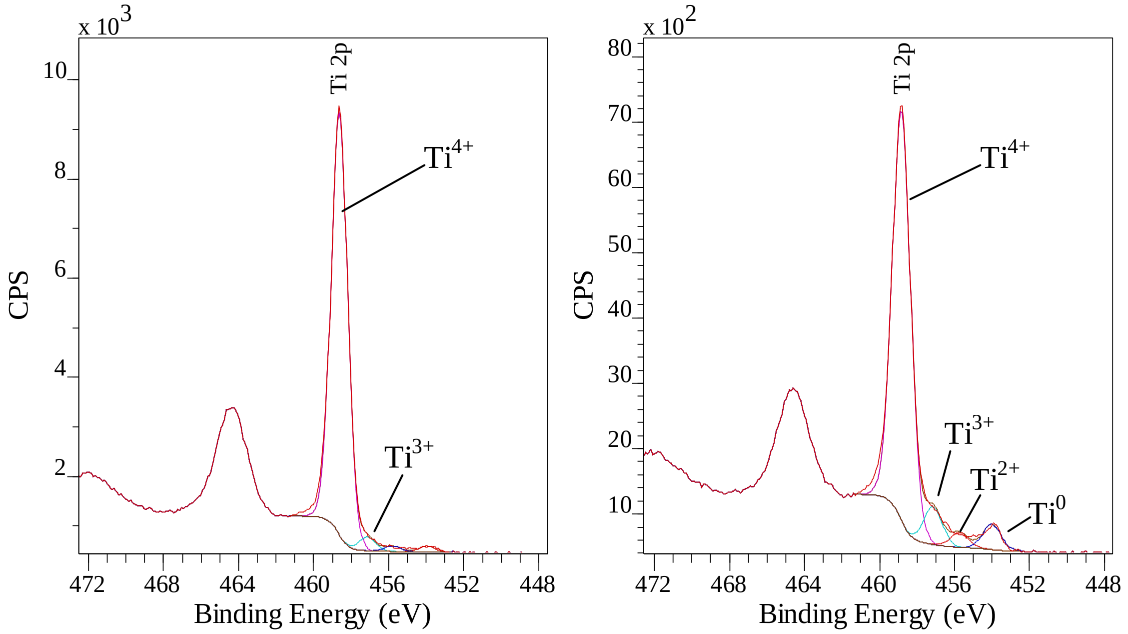

c) SLActive HBSS 24h

d) SLA HBSS 24h

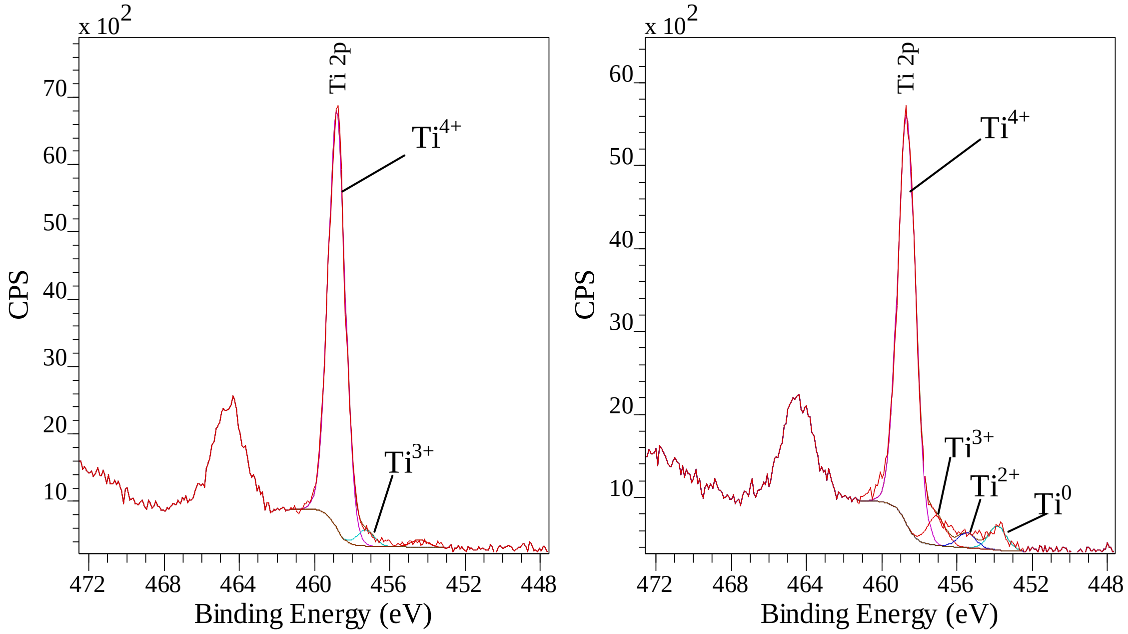

Figure 4.24 XPS Ti 2p spectra of SLActive and SLA samples after UV treatment (a, b) or after insertion in HBSS for 24h (c, d).

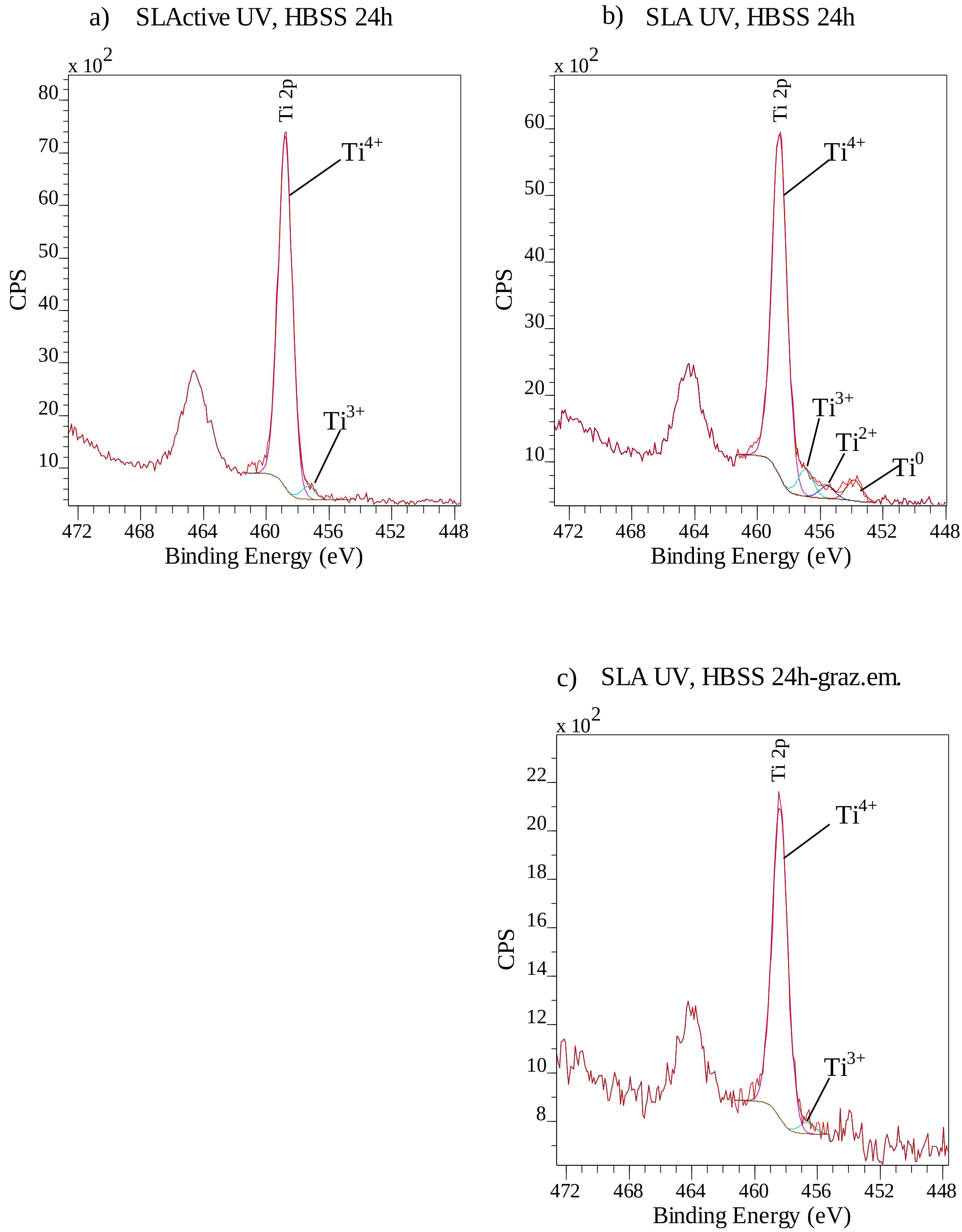
a) SLActive UV, HBSS 24h

b) SLA UV, HBSS 24h

c) SLA UV, HBSS 24h-graz.em.

Figure 4.25 XPS Ti 2p spectra of SLActive (a) and SLA (b) samples after UV treatment and consecutive insertion in HBSS for 24h. XPS wide spectra (45° grazing emission) of SLA (c) samples after UV treatment and consecutive insertion in HBSS for 24h.

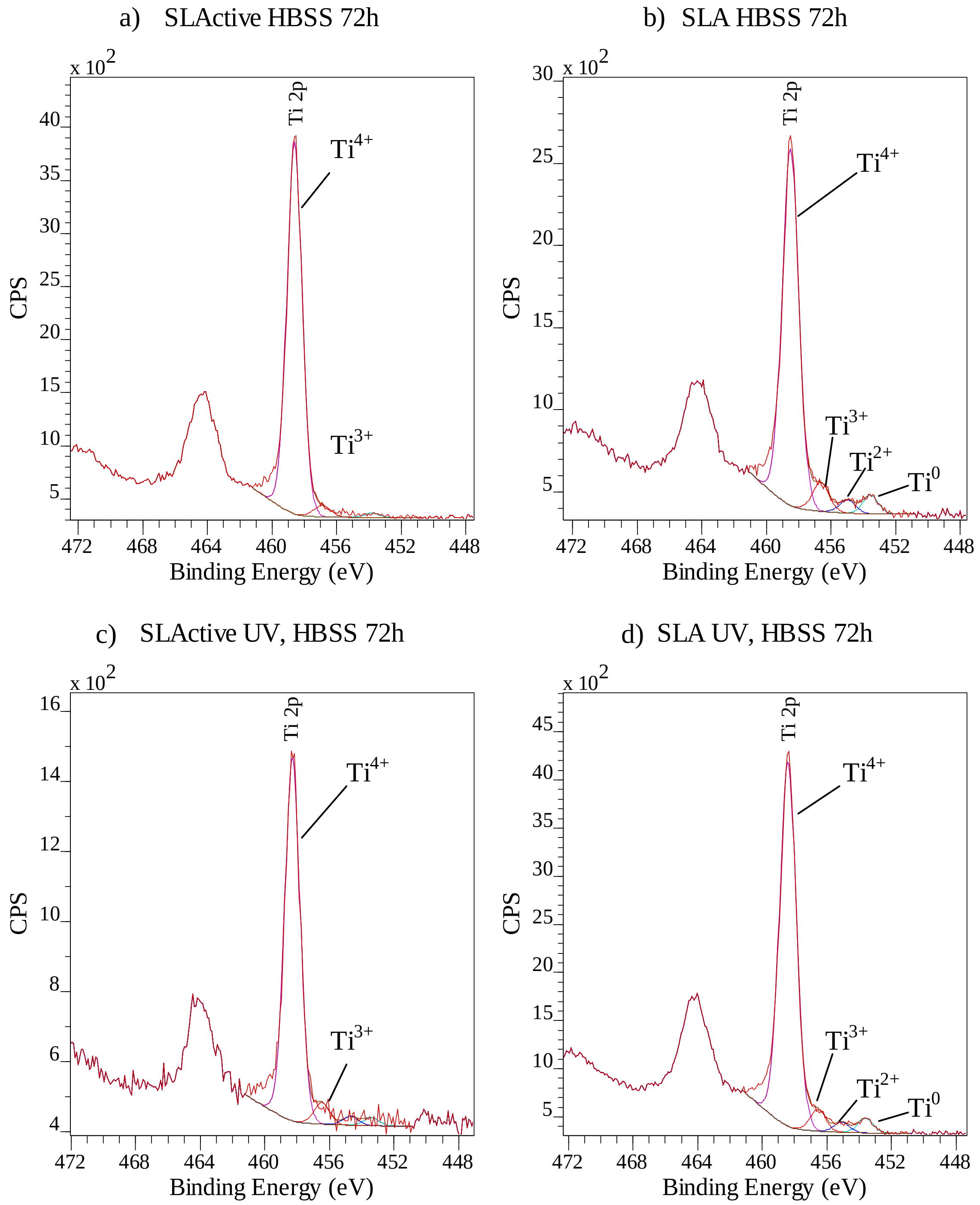

Figure 4.26 XPS Ti 2p spectra of SLActive and SLA samples after insertion in HBSS for 72h (a, b) and after UV treatment and consecutive insertion in HBSS for 72h (c, d).

The Ti 2p spectra (Fig. 4.24- 4.26) do not change much regardless of the treatment. A spectrum taken with 45^{o} grazing emission on SLA UV Hanks 24h sample (Fig. 4.25c) shows that the closer we get to the surface the less intermediate titanium oxides or metallic Ti we find. The specific spectrum resembles an SLActive spectrum. This confirms that we have a continuous layer of TiO_2 covering the Ti metal at the surface as expected.

High resolution C1s spectra recorded at a pass energy of 20 eV are displayed below:

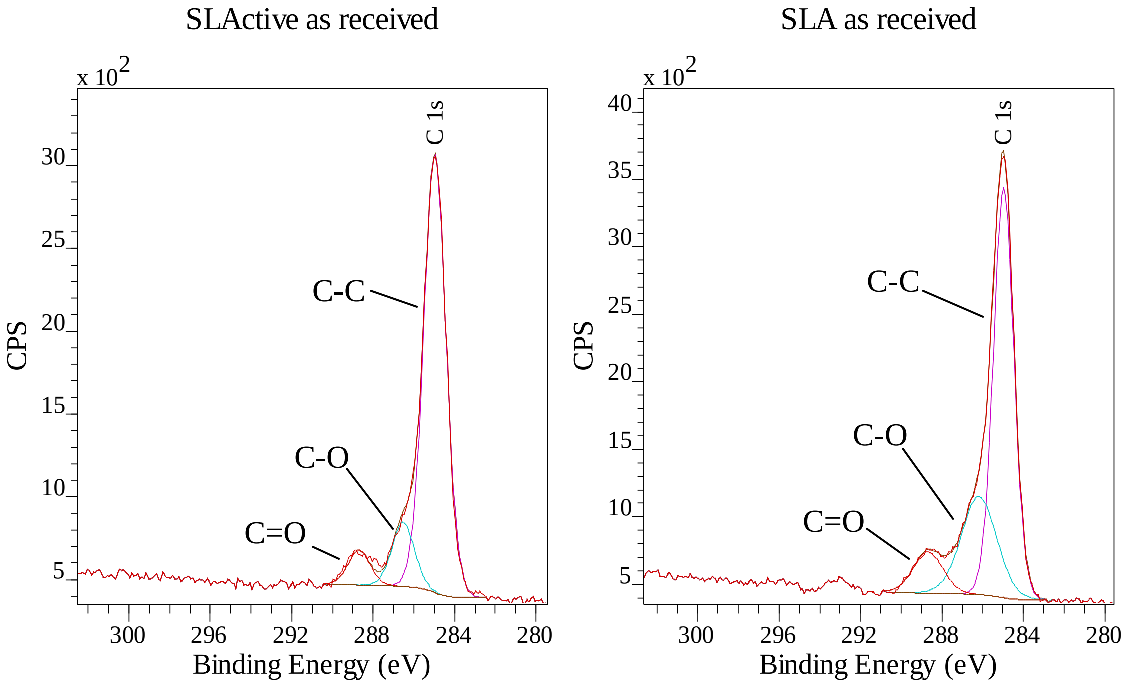

Figure 4.27 XPS C 1s spectra of SLActive and SLA samples as received.

The high resolution C 1s spectra at Fig. 4.27 display a dominant peak at ~285 eV, which corresponds to hydrocarbon (C-H and C-C) bonded carbon [156]. Different amount of contributions to the C 1s peak are also found at higher binding energies (286-290 eV), verifying the presence of other bond types in the adsorbed organic contamination layer such as C=O and C-OH bonds [154]. It is most likely that the contamination layer consists of a mixture of the most abundant contaminant molecules that exist in the preparation and handling environment of the samples, which must indeed bind relatively strongly to the sample surface to still remain there during the XPS analysis which takes place in vacuum. Considering these conditions, multilayers are mostly unlikely, given the binding between contaminant molecules should only be weak, unless external perturbations induce polymerization. It is therefore safe to suggest that the carbon contamination layer is predominantly comprised of organic molecules which are adsorbed as a result of air exposure. Carbon contamination is initially greater in SLA, which is expected given its non-aqueous storage. UV treatment seems to decrease organic carbon contamination at SLA, but not SLActive samples. The latter could be due to surface contamination from the UV source used for the test as suggested from the presence of F in the survey scan. When put in Hank's solution for 24h, carbon contamination seems to be similar between UV and non UV treated samples for both categories (Fig. 4.28 and 4.29). On the other hand, when they remain in the solution for at least 72h carbon contamination increases overall, but there seems to be a significant difference in the amount of carbon contamination between the SLActive UV (greater organic contamination) and non UV treated samples in figure 4.30 (left hand panels).

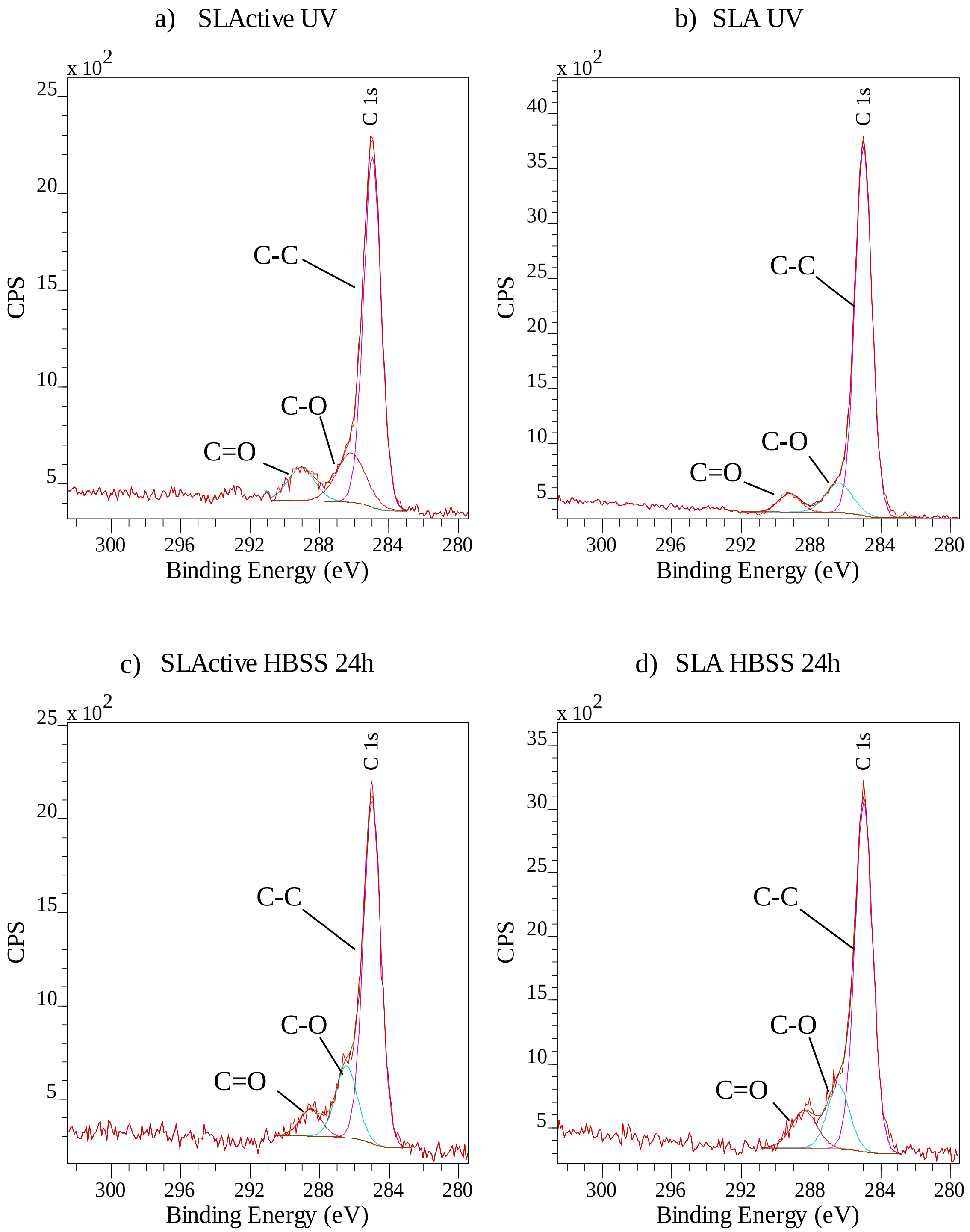

Figure 4.28 XPS C 1s spectra of SLActive and SLA samples after UV treatment (a, b) or after insertion in HBSS for 24h (c, d).

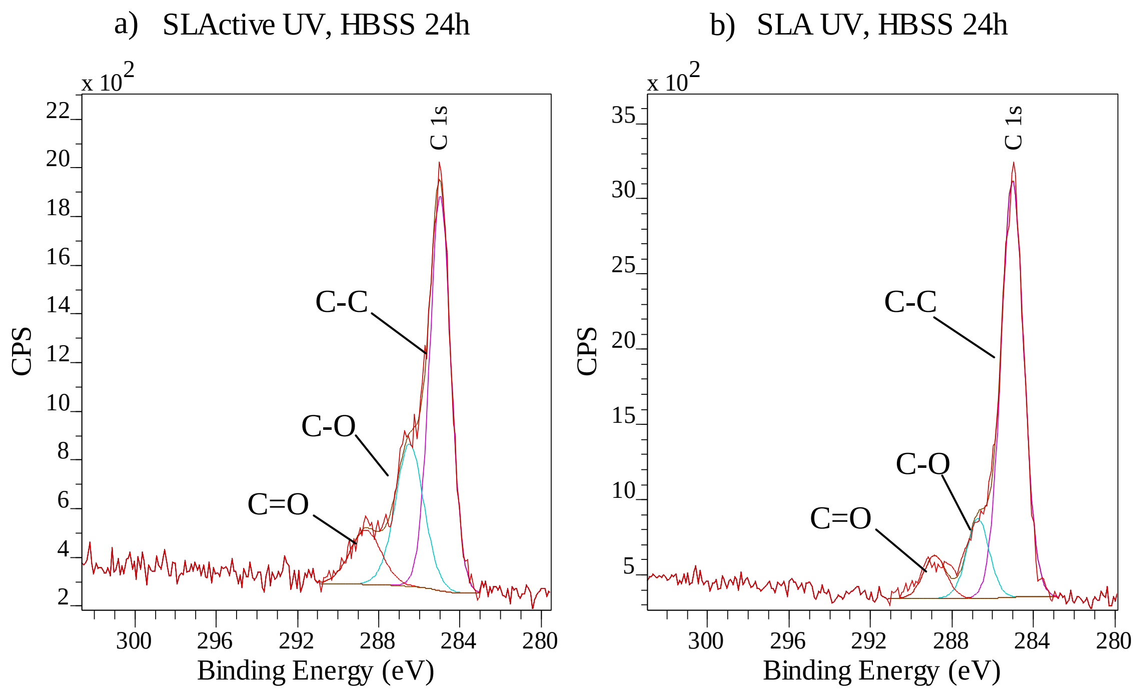
a) SLActive UV, HBSS 24h

b) SLA UV, HBSS 24h

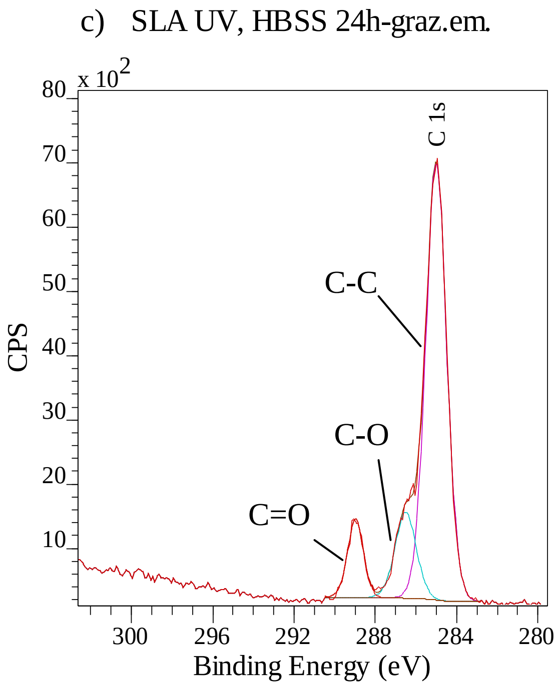
c) SLA UV, HBSS 24h-graz.em.

Figure 4.29 XPS C 1s spectra of SLActive (a) and SLA (b) samples after UV treatment and consecutive insertion in HBSS for 24h. XPS wide spectra (45° grazing emission) of SLA (c) samples after UV treatment and consecutive insertion in HBSS for 24h.

a) SLActive HBSS 72h

b) SLA HBSS 72h

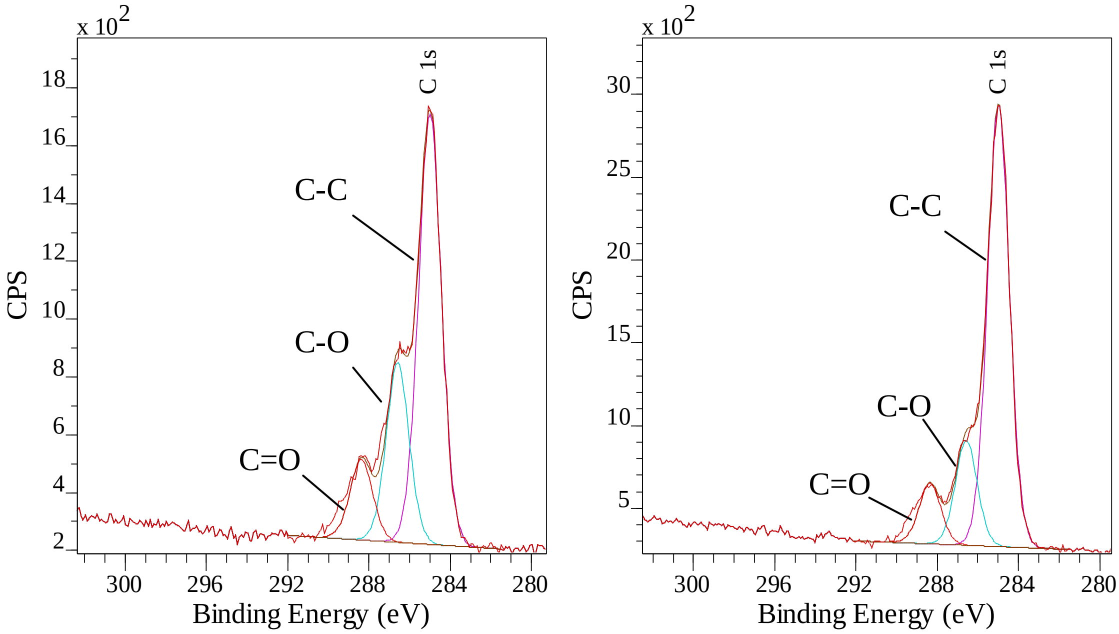

c) SLActive UV, HBSS 72h

d) SLA UV, HBSS 72h

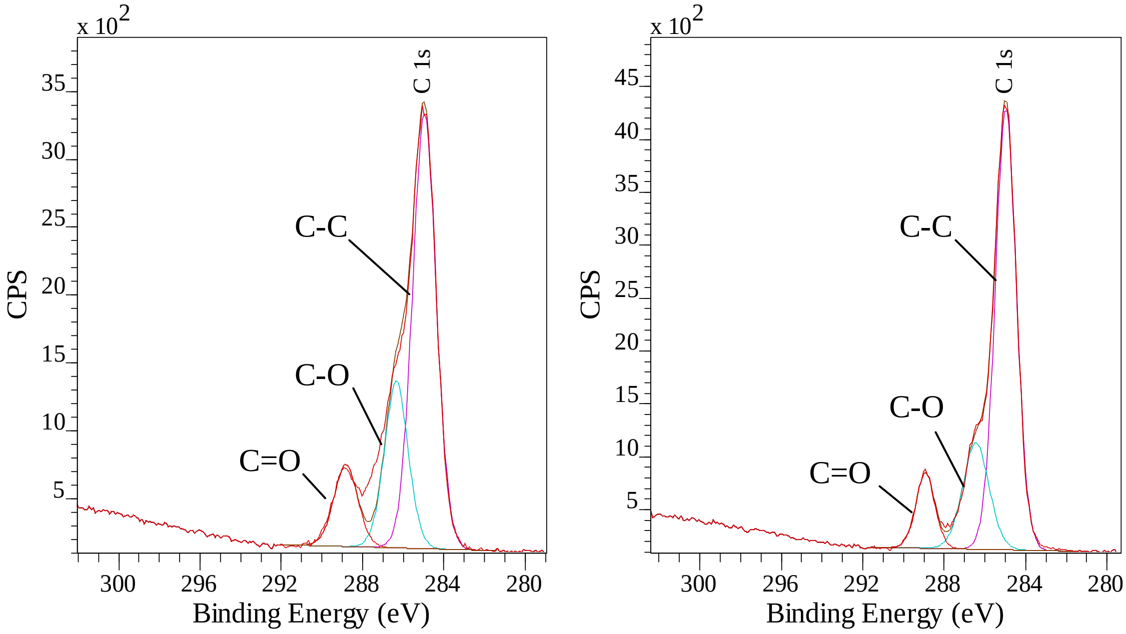

Figure 4.30 XPS C 1s spectra of SLActive and SLA samples after insertion in HBSS for 72h (a, b) and after UV treatment and consecutive insertion in HBSS for 72h (c, d).

High resolution O 1s spectra recorded at a pass energy of 20ev are displayed below (Fig. 4.31):

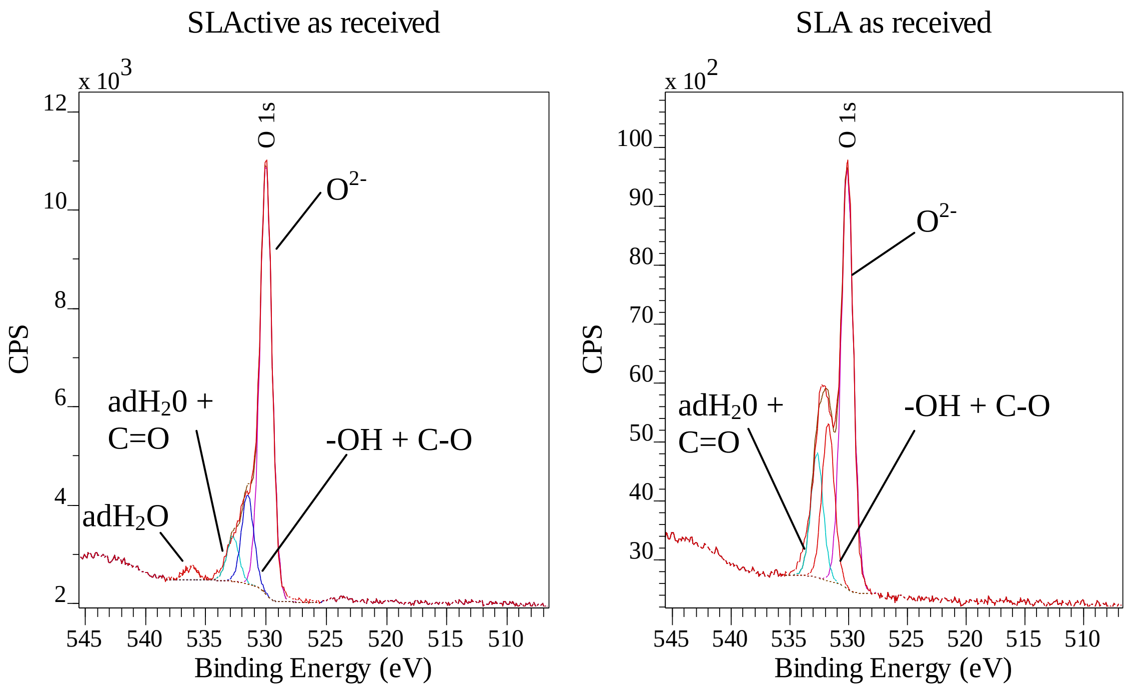
SLActive as received

SLA as received

Figure 4.31 XPS O 1s spectra of SLActive and SLA samples as received.

The main peak binding energy at the high resolution O1s spectra is ~530 eV which is assigned to the oxygen present in the surface oxide [154]. Moreover, the presence of additional spectral components at the higher energy side of the peak is indicated by the asymmetric shape of the O 1s peak. In all spectra without exception, individual peaks in the region of 531-533 eV were clearly identified, which can be assigned to oxygen present in C=O and C-OH bonds [156] in the contamination layer, or to OH groups and adsorbed H_2O at the oxide surface [157]. In our tests there seems to be a correlation between the intensities of the high energy contributions to the C 1s and O 1s peaks respectively, therefore we could assume that the asymmetry of the O 1s peak primarily comes from organically bonded oxygen, as in C=O or COOH. It cannot be ruled out, however, that some OH groups may be directly bonded to the oxide surface since many metal oxides do dissociate water and incorporate hydroxyl groups at their surfaces [155]. The O1s peak was fitted to three subpeaks [154] (Fig. 4.32): O^{2-} (E_B ~ 530 eV), -OH plus C-O (E_B ~ 531.5 eV), and adsorbed water (adsH_2O) plus C=O (E_B ~ 533 eV). In the SLActive samples an additional peak was registered at ~536 eV, which was assigned to adsorbed water.

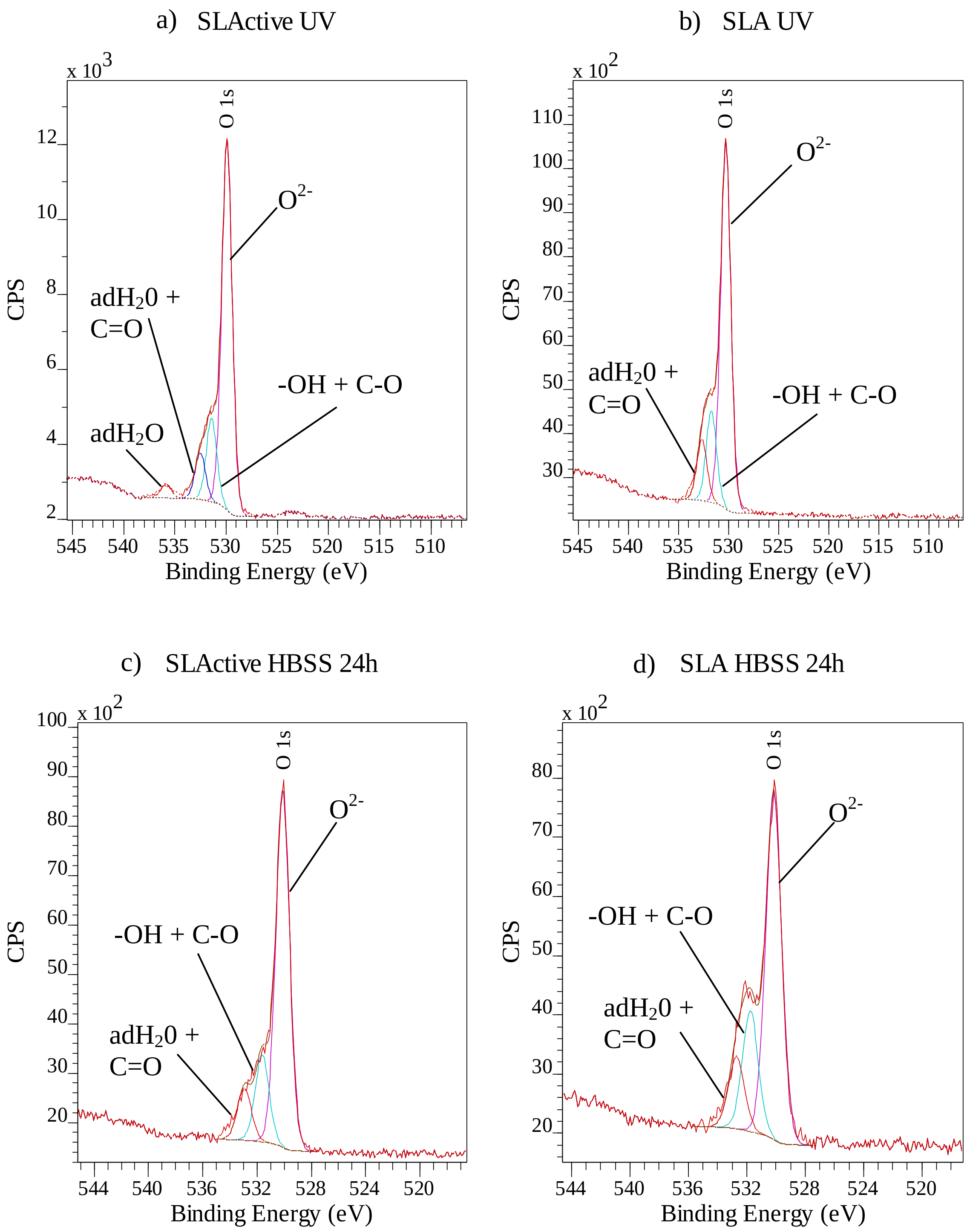

Figure 4.32 XPS O 1s spectra of SLActive and SLA samples after UV treatment (a, b) or after insertion in HBSS for 24h (c, d).

Following 24 hours incubation in Hanks' Balanced Salt Solution (HBSS) there appears to be very little change in the O 1s spectra.

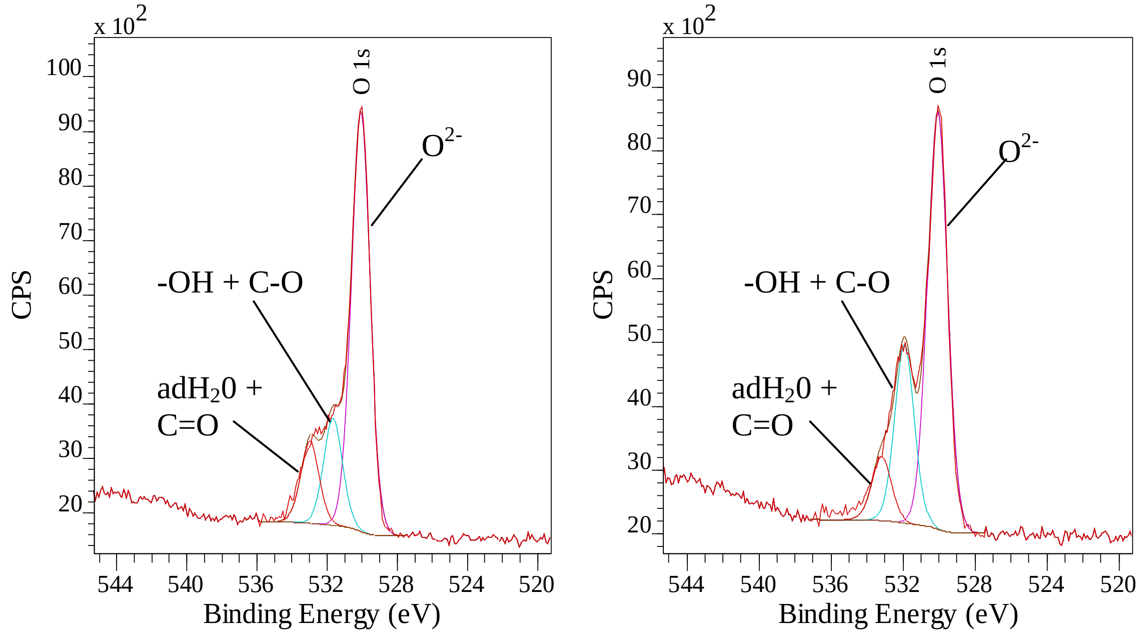

a) SLActive UV, HBSS 24h

b) SLA UV, HBSS 24h

c) SLA UV, HBSS 24h-graz.em.

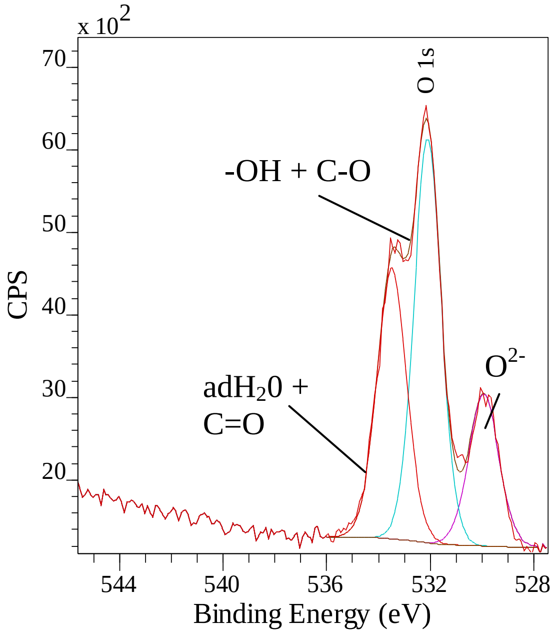

Figure 4.33 XPS O 1s spectra of SLActive (a) and SLA (b) samples after UV treatment and consecutive insertion in HBSS for 24h. XPS wide spectra (45° grazing emission) of SLA (c) samples after UV treatment and consecutive insertion in HBSS for 24h.

For the UV-treated SLA sample after 24 hours in Hanks' solution a grazing emission scan was recorded (Fig. 4.33c). This clearly shows that the species associated with hydrocarbons, adsorbed water and hydroxides lie on the top of the oxide layer.

Figure 4.34 shows as received SLA, as received SLActive and UV-treated SLA and SLActive samples on the same plot for ease of comparison. It can be seen that there is more contamination on the SLA as received surface compared to the SLActive, which appears as greater asymmetry on the oxygen peak in Fig. 4.31 and Fig. 4.34 (oxygen bonded to carbon and adsorbed OH species). UV treatment led to decreased O contamination only in the SLA sample, which explains the greater change in the asymmetry of the peak of the SLA O 1s peak at Fig. 4.32b and Fig. 4.34. No significant change is detected on the SLActive O 1s spectrum (Fig. 4.32a, Fig 4.34) after UV treatment relative to the non UV-treated sample.

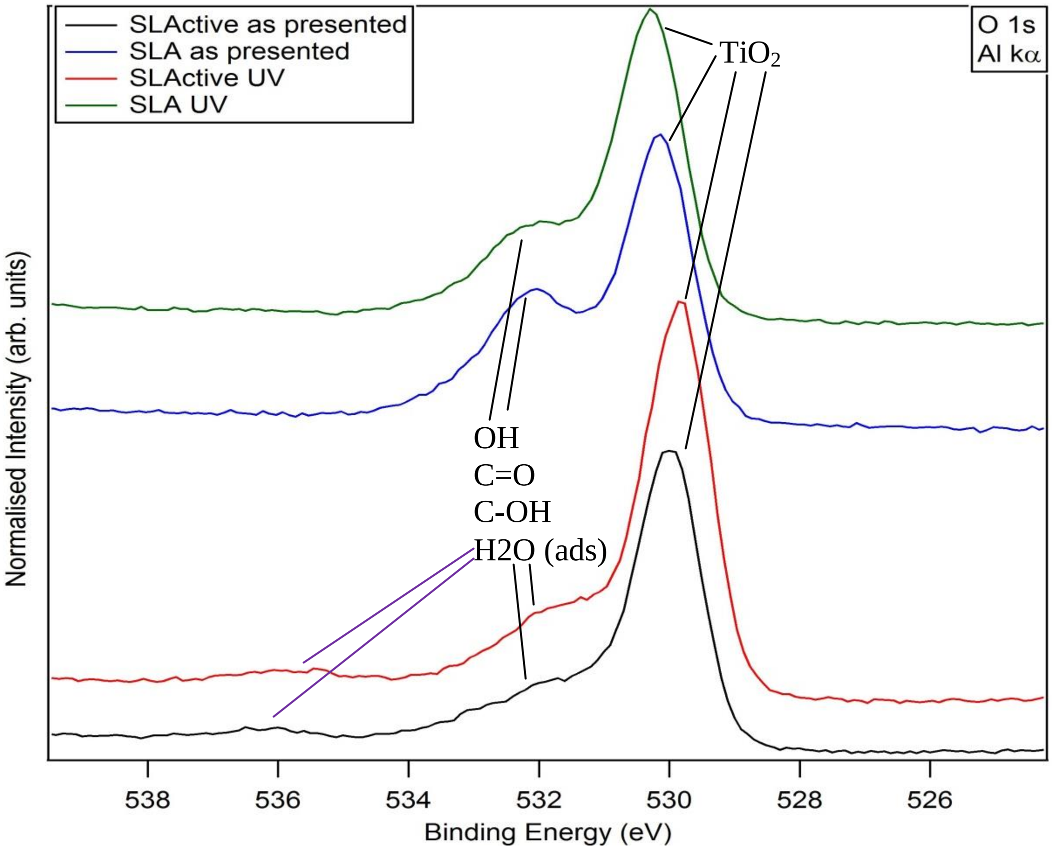

Figure 4.34 XPS spectra of O 1s from SLA and SLActive disks as received and after UV treatment.

It has been suggested that hydrocarbon contamination may affect the bioactivity of the Ti surface and could be reduced by ultraviolet irradiation [91]. Aita *et al* (2009) [158] supported the idea that UV light pre-treatment of titanium substantially promotes its osteoconductive capacity, with UV-catalytic progressive removal of hydrocarbons from the TiO_2 surface. It was suggested that in this way photofunctionalization of titanium enables faster and more solid establishment of bone–titanium integration. This was achieved after a 48h treatment with UV light. Our tests did not show a great decrease in carbon contamination, and where it did it was only for the SLA samples. The samples were only treated for 20 minutes though and this may have played a significant role in the results. Further tests and cell cultures are needed though to test the clinical value of any such effect. In any case, the hydrophilic SLA surfaces have been proved to exhibit better bioactivity than hydrophobic SLA surfaces by the N_2 protection or ultraviolet irradiation [9, 134, 158].

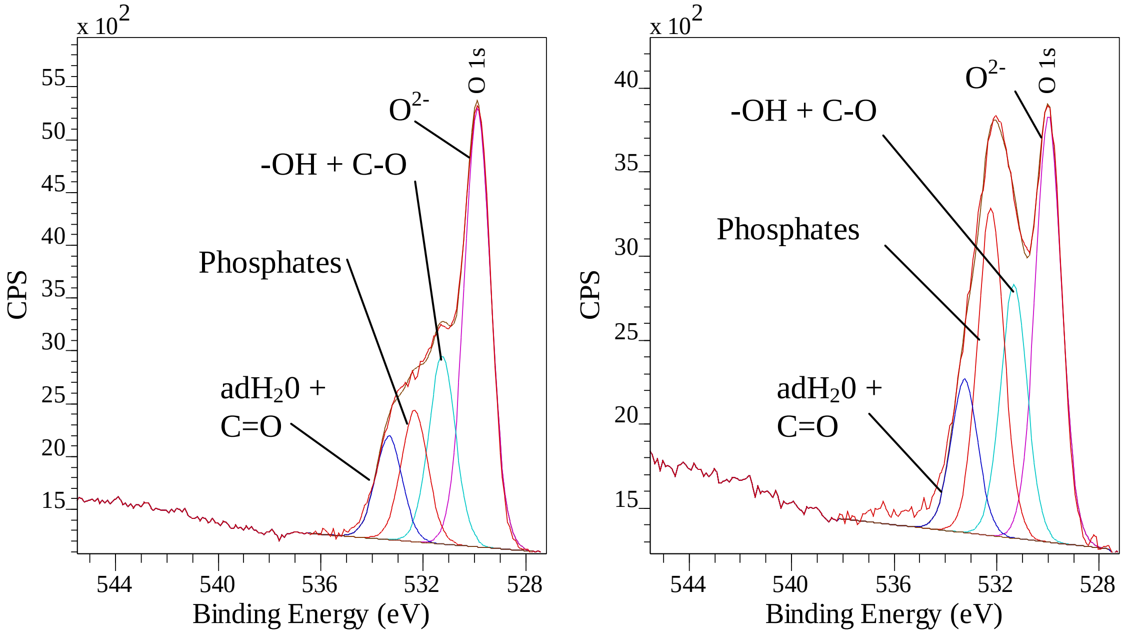

a) SLActive HBSS 72h

b) SLA HBSS 72h

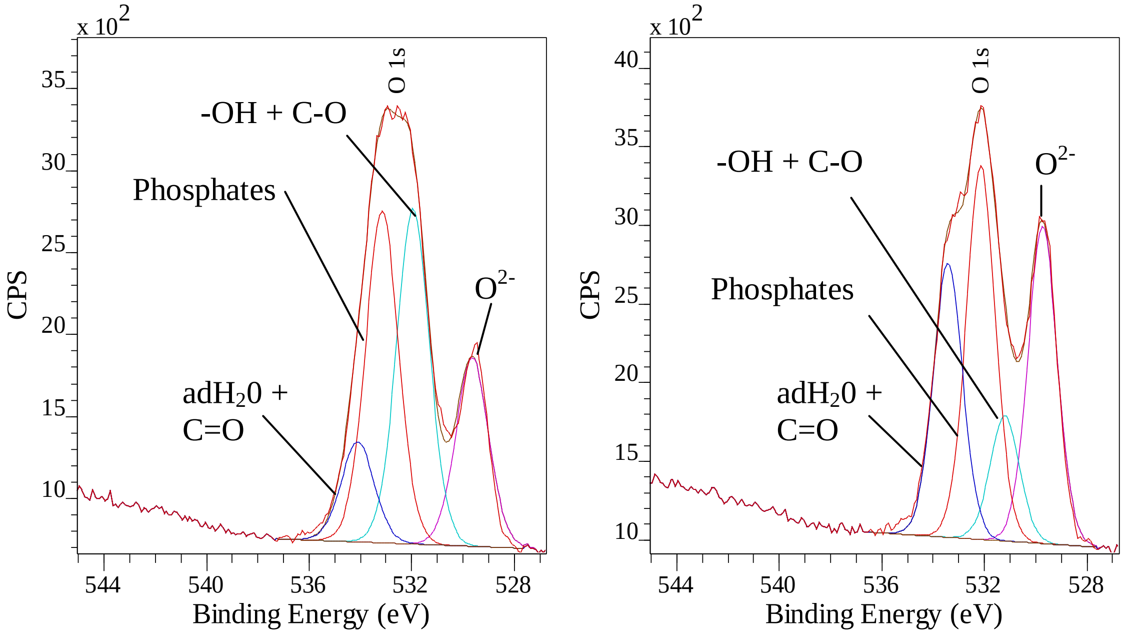

c) SLActive UV, HBSS 72h

d) SLA UV, HBSS 72h

Figure 4.35 XPS O 1s spectra of SLActive and SLA samples after insertion in HBSS for 72h (a, b) and after UV treatment and consecutive insertion in HBSS for 72h (c, d).

The O 1s spectra of both implant groups change significantly after 72h at Hank’s solution (see Fig. 4.35) and during peak fitting a fourth peak is added in the region of ~532.5 eV which may be indicative of the appearance of calcium phosphates at the sample surface [154]. One cannot, however, rule out that this peak contains contributions from residual phosphates, carbonates and sulphates from the Hanks’ solution which have not been removed from the surface by rinsing. In addition, the similarity in binding energy to that for OH before immersion in HBSS suggests that the immersion in aqueous solution also results in more hydroxyl species at the surface. The appearance of the fourth peak after 72h in Hanks’ solution is however concurrent with increase in the Ca and P % elemental composition. The increase in the % concentration of both calcium and phosphorous is greater in the non UV treated samples. XPS as a technique on its own cannot identify which ‘CaP’ phase this peak corresponds to and additional surface-sensitive analysis methods such as Surface X-ray Diffraction (SXRD) would be required to identify it [159].

4.4.2 Quantification

The tables below show quantification of the surface chemistry of SLA and SLActive samples before and after immersion in Hanks’ solution. XPS spectra were recorded from three positions on each sample (unless otherwise stated) and the average atomic % concentration and standard deviation are shown in the table.

Samples were subjected to XPS analysis in three slots of two days. In the first allocation the as received and UV treated samples were analysed. The samples were then incubated in Hanks’ solution for 24 hours before being analysed in the second allocation. The third allocation was used to analyse the 72 hour Hanks’ incubated samples. For more information on sample preparation see section 3.2.4.

	O 1s%	Ti 2p%	N 1s%	Ca 2p%	C 1s%	Cl 2p%	P 2p%
1	63.68(1.69)	15.62(0.28)	0.46(0.11)	0.02(0.02)	18.04(1.78)	1.97(0.18)	0.22(0.05)
2	64.12(0.59)	13.73(0.50)	0.86(0.15)	0.11(0.05)	20.87(0.59)	0.07(0.01)	0.23(0.02)
3	56.37(0.46)	13.97(0.33)	1.19(0.19)	0.11(0.09)	27.35(0.42)	0.34(0.01)	0.67(0.13)
4	66.1(0.91)	15.97(0.37)	0.48(0.15)	0.08(0.05)	17.3(0.93)	0.01(0.07)	0.06(0.06)
10	68.44(0.91)	16.36(0.37)	0.27(0.15)	0.12(0.05)	14.49(0.93)	0.08(0.07)	0.24(0.06)
20	63.32(0.91)	13.88(0.37)	1.32(0.15)	0	21.48(0.93)	0	0
30	70.02(0.91)	15.17(0.37)	0.63(0.15)	0.21(0.05)	13.65(0.93)	0	0.32(0.06)
40	64.74(0.91)	14.21(0.37)	0.55(0.15)	0.12(0.05)	19.94(0.93)	0.01(0.07)	0.43(0.06)

1: SLActive as received	**10: SLActive Hanks 24h**
2: SLA as received	**20: SLA Hanks 24h**
3: SLActive UV	**30: SLActive UV Hanks 24h**
4: SLA UV	**40: SLA UV Hanks 24h** **40 graz. em: 45° grazing emission**

	Ca/Ti	O/Ti	C/Ti	O^{-2}(BE 530eV) /Ti^{+4}(BE 458eV)	Ti 2p Metallic% (BE 453eV)
1	0.001(0.001)	4.08(0.06)	1.16(0.13)	3.23(0.09)	0.29(0.04)
2	0.008(0.004)	4.25(0.18)	1.20(0.09)	3.45(0.03)	0.98(0.16)
3	0.008(0.007)	4.43(0.08)	1.35(0.08)	3.00(0.04)	0.27(0.01)
4	0.005(0.004)	4.14(0.11)	1.08(0.10)	0.86(0.05)	1.02(0.07)
10	0.007(0.004)	4.18(0.11)	0.89(0.10)	3.22(0.05)	0.31(0.07)
20	0.000(0.004)	4.56(0.11)	1.55(0.10)	3.36(0.05)	0.92(0.07)
30	0.014(0.004)	4.62(0.11)	0.90(0.10)	3.36(0.05)	0
40	0.008(0.004)	4.56(0.11)	1.40(0.10)	3.55(0.05)	0.9(0.07)

Table 4.5 Quantitative information of SLA and SLActive surfaces as received, after UV treatment, after inserted in HBSS for 24h as received and after UV treatment and insertion in HBSS for 24h. Mean values and -in brackets- standard deviation.

	O 1s%	**Ti 2p%**	**N 1s%**	**Ca 2p%**	**C 1s%**	**Cl 2p%**	**P 2p%**
1	42.78(1.22)	7.49(0.22)	2.94(0.09)	1.32(0.02)	44.25(1.31)	0.05(0.02)	1.17(0.08)
2	33.66(0.77)	4.8(0.27)	2.36(0.31)	1.67(0.10)	56.71(0.57)	0.32(0.09)	0.49(0.01)
3	24.83(3.44)	1.33(0.57)	0.78(0.15)	0.31(0.08)	72.54(4.07)	0.03(0.01)	0.21(0.14)
4	33.41(13.54)	4.94(4.97)	1.52(1.12)	0.57(0.48)	58.92(20.77)	0.03(0.01)	0.63(0.65)
4-gr. em.	24.93(2.98)	1.96(1.05)	0.93(0.52)	0.27(0.04)	71.57(4.78)	0.03(0.01)	0.33(0.21)

1: SLActive, Hanks72h
2: SLA, Hanks 72h
3: SLActive UV, Hanks 72h
4: SLA UV, Hanks 72h
4 graz. em. : 45^{o} grazing emission

	Ca/Ti	**O/Ti**	**C/Ti**	**O^{-2}(BE 530eV) /Ti^{+4}(BE 458eV)**	**Ti 2p Metallic % (BE 453eV)**
1	0.18(0.04)	5.71(0.06)	5.92(0.35)	3.21(0.04)	0.18(0.02)
2	0.35(0.08)	7.03(0.45)	11.85(0.77)	3.18(0.09)	0.54(0.06)
3	0.24(0.05)	20.05(6.07)	61.12(29.49)	3.43(0.40)	0.13(0.03)
4	0.13(0.04)	10.93(8.27)	28.53(32.95)	3.22(0.05)	0.37(0.23)
4-graz.em.	0.15(0.06)	14.44(6.26)	43.6(25.94)	3.49(0.14)	0.26(0.09)

Table 4.6 Quantitative information of SLA and SLActive surfaces after insertion in HBSS for 72h as received and after UV treatment and insertion in HBSS for 72h. Mean values and -in brackets- standard deviation.

The results of the XPS elemental atomic percentage (%) as well as XPS Ca/Ti, O/Ti, C/Ti and O^{-2}/Ti^{+4} atomic ratios are listed above in Tables 4.5 and 4.6. The two as received samples have similar qualitative composition. Ti and O % concentration is 15.62% and 63.68% for the SLActive as received (ar) and 13.73% and 64.12% for the SLA as received (ar) respectively. SLActive (ar) demonstrate slightly lower C contamination, which is to be expected given its handling under N_2 gas and aqueous storage and subsequently less adsorption of CO_2 and other organic molecules from the atmosphere. Carbon levels were around 18.04% for SLActive and 20.87% for SLA. The difference is not as significant as reported in the literature, where C levels for SLA were between 32.7% and 36.4% [8, 46, 134, 160], whereas SLActive appears to have significantly lower carbon contamination and is in the region of 14-15% [8, 134, 160]. The difference in storage also accounts for almost untraceable Cl in the SLA sample. Traces of N and P are also detected in both implant groups. N is a common trace element in grade 4 cp Ti.

Fig. 4.36 shows the total concentration and atomic % concentration of O, Ti and C species at the surface following various surface treatments of the SLA and SLActive.

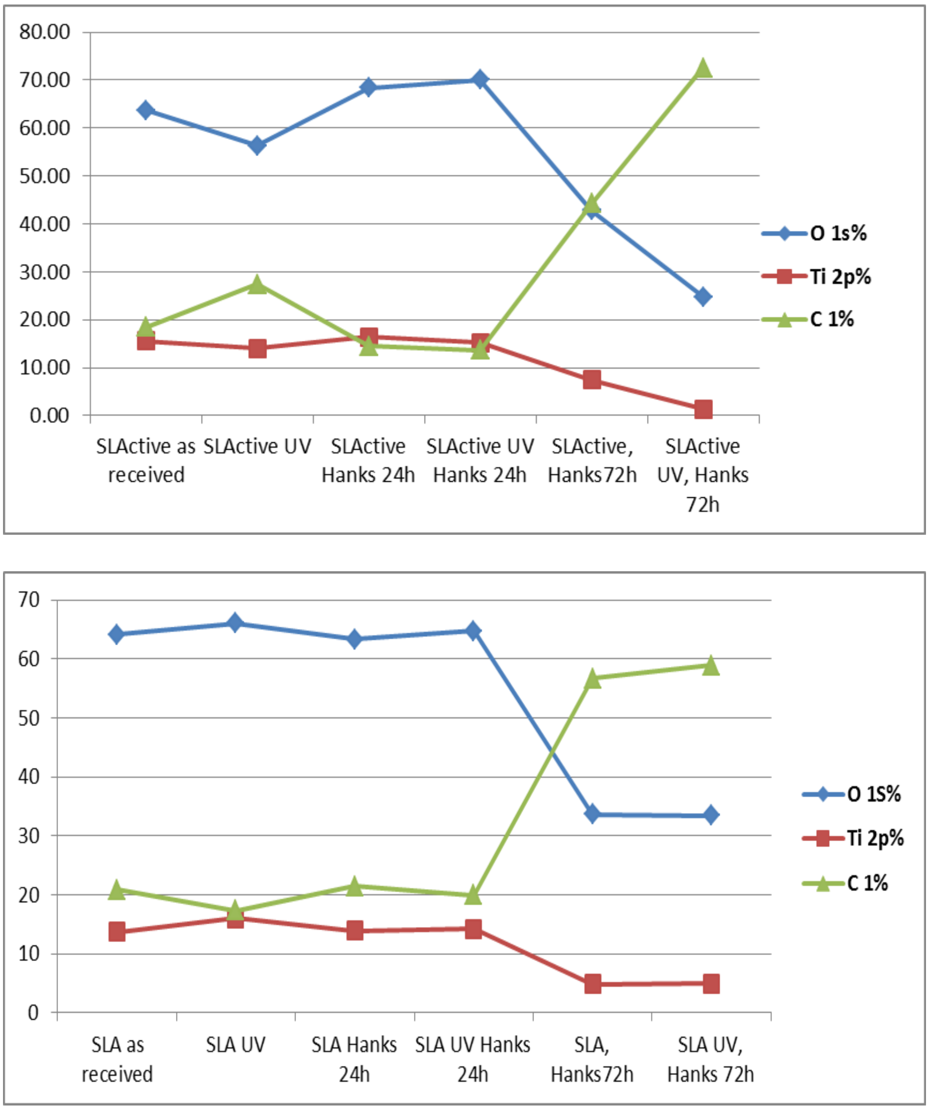

Figure 4.36 Changes in O 1s %, Ti 2p % and C 1s % after different treatments of the samples.

O 1s % and Ti 2p % concentrations (Fig. 4.36) do not appear to alter after UV treatment or insertion in Hank's solution for 24h, but they do appear similarly decreased after 72h in Hank's solution regardless of UV treatment or not. This can be explained by the increasing C contamination on the samples' surface. The origin of C contamination is not clear. It may come from carbonates in the Hanks' solution.

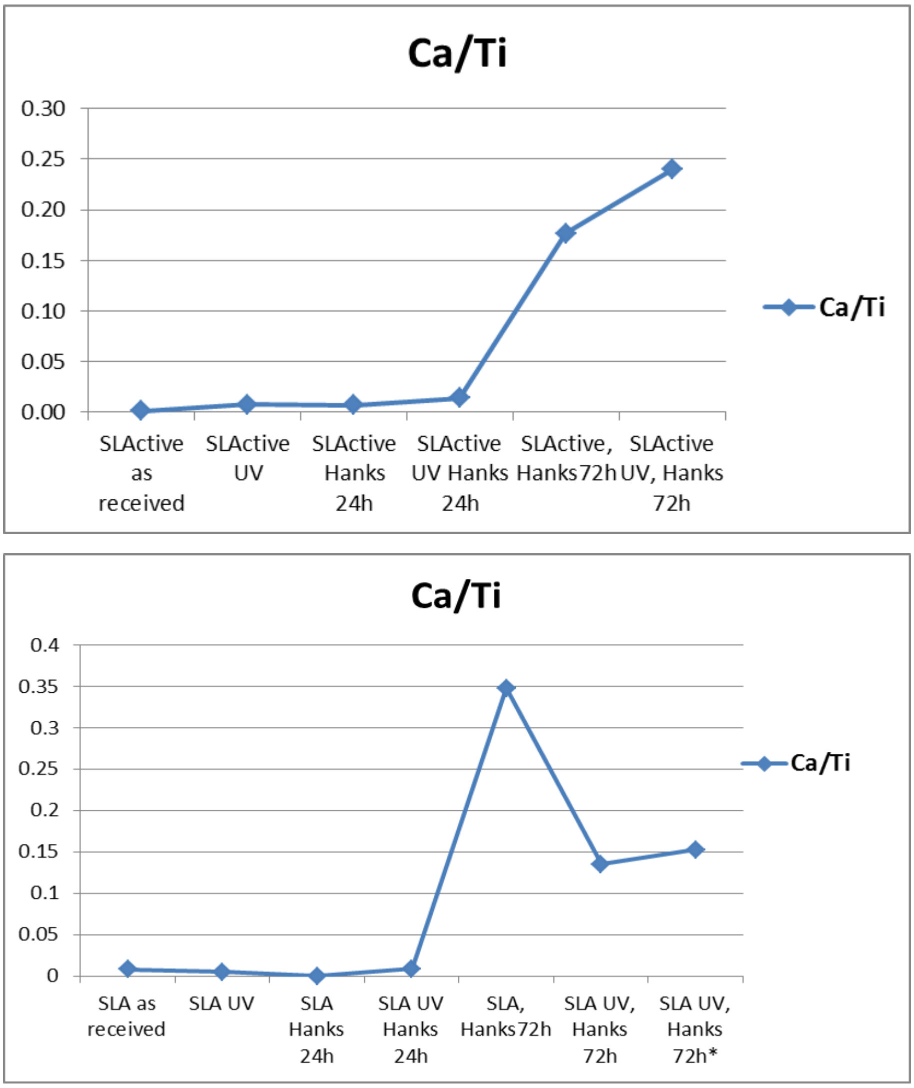

Figure 4.37 Changes in Ca/Ti ratio after different treatments of the SLActive and SLA samples (* stands for 45° grazing emission).

Calcium is almost untraceable in the as received samples' surfaces as well as on both UV treated samples. Its concentration starts to increase only slightly after the samples are stored in calcium-containing Hank's solution for 24 h and significantly more after they are stored in the same solution for more than 72 hours. This is also evident from the Ca/Ti ratios of the differently treated samples at Fig. 4.37 above. SLA and SLActive demonstrate similar behaviour.

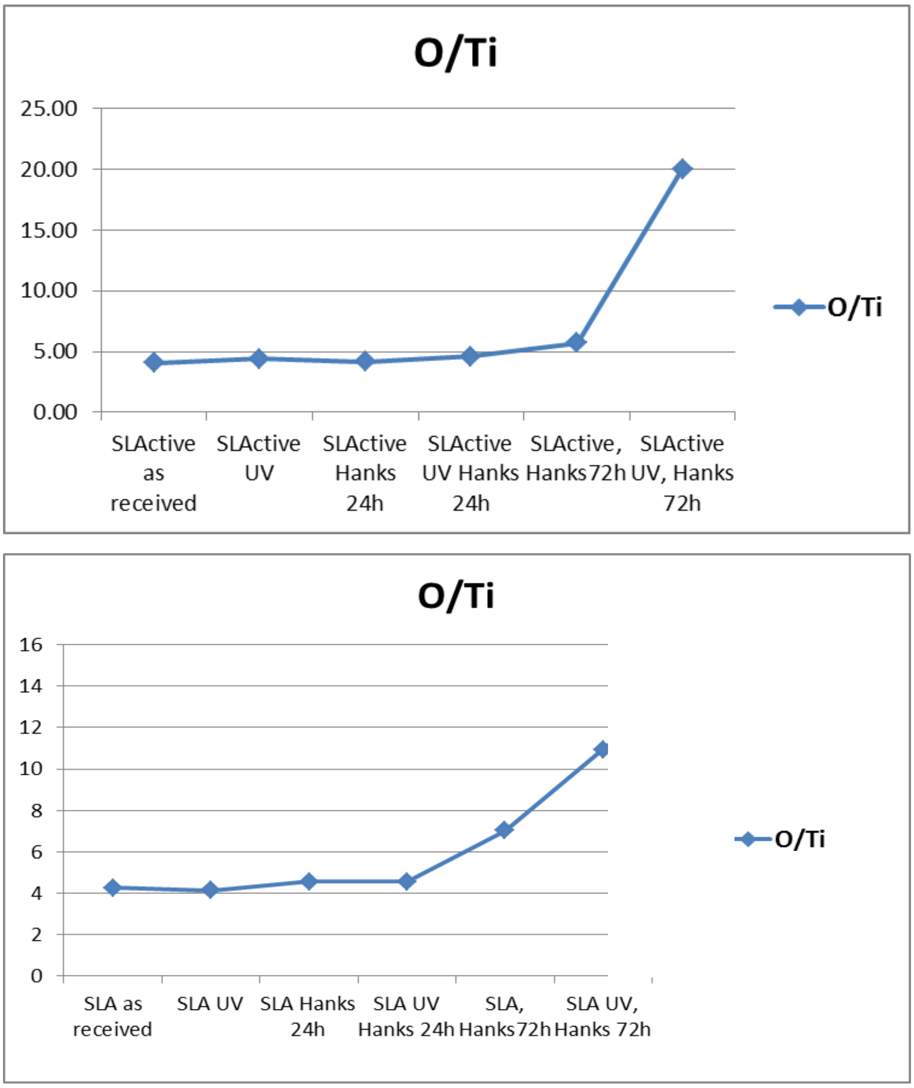

Figure 4.38 Changes in O/Ti ratio after different treatments of the SLActive and SLA samples.

The Oxygen/Titanium ratio (Fig. 4.38) remains relatively constant in the region of 4 for the as received, UV treated, Hank’s 24h and UV-Hank’s 24h samples. The ratio increases slightly for SLA and SLActive Hank’s 72h samples, whereas it increases significantly for both UV treated Hank’s 72h samples, reaching values of 20 for the SLActive and around 11 for the SLA sample. It can be inferred that UV treatment makes the studied surfaces more reactive to oxygen species, with the SLActive ones having an almost twice greater impact than the SLA ones. This is likely to be related to adsorption of carbon species such as carbonates or oxygen containing hydrocarbons. Interestingly, here is a sudden jump in Oxygen content for the SLActive sample which has been UV treated and placed in Hanks’ for 72 hours.

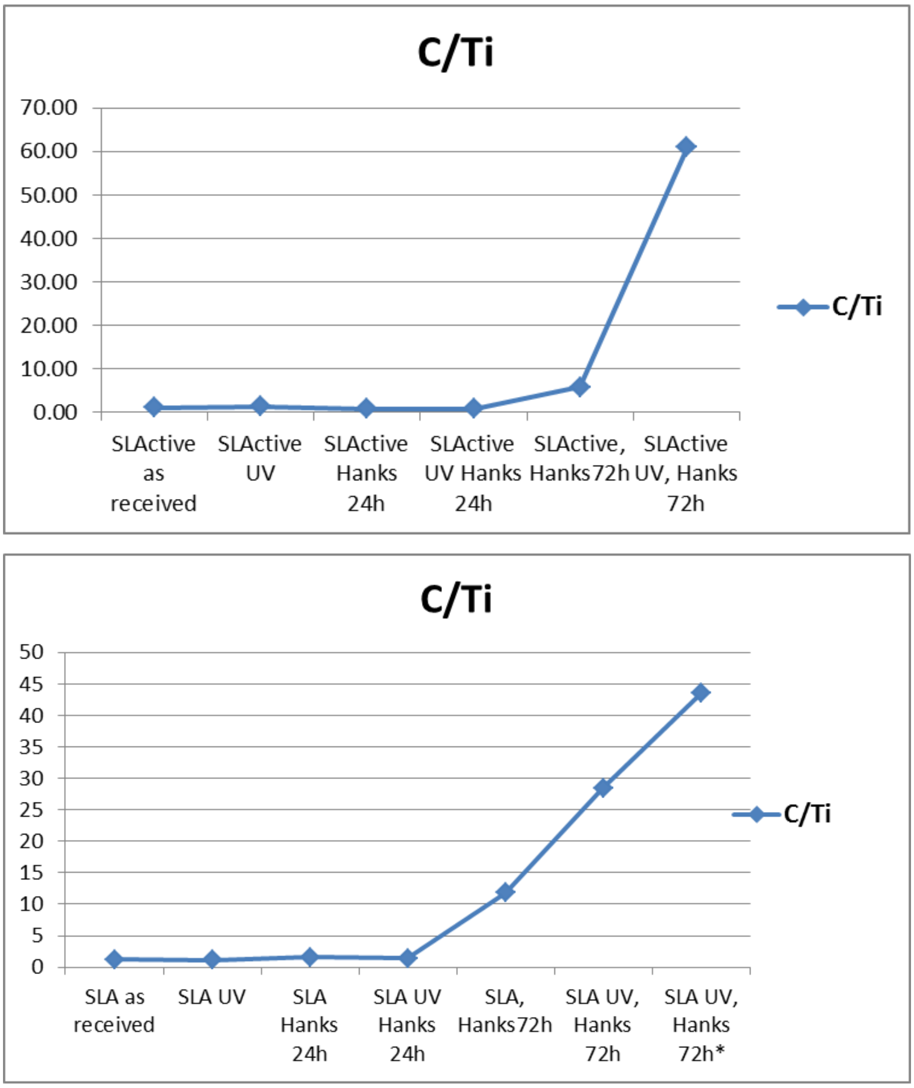

Figure 4.39 Changes in C/Ti ratio after different treatments of the SLActive and SLA samples (* stands for 45^o grazing emission).

Similar conclusions can be made for the Carbon/Titanium ratios (Fig. 4.39). It is expected to have increased carbon contamination the longer the samples are stored in Hank's solution. It is interesting though to notice that UV treated samples appear to have more C contamination than non-UV treated ones after both being 72h in Hank's solution. It is also evident in the intensity of C 1s peak at Fig 4.22 (c, d). This is consistent with the increase in Oxygen/Titanium ratio above and supports the deposition of a C-O species at the surface. This is in agreement with the O 1s spectra discussed earlier. In an attempt to determine the nature of the surface oxide the O^{2-} to Ti^{4+} ratio is shown in in Fig. 4.40 below.

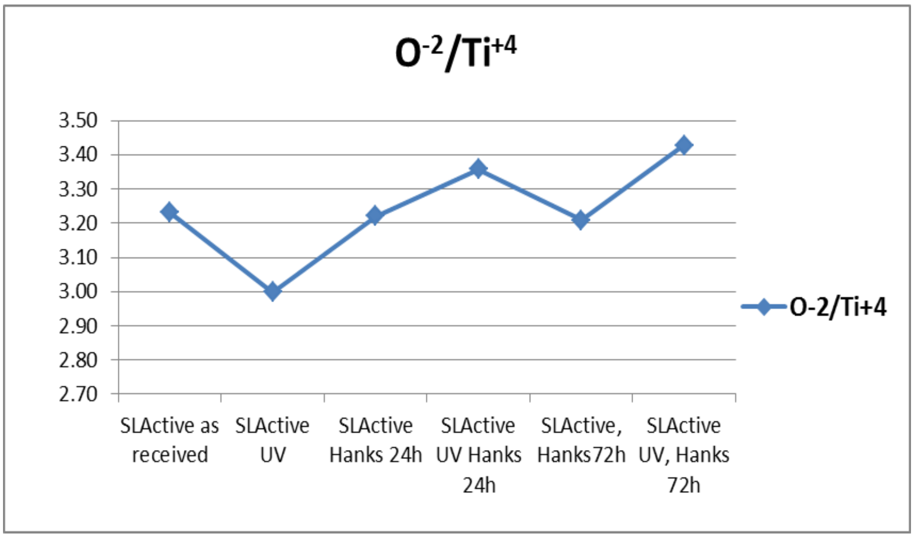

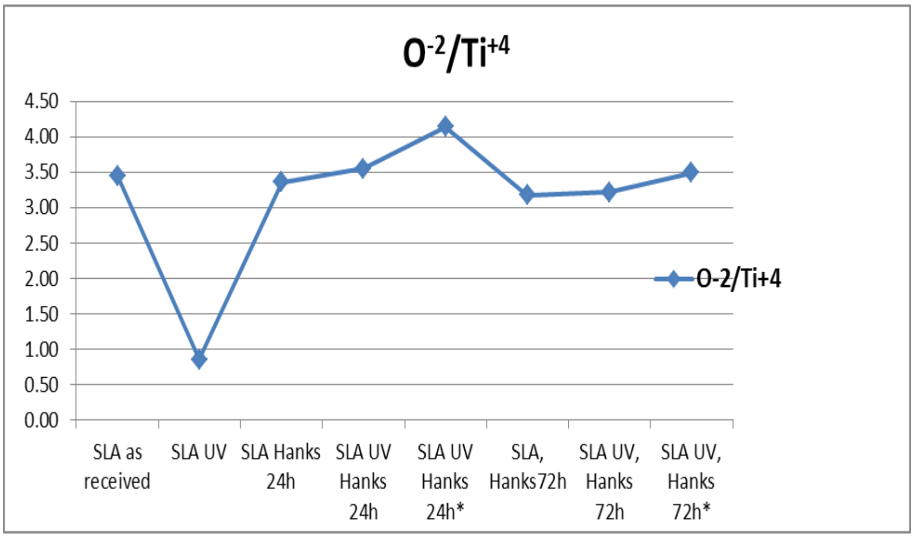

Figure 4.40 Changes in O^{-2}/Ti^{+4} ratio after different treatments of the SLActive and SLA samples (* stands for 45^{o} grazing emission).

The ratio of O^{-2}/Ti^{+4} seems to be consistently above three, with the exception of the SLA UV sample (0.86). This is likely to be due to the presence of other oxygen species at the same binding energy as the oxide on the O 1s signal. The complexity of the O 1s spectra and difficulties in fitting backgrounds to both Ti 2p and O 1s spectra lead to some degree of uncertainty in the precise origin of particular peaks. Slight variations in the background fitting can lead to significant changes in the area of single peaks. In addition, the presence of TiOH at the surface further complicates O^{2-} fitting since the fits overlap as shown in Fig. 4.31 – 4.33.

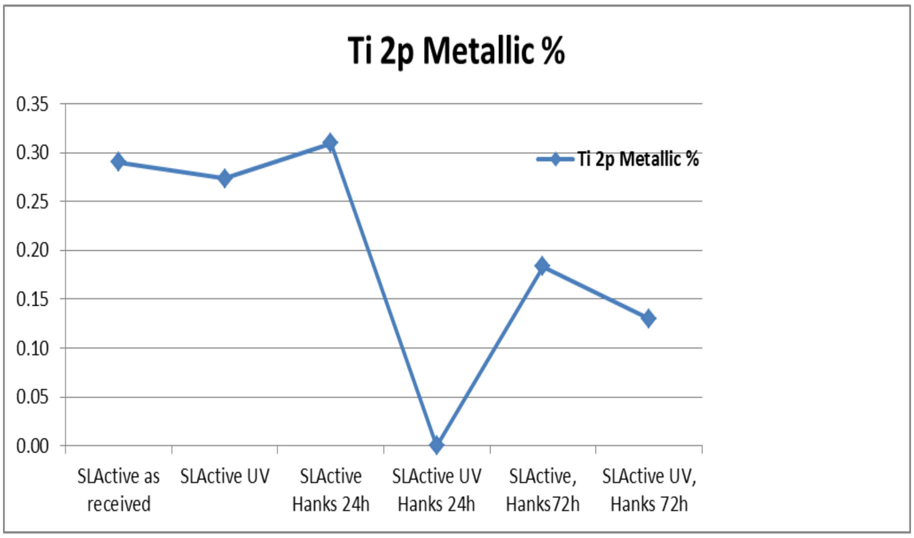

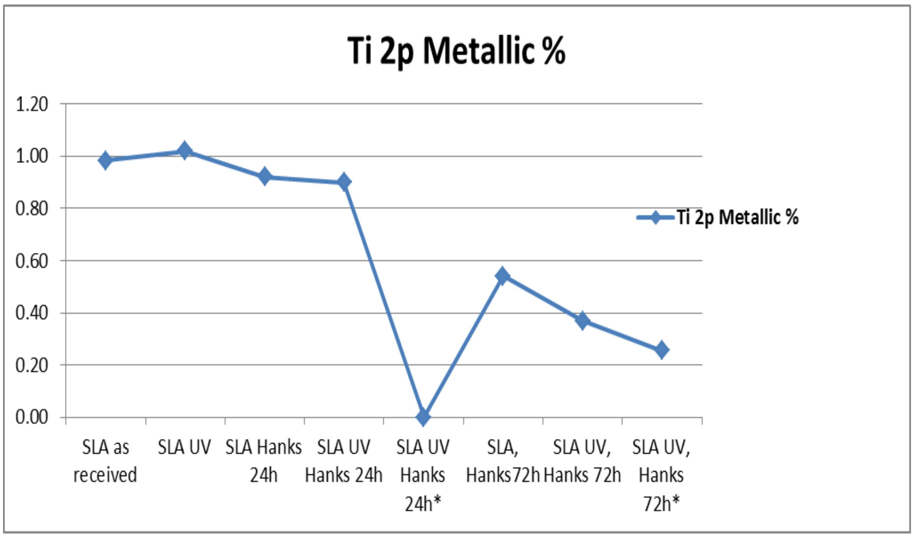

Figure 4.41 Changes in Ti 2p Metallic % after different treatments of the SLActive and SLA samples (* stands for 45^{o} grazing emission).

Fig. 4.41 shows the % concentration of metallic Ti at the surface. There seems to be increased presence of metallic Ti in SLA as received samples, which probably suggests that oxidation continues more efficiently in saline solution than in air. The higher metallic Ti concentration on SLA samples implies the existence of a thinner surface oxide layer, compared to SLActive. This layer seems to increase in thickness on the SLA samples the longer the samples are stored in Hanks' solution, suggesting that the neutral aqueous medium does indeed affect the oxidation of the surface. However, it should be noted that the effect of increased surface contamination observed in C 1s concentrations will lead to a reduction in the detection of buried Ti close to the surface.

5. CONCLUSIONS

Taking all the results above into consideration, the following conclusions were drawn:

The Sv roughness parameter for SLActive surface was found to be statistically significantly higher than SLA, although no significant differences were found between the two groups with regards to the rest of the amplitude parameters. The Null Hypothesis (Ho) (1) was rejected and the Alternative Hypothesis (Ha) (1) was accepted. Notably, in addition to the height descriptive parameters, at least one hybrid or spatial parameter is necessary for appropriate surface evaluation [71].

The SLActive samples appeared to be super-hydrophilic, while the SLA ones were hydrophobic. There was a significant difference in their wettability. The Null Hypothesis (Ho) (2) was rejected and the Alternative Hypothesis (Ha) (2) was accepted.

The SLActive surface displayed two distinct spectra, the first resembling the SLA spectrum (amorphous structure), whereas the second had some medium to broad peaks at 609, 422 and 256 cm^{-1}, which was not found at the SLA surface. The Null Hypothesis (Ho) (4) was rejected and the Alternative Hypothesis (Ha) (4) was accepted.

With limited time and limited access to high resolution XPS instrument it is not possible to categorically rule out or confirm Null Hypotheses (Ho) (3), (5) and (6). However there were subtle differences between the samples investigated in this study. Notably, 72 hour immersion of SLA and SLActive discs leads to the appearance of Ca and P species at the surface of the materials. This is also associated with the presence of a new oxygen species which may be in part due to Calcium phosphate material at the surface. UV treatment appeared to show no effect on the amount of CaP at the surface over the time scales here. This might suggest that results suggesting faster osseointegration following UV treatment maybe more in the effect of C contamination on cell attachment and proliferation than on mineralisation.

Suggestions for further work

Literature suggests that many factors contribute to the long term clinical success of dental implants, the majority of which are associated with their surface characteristics. Nowadays the interest seems to be directed towards the study of effects of nano-topography of implant surfaces on their clinical success, the study of techniques to decrease the risk of periimplant complications by local delivery of antibiotics or other surface alterations –standard protocol for treating periimplantitis is yet to be established- and lastly, the effect of different active ingredients in the implant-bone interface that may promote greater and faster biological response [144].

Unfortunately a lot of the published data comes from studies of specific implant systems which are often done in collaboration with manufacturing companies. A certain degree of bias can therefore not be ruled out. Only a few studies can be found that are actually comparing different implant systems [13, 35, 36, 136]. Esposito *et al.* (2005) [161] published a systematic review of failure rates between various root-formed osseointegrated dental implant systems after 5 years of loading. They concluded four randomised clinical trials in their analysis and found no clinically significant differences between the different studied systems. For that reason, more randomised clinical trials with greater patient samples need to be carried out, to facilitate the evaluation of the clinical relevance that dental implants' different surface characteristics may have.

In addition to the current focused interest on dental implantology research, stem cell technology is being increasingly used by several research groups in an attempt to achieve the generation of native oral tissue analogs that will be compatible with the patients' own [162-169]. The goal to create bioengineered teeth is noble, the research progress in the field appears to be promising and there is truth in the belief that regenerative medicine, and more specifically, tissue engineering is bound to play a significant and definitely revolutionary part in the future of clinical dentistry.

In the meantime, well-designed comparative surface characterization studies of various existing commercial implant systems are necessary, preferably with the use of standardised methods of analysis [144]. Specifically, large sample sets are required for XPS studies to promptly assess differences in surface chemistry between SLA and SLActive implants. XPS is a powerful technique for surface analysis and gives truly surface elemental composition, although it is limited in analysis of samples where the presence of water is likely to influence material behaviour. This will expedite progress in the research, since understanding and comparison of findings will be considerably easier. In combination with well-executed clinical trials, they will provide further data to correlate specific implant surface characteristics with long term successfully osseointegrated dental implants.

REFERENCES

[1] Raman Spectroscopy. http://www.andor.com/learning-academy/raman-spectroscopy-an-introduction-to-raman-spectroscopy.

[2] Dental implant overview Part 1. http://www.dentalorg.com/dental-implant-overview-part-1.html2011.

[3] Banwell C, McCash E. Foundamentals of Molecular Spectroscopy. Fourth ed: McGraw-Hill Book Company Europe; 1994.

[4] Raman energy levels. http://en.wikipedia.org/wiki/File:Raman_energy_levels.svg.

[5] Terheyden H, Lang NP, Bierbaum S, Stadlinger B. Osseointegration - communication of cells. Clin Oral Implants Res. 2011.

[6] Parker JC, Siegel RW. Raman microprobe study of nanophase TiO_2 and oxidation-induced spectral changes. Journal of Materials Research. 1990;5:1246-52.

[7] Buser D, Schenk RK, Steinemann S, Fiorellini JP, Fox CH, Stich H. Influence of surface characteristics on bone integration of titanium implants. A histomorphometric study in miniature pigs. J Biomed Mater Res. 1991;25:889-902.

[8] Rupp F, Scheideler L, Olshanska N, de Wild M, Wieland M, Geis-Gerstorfer J. Enhancing surface free energy and hydrophilicity through chemical modification of microstructured titanium implant surfaces. J Biomed Mater Res A. 2006;76:323-34.

[9] Buser D, Broggini N, Wieland M, Schenk RK, Denzer AJ, Cochran DL, Hoffmann B, Lussi A, Steinemann SG. Enhanced bone apposition to a chemically modified SLA titanium surface. J Dent Res. 2004;83:529-33.

[10] Cochran DL, Morton D, Weber HP. Consensus statements and recommended clinical procedures regarding loading protocols for endosseous dental implants. Int J Oral Maxillofac Implants. 2004;19 Suppl:109-13.

[11] Albrektsson T, Brånemark PI, Hansson HA, Lindström J. Osseointegrated titanium implants. Requirements for ensuring a long-lasting, direct bone-to-implant anchorage in man. Acta Orthop Scand. 1981;52:155-70.

[12] Albrektsson T, Wennerberg A. Oral implant surfaces: Part 1--review focusing on topographic and chemical properties of different surfaces and in vivo responses to them. Int J Prosthodont. 2004;17:536-43.

[13] Albrektsson T, Wennerberg A. Oral implant surfaces: Part 2--review focusing on clinical knowledge of different surfaces. Int J Prosthodont. 2004;17:544-64.

[14] Buser D, Schenk RK, Steinemann S, Fiorellini JP, Fox CH, Stich H. Influence of surface characteristics on bone integration of titanium implants. A histomorphometric study in miniature pigs. J Biomed Mater Res. 1991;25:889-902.

[15] Cochran DL, Nummikoski PV, Higginbottom FL, Hermann JS, Makins SR, Buser D. Evaluation of an endosseous titanium implant with a sandblasted and acid-etched surface in the canine mandible: radiographic results. Clin Oral Implants Res. 1996;7:240-52.

[16] Cochran DL, Schenk RK, Lussi A, Higginbottom FL, Buser D. Bone response to unloaded and loaded titanium implants with a sandblasted and acid-etched surface: a histometric study in the canine mandible. J Biomed Mater Res. 1998;40:1-11.

[17] Rosenberg ES, Cho SC, Elian N, Jalbout ZN, Froum S, Evian CI. A comparison of characteristics of implant failure and survival in periodontally compromised and periodontally healthy patients: a clinical report. Int J Oral Maxillofac Implants. 2004;19:873-9.

[18] Bornstein MM, Valderrama P, Jones AA, Wilson TG, Seibl R, Cochran DL. Bone apposition around two different sandblasted and acid-etched titanium implant surfaces: a histomorphometric study in canine mandibles. Clin Oral Implants Res. 2008;19:233-41.

[19] Cranin A. Glossary of implant terms. Journal of Oral Implantology. 1990:57-63.

[20] Misch C. Contemporary Implant Dentistry. 2008.

[21] Malet J, Mora F, Bouchard P. Implant Dentistry at a glance. First ed: John Wiley & Sons, Ltd.; 2012.

[22] Roberts W, Garetto L, Simmons K. Endosseous implants for rigid orthodontic anchorage. In: Bell W, editor. Surgical correction of dentofacial deformities. Philadelphia: WB Saunders; 1992.

[23] Roberts WE, Nelson CL, Goodacre CJ. Rigid implant anchorage to close a mandibular first molar extraction site. J Clin Orthod. 1994;28:693-704.

[24] Roberts WE, Arbuckle GR, Analoui M. Rate of mesial translation of mandibular molars using implant-anchored mechanics. Angle Orthod. 1996;66:331-8.

[25] Roberts W, Hartsfiels JJ. Multidisciplinary management of congenita and acquired compensated malocclussions: diagnosis, etioogy and treatment planning. Indiana Dental Association Journal. 1997:42.

[26] Deguchi T, Takano-Yamamoto T, Kanomi R, Hartsfield JK, Roberts WE, Garetto LP. The use of small titanium screws for orthodontic anchorage. J Dent Res. 2003;82:377-81.

[27] Kanomi R. Mini-implant for orthodontic anchorage. J Clin Orthod. 1997;31:763-7.

[28] Luzi C, Verna C, Melsen B. Immediate loading of orthodontic mini-implants: a histomorphometric evaluation of tissue reaction. Eur J Orthod. England2009. p. 21-9.

[29] marketsandmarkets.com. Global Dental Implants Market (2010 -2015). http://www.marketsandmarkets.com/Market-Reports/Dental-Implants-Market-241.html2010.

[30] Brånemark PI, Adell R, Breine U, Hansson BO, Lindström J, Ohlsson A. Intra-osseous anchorage of dental prostheses. I. Experimental studies. Scand J Plast Reconstr Surg. 1969;3:81-100.

[31] Nguyen DT, Orgill DP, Murphy GF. Chapter 4: The Pathophysiologic Basis for Wound Healing and Cutaneous Regeneration. Biomaterials For Treating Skin Loss: Boca Raton/Cambridge: CRC Press (US) & Woodhead Publishing (UK/Europe) 2009. p. 25-7.

[32] Ferencyk M, Rovensky J, Mat’ha V, Herold M. Kompendium der Immunologie. 2006.

[33] Schenk RK, Buser D. Osseointegration: a reality. Periodontol 2000. 1998;17:22-35.

[34] Zinelis S, Thomas A, Syres K, Silikas N, Eliades G. Surface characterization of zirconia dental implants. Dental Materials. 2010;26:295-305.

[35] Albrektsson T, Wennerberg A. Oral implant surfaces: Part 1--review focusing on topographic and chemical properties of different surfaces and in vivo responses to them. Int J Prosthodont. 2004;17:536-43.

[36] Fandridis J, Papadopoulos T. Surface characterization of three titanium dental implants. Implant Dent. 2008;17:91-9.

[37] Brånemark PI, Hansson BO, Adell R, Breine U, Lindström J, Hallén O, Ohman E. Osseointegrated implants in the treatment of the edentulous jaw. Experience from a 10-year period. Scand J Plast Reconstr Surg Suppl. 1977;16:1-132.

[38] Meredith N. Assessment of implant stability as a prognostic determinant. Int J Prosthodont. 1998;11:491-501.

[39] Friberg B, Sennerby L, Linden B, Gröndahl K, Lekholm U. Stability measurements of one-stage Brånemark implants during healing in mandibles. A clinical resonance frequency analysis study. Int J Oral Maxillofac Surg. 1999;28:266-72.

[40] Glauser R, Meredith N. Diagnostische Möglichkeiten zur Evaluation der Implantatstabilität. Implantologie. 2001:147–60.

[41] Lekholm U, Zarb G. Patient selection and preparation. In: Brånemark P-I, Zarb G, Albrektsson T, editors. Tissue-Integrated Prostheses: Osseointegration in Clinical Dentistry. Chicago: Quintessence; 1985.

[42] Turkyilmaz I, McGlumphy EA. Influence of bone density on implant stability parameters and implant success: a retrospective clinical study. BMC Oral Health. 2008;8:32.

[43] Dohan Ehrenfest DM, Coelho PG, Kang BS, Sul YT, Albrektsson T. Classification of osseointegrated implant surfaces: materials, chemistry and topography. Trends Biotechnol. 2010;28:198-206.

[44] Coelho PG, Granjeiro JM, Romanos GE, Suzuki M, Silva NR, Cardaropoli G, Thompson VP, Lemons JE. Basic research methods and current trends of dental implant surfaces. J Biomed Mater Res B Appl Biomater. 2009;88:579-96.

[45] Kim KH, Ramaswamy N. Electrochemical surface modification of titanium in dentistry. Dent Mater J. 2009;28:20-36.

[46] Le Guéhennec L, Soueidan A, Layrolle P, Amouriq Y. Surface treatments of titanium dental implants for rapid osseointegration. Dent Mater. 2007;23:844-54.

[47] Rupp F, J. G-G, Geckeler KE. Dental implant materials: Surface modification and interface phenomena. Adv Mater. 1996;8:254-7.

[48] Chiang C-Y, Chiou S-H, Yang W-E, Hsu M-L, Yung M-C, Tsai M-L, Chen L-K, Huang H-H. Formation of TiO_2 nano-network on titanium surface increases the human cell growth. Dental materials : official publication of the Academy of Dental Materials. 2009;25:1022-9.

[49] Posch T, Kerschbaum F, Fabian D, Mutschke H, Dorschner J, Tamanai A, Henning T. Infrared Properties of Solid Titanium Oxides: Exploring Potential Primary Dust Condensates. The Astrophysical Journal Supplement Series. 2003;49.

[50] Syres K. Molecular Adsorption on TiO_2 Surfaces: Modelling Potential Biomedical and Photovoltaic Devices PhD Thesis, The University of Manchester. 2010.

[51] Diebold U. Surface Science Reports. 2003;48.

[52] Di Paola A, Addamo M, Bellardita M, Cazzanelli E, Palmisano L. Preparation of photocatalytic brookite thin films. Thin Solid Films. 2007;515:3527-9.

[53] The crystal structure of Brookite. http://paulingblog.wordpress.com/2010/01/12/the-crystal-structure-of-brookite/2010.

[54] Brookite Mineral Data. http://www.webmineral.com/data/Brookite.shtml.

[55] The mineral Brookite. http://www.galleries.com/Brookite.

[56] Hoang VV. Structural properties of simulated liquid and amorphous TiO_2. Physica Status Solidi B. 2007;244:1280-7.

[57] Mao C, Li H, Cui F, Ma C, Feng Q. Oriented growth of phosphates on polycrystalline titanium in a process mimicking biomineralization. Journal of Crystal Growth. 1999;206:308-21.

[58] Chatwin C. Adsorption of Complex Organic Molecules on Anatase and Rutile TiO_2 Surfaces: Towards New Biosensors and Photovoltaics. PhD Thesis, The Unversity of Manchester. 2007.

[59] Schwarz F, Wieland M, Schwartz Z, Zhao G, Rupp F, Geis-Gerstorfer J, Schedle A, Broggini N, Bornstein MM, Buser D, Ferguson SJ, Becker J, Boyan BD,Cochran DL. Potential of chemically modified hydrophilic surface characteristics to support tissue integration of titanium dental implants. J Biomed Mater Res B Appl Biomater. 2009;88:544-57.

[60] Ratner B, Hoffman A, Schoen F, Lemons J. Biomaterials Science: An Introduction to Materials in Medicine: Academic Press; 1996.

[61] Briggs D, Seah M. Practical Surface Anaysis by Auger and X-ray Photoelectron Spectroscopy: Wiley & Sons; 1987.

[62] Fairley N. CasaXPS Manual 2.3.15 Introduction to XPS and AES. Casa Software Ltd; 2009.

[63] Seah M, Dench W. Quantitative electron spectroscopy of surfaces: A standard data base for electron inelastic mean free paths in solids. Surface and Interface Analysis. 1979;1:2-11.

[64] Vickerman J. Surface analysis - The principal techniques: John Wiley & Sons; 1997.

[65] Chen Q. Advanced Surface Science. http://www.sussex.ac.uk/Users/qc25/teaching/Surfsci3.pdf2009.

[66] Solid State Physics. http://en.wikipedia.org/wiki/Solid-state_physics.

[67] Raman Spectroscopy Applications. http://en.wikipedia.org/wiki/Raman_spectroscopy#Applications.

[68] Som S, Foing B. Thermal degradation of organic material by portable laser Raman spectrometry. International Journal of Astrobiology. 2012;11:177-86.

[69] Optical Profilometry. http://www.mri.psu.edu/facilities/mcl/techniques/optProfilometry.asp2012.

[70] Optical Profiler Basics. http://www.zemetrics.com/optical-profilers-about.shtml.

[71] Wennerberg A, Albrektsson T. On implant surfaces: a review of current knowledge and opinions. Int J Oral Maxillofac Implants. 2010;25:63-74.

[72] Zecchino M. Characterizing Surface Quality: Why Average Roughness is Not Enough http://www.veeco.com/pdfs/appnotes/an511_roughness_64.pdf: Veeco Instruments, Inc.; 2003.

[73] Surface Measurement Parameters for Wyko® Optical Profilers. http://zeus.plmsc.psu.edu/~manias/MatSc597/docs/di_roughness.pdf2002.

[74] Stajer A, Ungvari K, Pelsoczi IK, Polyanka H, Oszko A, Mihalik E, Rakonczay Z, Radnai M, Kemény L, Fazekas A, Turzó K. Corrosive effects of fluoride on titanium: Investigation by X-ray photoelectron spectroscopy, atomic force microscopy and human epithelial cell culturing. Journal of Biomedical Materials Research Part A. 2008;87A:450-8.

[75] http://ortholab.buffalo.edu/bioelectrochemresearch.

[76] Viornery C, Chevolot Y, Leonard D, Aronsson BO, Pechy P, Mathieu HJ, Descouts P, Graetzel M. Surface modification of titanium with phosphonic acid to improve bone bonding: Characterization by XPS and ToF-SIMS. Langmuir. 2002;18:2582-9.

[77] de Maeztu MA, Alava JI, Gay-Escoda C. Ion implantation: surface treatment for improving the bone integration of titanium and Ti6Al4V dental implants. Clinical Oral Implants Research. 2003;14:57-62.

[78] Morra M, Cassinelli C, Bruzzone G, Carpi A, Di Santi G, Giardino R, Fini M. Surface chemistry effects of topographic modification of titanium dental implant surfaces: 1. Surface analysis. International Journal of Oral & Maxillofacial Implants. 2003;18:40-5.

[79] Morra M, Cassinelli C, Meda L, Fini M, Giavaresi G, Giardino R. Surface analysis and effects on interfacial bone microhardness of collagen-coated titanium implants: A rabbit model. International Journal of Oral & Maxillofacial Implants. 2005;20:23-30.

[80] Vanzillotta PS, Sader MS, Bastos IN, Soares GD. Improvement of in vitro titanium bioactivity by three different surface treatments. Dental Materials. 2006;22:275-82.

[81] Berardi D, Colagiovanni M, Scoccia A, Raffaelli L, Manicone PF, Perfetti G. Evaluation of a new laser surface implant: Scanning Electron Microscopy / Energy Dispersive X-Ray and X-Ray Photoelectron Spectroscopy analyses. Journal of Biological Regulators and Homeostatic Agents. 2008;22:161-7.

[82] Lopes CB, Sathaiah S, Pinheiro ALB, Duarte J, Martins MC. Laser biomodulation in bone implants: A Raman spectral study. Conference on Lasers in Dentistry IX. San Jose, Ca 2003. p. 164-9.

[83] Lopes CB, Pinheiro ALB, Sathaiah S, Duarte J, Martins MC. Infrared laser light reduces loading time of dental implants: A Raman spectroscopic study. Photomedicine and Laser Surgery. 2005;23:27-31.

[84] Liu HY, Wang XJ, Wang LP, Lei FY, Wang XF, Ai HJ. Effect of fluoride-ion implantation on the biocompatibility of titanium for dental applications. Applied Surface Science. 2008;254:6305-12.

[85] Kang BS, Sul YT, Oh SJ, Lee HJ, Albrektsson T. XPS, AES and SEM analysis of recent dental implants. Acta Biomaterialia. 2009;5:2222-9.

[86] Watanabe K, Okawa S, Kanatani M, Homma K. Surface analysis of commercially pure titanium implant retrieved from rat bone. part 1: Initial biological response of sandblasted surface. Dental Materials Journal. 2009;28:178-84.

[87] Petrini P, Arciola CR, Pezzali I, Bozzini S, Montanaro L, Tanzi MC, Speziale P, Visai L. Antibacterial activity of zinc modified titanium oxide surface. International Journal of Artificial Organs. 2006;29:434-42.

[88] Xua JA, Ding G, Li JL, Yang SH, Fang BS, Sun HC, Zhou Y. Zinc-ion implanted and deposited titanium surfaces reduce adhesion of Streptococccus mutans. Applied Surface Science. 2010;256:7540-4.

[89] Lai CH, Chang YY, Huang HL, Kao HY. Characterization and antibacterial performance of ZrCN/amorphous carbon coatings deposited on titanium implants. Thin Solid Films. 2011;520:1525-31.

[90] Pisarek M, Roguska A, Andrzejczuk M, Marcon L, Szunerits S, Lewandowska M, Janik-Czachor M. Effect of two-step functionalization of Ti by chemical processes on protein adsorption. Applied Surface Science. 2011;257:8196-204.

[91] Zhang EW, Wang YB, Shuai KG, Gao F, Bai YJ, Cheng Y, Xiong XL, Zheng YF, Wei SC. In vitro and in vivo evaluation of SLA titanium surfaces with further alkali or hydrogen peroxide and heat treatment. Biomedical Materials. 2011;6.

[92] Weinlaender M, Reumer J, Kenney EB, Moy PK, Adar F. Raman microprobe investigation of the calcium-phosphate phases of three commercially available plasma-flame-sprayed Hydroxyapatite-coated dental implants. Journal of Materials Science-Materials in Medicine. 1992;3:397-401.

[93] Frauchiger VM, Schlottig F, Gasser B, Textor M. Anodic plasma-chemical treatment of CP titanium surfaces for biomedical applications. Biomaterials. 2004;25:593-606.

[94] Vasconcellos MAZ, Hinrichs R, Javorsky CS, Giuriatti G, da Costae J. Micro-Raman characterization of plasma nitrided Ti6Al4V-ELI. Surface & Coatings Technology. 2007;202:275-9.

[95] Machado ACP, Oliveira MV, Pereira RP, Carvalho YR, Cairo CAA. In vivo Evaluation of Porous Titanium Implants with Biomimetic Coating. Bioceramics 21. 2009;396-398:179-82.

[96] Stadlinger B, Hennig M, Eckelt U, Kuhlisch E, Mai R. Comparison of zirconia and titanium implants after a short healing period. A pilot study in minipigs. Int J Oral Maxillofac Surg. 2010;39:585-92.

[97] Kollar A, Huber S, Mericske E, Mericske-Stern R. Zirconia for teeth and implants: a case series. Int J Periodontics Restorative Dent. 2008;28:479-87.

[98] van Brakel R, Cune MS, van Winkelhoff AJ, de Putter C, Verhoeven JW, van der Reijden W. Early bacterial colonization and soft tissue health around zirconia and titanium abutments: an in vivo study in man. Clin Oral Implants Res. 2011;22:571-7.

[99] Bozzini B, Carlino P, Mele C. Electrochemical behaviour and surface characterisation of Zr exposed to an SBF solution containing glycine, in view of dental implant applications. Journal of Materials Science-Materials in Medicine. 2011;22:193-200.

[100] Melero H, Fernandez J, Dosta S, Guilemany JM. Characterization of new bioactive coatings of hydroxyapatite and TiO_2 obtained by High-Velocity Oxy-Fuel. Boletin De La Sociedad Espanola De Ceramica Y Vidrio. 2011;50:59-64.

[101] AlSamak S, Bitsanis E, Makou M, Eliades G. Morphological and structural characteristics of orthodontic mini-implants. J Orofac Orthop. 2012;73:58-71.

[102] Silva MhPD, Soares GA, Elias CN, Lima JHC, Schechtman H, Gibson IR, Best SM. Surface analysis of titanium dental implants with different topographies. Materials Research. 2000;3:61.

[103] Juodzbalys G, Sapragoniene M, Wennerberg A. New Acid Etched Titanium Dental Implant Surface. Stomatologija, Baltic Dental and Maxillofacial Journal. 2003:101-5.

[104] RZ L. Apatites in biological systems. Prog Cryst Growth Charact. 1981:1-45.

[105] Lu HB, Campbell CT, Graham DJ, Ratner BD. Surface Characterization of Hydroxyapatite and Related Calcium Phosphates by XPS and TOF-SIMS. Analytical Chemistry. 2000;72:2886-94.

[106] Chusuei CC, Goodman DW, Van Stipdonk MJ, Justes DR, Loh KH, Schweikert EA. Solid−Liquid Adsorption of Calcium Phosphate on TiO_2. Langmuir. 1999;15:7355-60.

[107] Jung UW, Hwang JW, Choi DY, Hu KS, Kwon MK, Choi SH, Kim HJ. Surface characteristics of a novel hydroxyapatite-coated dental implant. J Periodontal Implant Sci. 2012;42:59-63.

[108] Boyna BD, Dean DD, Lohmann CH. The titanium bone cell interface in vitro: The role of the surface in promoting osteointegration. In: Brunette DM, Tengvall P, Textor M, Thomsen P, editors. Titanium in Medicine. Berlin: Springer-Verlang; 2001.

[109] Rupp F, Scheideler L, Eichler M, Geis-Gerstorfer J. Wetting behavior of dental implants. Int J Oral Maxillofac Implants. 2011;26:1256-66.

[110] Riley DJ, Bavastrello V, Covani U, Barone A, Nicolini C. An in-vitro study of the sterilization of titanium dental implants using low intensity UV-radiation. Dental materials : official publication of the Academy of Dental Materials. 2005;21:756-60.

[111] Duske K, Koban I, Kindel E, Schroder K, Nebe B, Holtfreter B, Jablonowski L, Weltmann KD, Kocher T. Atmospheric plasma enhances wettability and cell spreading on dental implant metals. J Clin Periodontol. 2012;39:400-7.

[112] Lu H, Zhou L, Wan L, Li S, Rong M, Guo Z. Effects of storage methods on time-related changes of titanium surface properties and cellular response. Biomed Mater. 2012;7:055002.

[113] Ueno T, Yamada M, Hori N, Suzuki T, Ogawa T. Effect of ultraviolet photoactivation of titanium on osseointegration in a rat model. The International journal of oral & maxillofacial implants. 2010;25:287-94.

[114] Ueno T, Yamada M, Suzuki T, Minamikawa H, Sato N, Hori N, Takeuchi K, Hattori M, Ogawa T. Enhancement of bone-titanium integration profile with UV-photofunctionalized titanium in a gap healing model. Biomaterials. England: 2009 Elsevier Ltd; 2010. p. 1546-57.

[115] Wang R, Hashimoto K, Fujishima A, Chikuni M, Kojima E, Kitamura A, Shimohigoshi M, Watanabe T. Light-induced amphiphilic surfaces. Nature. 1997;388:431-2.

[116] Takeuchi M, Sakamoto K, Martra G, Coluccia S, Anpo M. Mechanism of photoinduced superhydrophilicity on the TiO2 photocatalyst surface. J Phys Chem B. 2005;109:15422-8.

[117] Watanabe H, Saito K, Kokubun K, Sasaki H, Yoshinari M. Change in surface properties of zirconia and initial attachment of osteoblastlike cells with hydrophilic treatment. Dent Mater J. 2012;31:806-14.

[118] Svanborg LM, Andersson M, Wennerberg A. Surface characterization of commercial oral implants on the nanometer level. J Biomed Mater Res B Appl Biomater. 2010;92:462-9.

[119] Jimbo R, Coelho PG, Bryington M, Baldassarri M, Tovar N, Currie F, Hayashi M, Janal MN, Andersson M, Ono D, Vandeweghe S, Wennerberg A. Nano Hydroxyapatite-coated Implants Improve Bone Nanomechanical Properties. J Dent Res 2012.

[120] Meirelles L, Melin L, Peltola T, Kjellin P, Kangasniemi I, Currie F, Andersson M, Albrektsson T, Wennerberg A. Effect of hydroxyapatite and titania nanostructures on early in vivo bone response. Clin Implant Dent Relat Res. Canada 2008. p. 245-54.

[121] Wennerberg A, Svanborg LM, Berner S, Andersson M. Spontaneously formed nanostructures on titanium surfaces. Clin Oral Implants Res. 2012.

[122] Kimura I, Kanatani M, Watanabe K. Adhesion of hollow calcium-deficient hydroxyapatite microspheres onto titanium. Dent Mater J. 2009;28:700-7.

[123] Kim MH, Lee SY, Kim MJ, Kim SK, Heo SJ, Koak JY. Effect of biomimetic deposition on anodized titanium surfaces. J Dent Res. 2011;90:711-6.

[124] Kikuchi S, Takebe J. Characterization of the surface deposition on anodized-hydrothermally treated commercially pure titanium after immersion in simulated body fluid. J Prosthodont Res. 2010;54:70-7.

[125] Martin JY, Schwartz Z, Hummert TW, Schraub DM, Simpson J, Lankford J, Dean DD, Cochran DL, Boyan BD. Effect of titanium surface roughness on proliferation, differentiation, and protein synthesis of human osteoblast-like cells (MG63). Journal of Biomedical Materials Research. 1995;29:389-401.

[126] Bratu EA, Tandlich M, Shapira L. A rough surface implant neck with microthreads reduces the amount of marginal bone loss: a prospective clinical study. Clinical oral implants research. 2009;20, 827-832

[127] Cochran DL, Buser D, ten Bruggenkate CM, Weingart D, Taylor TM, Bernard JP, Peters F, Simpson JP. The use of reduced healing times on ITI implants with a sandblasted and acid-etched (SLA) surface: early results from clinical trials on ITI SLA implants. Clin Oral Implants Res. 2002;13:144-53.

[128] Hu Y, Barbour M, Allen G. Time and pH dependence of adsorption of chlorhexidine on anatase and rutile titanium dioxide. In: VanderSloten J, Verdonck P, Nyssen M, Haueisen J, editors. 4th European Conference of the International Federation for Medical and Biological Engineering: Springer; 2009. p. 2265-8.
[129] Guo X, Xu D, Ding Z, Su W. Preparation and Raman spectrum of Rutile single crystals using floating zone method. Chin Phys Lett. 2006;23.
[130] Yoshitake H, Abe D. Raman spectroscopic study of the framework structure of amorphous mesoporous titania. Microporous and Mesoporous Materials. 2009;119:267-75.
[131] Tompsett GA, Bowmaker GA, Cooney RP, Metson JB, Rodgers KA, Seakins JM. The Raman spectrum of brookite, TiO_2 (Pbca, Z = 8). Journal of Raman Spectroscopy. 1995;26:57-62.
[132] Hardcastle FD, Ishihara H, Sharma R, Biris AS. Photoelectroactivity and Raman spectroscopy of anodized titania (TiO_2) photoactive water-splitting catalysts as a function of oxygen-annealing temperature. Journal of Materials Chemistry. 2011;21:6337-45.
[133] Seah MP, Dench WA. Quantitative electron spectroscopy of surfaces: A standard data base for electron inelastic mean free paths in solids Surface and Interface Analysis. 1979;1:2-11.
[134] Zhao G, Schwartz Z, Wieland M, Rupp F, Geis-Gerstorfer J, Cochran DL, Geis-Gerstorfer J, Cochran DL, Boyan BD. High surface energy enhances cell response to titanium substrate microstructure. J Biomed Mater Res A. 2005;74:49-58.
[135] Szmukler-Moncler S, Perrin D, Ahossi V, Magnin G, Bernard JP. Biological properties of acid etched titanium implants: effect of sandblasting on bone anchorage. J Biomed Mater Res B Appl Biomater. 2004;68:149-59.
[136] Jarmar T, Palmquist A, Branemark R, Hermansson L, Engqvist H, Thomsen P. Technique for preparation and characterization in cross-section of oral titanium implant surfaces using focused ion beam and transmission electron microscopy. J Biomed Mater Res A. 2008;87:1003-9.
[137] Zinelis S, Silikas N, Thomas A, Syres K, Eliades G. Surface characterization of SLActive dental implants. Eur J Esthet Dent. Germany 2012. p. 72-92.
[138] Buser D, Nydegger T, Oxland T, Cochran DL, Schenk RK, Hirt HP, Snétivy D, Nolte LP. Interface shear strength of titanium implants with a sandblasted and acid-etched surface: a biomechanical study in the maxilla of miniature pigs. J Biomed Mater Res. United States: 1999 John Wiley & Sons, Inc.; 1999. p. 75-83.

[139] Le Guehennec L, Lopez-Heredia MA, Enkel B, Weiss P, Amouriq Y, Layrolle P. Osteoblastic cell behaviour on different titanium implant surfaces. Acta Biomater. England2008. p. 535-43.

[140] Wennerberg A, Ohlsson R, Rosen BG, Andersson B. Characterizing three-dimensional topography of engineering and biomaterial surfaces by confocal laser scanning and stylus techniques. Med Eng Phys. England1996. p. 548-56.

[141] Cooper LF. A role for surface topography in creating and maintaining bone at titanium endosseous implants. J Prosthet Dent. United States2000. p. 522-34.

[142] Whitehead SA, Shearer AC, Watts DC, Wilson NH. Comparison of two stylus methods for measuring surface texture. Dent Mater. England1999. p. 79-86.

[143] Arvidsson A, Liedberg B, Moller K, Lyven B, Sellen A, Wennerberg A. Chemical and topographical analyses of dentine surfaces after Carisolv treatment. J Dent. England2002. p. 67-75.

[144] Mongra A, Kaur A. Surface characteristics of biomaterials in dental implants. J Acad Indus Res. 2012;1:186-95.

[145] Wild Md. Hydrophilic properties of SLActive dental implants. STARGET2005.

[146] Schwarz F, Herten M, Wieland M, Dard M, Becker J. [Chemically modified, ultra-hydrophilic titanium implant surfaces]. Mund Kiefer Gesichtschir. 2007;11:11-7.

[147] Schwarz F, Herten M, Sager M, Wieland M, Dard M, Becker J. Histological and immunohistochemical analysis of initial and early subepithelial connective tissue attachment at chemically modified and conventional SLA titanium implants. A pilot study in dogs. Clin Oral Investig. 2007;11:245-55.

[148] Feng B, Chen JY, Qi SK, He L, Zhao JZ, Zhang XD. Characterization of surface oxide films on titanium and bioactivity. J Mater Sci Mater Med. United States2002. p. 457-64.

[149] Sawase T, Jimbo R, Baba K, Shibata Y, Ikeda T, Atsuta M. Photo-induced hydrophilicity enhances initial cell behavior and early bone apposition. Clin Oral Implants Res. Denmark2008. p. 491-6.

[150] Sul YT, Johansson CB, Petronis S, Krozer A, Jeong Y, Wennerberg A, Albrektsson T. Characteristics of the surface oxides on turned and electrochemically oxidized pure titanium implants up to dielectric breakdown: the oxide thickness, micropore configurations, surface roughness, crystal structure and chemical composition. Biomaterials. 2002;23:491-501.

[151] Blanco A, Bussoletti E, Colangeli L, Fonti S, Orofino V. Raman spectra of submicron amorphous carbon grains and mixtures of polycyclic aromatic hydrocarbons. Infrared Physics. 1988;28:383-8.

[152] de Aza PN, Santos C, Pazo A, de Aza S, Cuscó R, Artús L. Vibrational Properties of Calcium Phosphate Compounds. 1. Raman Spectrum of β-Tricalcium Phosphate. Chemistry of Materials. 1997;9:912-5.

[153] Xu J, Butler IS, Gilson DFR. FT-Raman and high-pressure infrared spectroscopic studies of dicalcium phosphate dihydrate ($CaHPO_4 \cdot 2H_2O$) and anhydrous dicalcium phosphate (CaHPO4). Spectrochimica Acta Part A: Molecular and Biomolecular Spectroscopy. 1999;55:2801-9.

[154] NIST XPS Database. http://srdata.nist.gov/xps/EnergyTypeValSrch.aspx.

[155] Lausmaa J, Kasemo B, Mattsson H. Surface spectroscopic characterization of titanium implant materials. Applied Surface Science. 1990;44:133-46.

[156] Dilks A. In: Brundle CR, Baker AD, editors. Electron Spectroscopy: Theory, Techniques and Apllications: Academic Press London; 1981.

[157] Armstrong NR, Quinn RK. Auger and X-ray photoelectron spectroscopic and electrochemical characterization of titanium thin film electrodes. Surface Science. 1977;67:451-68.

[158] Aita H, Hori N, Takeuchi M, Suzuki T, Yamada M, Anpo M, Ogawa T. The effect of ultraviolet functionalization of titanium on integration with bone. Biomaterials. England 2009. p. 1015-25.

[159] Chusuei CC, Goodman DW, Van Stipdonk MJ, Justes DR, Schweikert EA. Calcium Phosphate Phase Identification Using XPS and Time-of-Flight Cluster SIMS. Anal Chem. 1999;71:149-53.

[160] Qu Z, Rausch-Fan X, Wieland M, Matejka M, Schedle A. The initial attachment and subsequent behavior regulation of osteoblasts by dental implant surface modification. J Biomed Mater Res A. 2007;82:658-68.

[161] Esposito M, Grusovin MG, Coulthard P, Thomsen P, Worthington HV. A 5-year follow-up comparative analysis of the efficacy of various osseointegrated dental implant systems: a systematic review of randomized controlled clinical trials. Int J Oral Maxillofac Implants. 2005;20:557-68.

[162] Mao JJ. Stem cells and the future of dental care. N Y State Dent J. 2008;74:20-4.

[163] Angelova Volponi A, Kawasaki M, Sharpe PT. Adult Human Gingival Epithelial Cells as a Source for Whole-tooth Bioengineering. J Dent Res. United States 2013. p. 329-34.

[164] El-Bialy T. Editorial: a review of tooth tissue engineering studies. Open Dent J. Netherlands 2012. p. 212-3.

[165] Moioli EK, Clark PA, Xin X, Lal S, Mao JJ. Matrices and scaffolds for drug delivery in dental, oral and craniofacial tissue engineering. Adv Drug Deliv Rev. Netherlands2007. p. 308-24.

[166] Na S, Zhang H, Huang F, Wang W, Ding Y, Li D, Jin Y. Regeneration of dental pulp/dentine complex with a three-dimensional and scaffold-free stem-cell sheet-derived pellet. J Tissue Eng Regen Med. 2013.

[167] Nguyen TT, Mui B, Mehrabzadeh M, Chea Y, Chaudhry Z, Chaudhry K, Tran SD. Regeneration of tissues of the oral complex: Current clinical trends and advances. J Can Dent Assoc. 2013;79:d1.

[168] Sujesh M, Rangarajan V, Ravi Kumar C, Sunil Kumar G. Stem cell mediated tooth regeneration: new vistas in dentistry. J Indian Prosthodont Soc. India2012. p. 1-7.

[169] Yildirim S, Fu SY, Kim K, Zhou H, Lee CH, Li A, Kim SG,Wang S, Mao JJ. Tooth regeneration: a revolution in stomatology and evolution in regenerative medicine. Int J Oral Sci. 2011;3:107-16.